LBL-13200

Lawrence Berkeley Laboratory

UNIVERSITY OF CALIFORNIA

Materials & Molecular Research Division

OCT 26 1981

LIBRARY AND DOCUMENTS SECTION

RADIATION ENHANCEMENT OF STRESS CORROSION CRACKING OF ZIRCALOY

Shih-Hsiung Shann
(Ph.D. thesis)

September 1981

TWO-WEEK LOAN COPY

This is a Library Circulating Copy which may be borrowed for two weeks. For a personal retention copy, call Tech. Info. Division, Ext. 6782

LBL-13200 c.2

Prepared for the U.S. Department of Energy under Contract W-7405-ENG-48

DISCLAIMER

This document was prepared as an account of work sponsored by the United States Government. While this document is believed to contain correct information, neither the United States Government nor any agency thereof, nor the Regents of the University of California, nor any of their employees, makes any warranty, express or implied, or assumes any legal responsibility for the accuracy, completeness, or usefulness of any information, apparatus, product, or process disclosed, or represents that its use would not infringe privately owned rights. Reference herein to any specific commercial product, process, or service by its trade name, trademark, manufacturer, or otherwise, does not necessarily constitute or imply its endorsement, recommendation, or favoring by the United States Government or any agency thereof, or the Regents of the University of California. The views and opinions of authors expressed herein do not necessarily state or reflect those of the United States Government or any agency thereof or the Regents of the University of California.

LBL-13200

RADIATION ENHANCEMENT OF STRESS CORROSION CRACKING OF ZIRCALOY

SHIH-HSIUNG SHANN

Ph.D. Thesis

Department of Nuclear Engineering of the University of California,
and the Materials and Molecular Research Division of the
Lawrence Berkeley Laboratory, University of California,
Berkeley, CA 94720

September 1981

This work was supported by the Director, Office of Energy Research, Office of Basic Energy Science, Materials Sciences Division of the U. S. Department of Energy under Contract No. W-7405-ENG-48.

TABLE OF CONTENTS

1. INTRODUCTION. 1

1.1 OBJECTIVE. 1

1.2 REVIEW OF PREVIOUS WORK. 2

1.3 EXPERIMENTAL APPROACH. 4

2. EXPERIMENTAL. 6

2.1 IODINE 6

2.2 IODINE EQUIVALENT PRESSURE CALCULATION 7

2.3 METAL IODIDES AND CADMIUM. 7

2.4 METAL IODIDE AND CADMIUM EQUIVALENT PRESSURES. 8

2.5 CESIUM IODIDE IRRADIATION STUDY. 9

3. IODINE STRESS CORROSION CRACKING OF ZIRCALOY. 12

3.1 INTRODUCTION 12

3.2 EXPERIMENTAL 12

3.3 MATERIALS. 12

3.4 RESULTS. 13

3.4.1 FAILURE MODES 13

3.4.2 TIME TO RUPTURE 13

3.5 DISCUSSION 14

3.5.1 IODINE CONCENTRATION. 14

3.5.2 BIAXIALITY. 15

3.5.3 STRESS AND IODINE PRESSURE THRESHOLD. 16

3.5.4 HIGH STRESS FAILURE 16

3.5.5 DATA CORRELATION. 16

4. ALUMINUM IODIDE STRESS CORROSION CRACKING OF ZIRCALOY 40
4.1 INTRODUCTION 40
4.2 EXPERIMENTAL 40
4.3 MATERIALS. 40
4.4 RESULTS. 40
4.5 DISCUSSION 41
4.5.1 FRACTOGRAPHY. 41
4.5.2 EDAX EXAMINATION RESULTS. 41
4.5.3 DATA CORRELATION. 41
4.5.4 IODIDE AFFECTED SURFACE STUDY OF UNFAILED SPECIMENS 41
5. IRON IODIDE STRESS CORROSION CRACKING OF ZIRCALOY 55
5.1 INTRODUCTION 55
5.2 EXPERIMENTAL 55
5.3 MATERIALS. 55
5.4 RESULTS. 55
5.4.1 FAILURE MODE. 55
5.4.2 TIME TO FAILURE 56
5.5 DISCUSSION 56
5.5.1 FRACTOGRAPHY. 56
5.5.2 IRON IODIDE EQUIVALENT PRESSURE 56
5.5.3 TEMPERATURE DEPENDENCE. 57
5.5.4 DATA CORRELATION. 57
5.5.5 CRACK INITIATION. 57

6. CRACK INITIATION STUDY FOR IRON IODIDE SCC. 68
6.1 INTRODUCTION 68
6.2 EXPERIMENTAL 68
6.3 RESULTS AND DISCUSSION 69
6.3.1 CRACK PROPAGATION DOMINATES THE SPECIMEN LIFETIME. 69
6.3.2 CRACK INITIATION SITES. 69
7. CADMIUM VAPOR EMBRITTLEMENT OF ZIRCALOY 80
7.1 INTRODUCTION 80
7.2 EXPERIMENTAL 80
7.3 MATERIALS. 80
7.4 RESULTS. 80
7.4.1 FAILURE MODE. 80
7.4.2 TIME TO FAILURE 81
7.5 DISCUSSION 81
7.5.1 SCATTER OF DATA 81
7.5.2 FRACTOGRAPHY. 82
7.5.3 DATA CORRELATION. 82
7.5.4 CADMIUM EQUIVALENT PRESSURE 83
7.5.5 TEMPERATURE WINDOW. 83
8. EFFECT OF CESIUM IODIDE ON THE FAILURE TIME OF ZIRCALOY . . . 95
8.1 INTRODUCTION 95
8.2 EXPERIMENTAL 95
8.2.1 NONIRRADIATED CASE. 95
8.2.2 IRRADIATED CASE 95

8.3 MATERIALS. 96

8.4 RESULTS. 96

8.4.1 CESIUM IODIDE AFFECTED SPECIMENS WITHOUT IRRADIATION. 96

8.4.2 SPECIMEN WITH IRRADIATION ONLY. 96

8.4.3 IRRADIATED AND CESIUM IODIDE AFFECTED SPECIMENS 97

8.5 DISCUSSION 97

8.5.1 UNIRRADIATED CESIUM IODIDE AFFECTED SPECIMENS 97

8.5.2 IRRADIATED AND CESIUM IODIDE AFFECTED SPECIMENS 98

8.5.3 FILM FORMATION IN IRRADIATED AND CESIUM IODIDE AFFECTED TESTS 98

8.5.4 EFFECT OF FILM THICKNESS. 102

8.5.5 ENERGY DEPOSITION RATE FROM THE PROTON BEAM COMPARED WITH INPILE ENVIRONMENT 102

9. DISCUSSION. 118

9.1 CRACK PROPAGATION CONTROLS THE FAILURE TIME. 118

9.2 PROPOSED ENVIRONMENT AFFECTED CRACK PROPAGATION MODEL. . 118

9.2.1 IODINE. 120

9.2.2 ALUMINUM IODIDE 120

9.2.3 IRON IODIDE 121

9.3 IN PILE SITUATION. 122

9.3.1 CHEMISTRY OF IODIDE 122

9.3.2 CHEMISTRY OF CADMIUM. 124

10. CONCLUSIONS. 126

10.1 UNIRRADIATED STRESS CORROSION CRACKING TEST RESULTS. . 126

10.2 DATA CORRELATION OF FAILURE TIMES. 127

10.3 RADIATION ENHANCED CESIUM IODIDE STRESS CORROSION CRACKING TESTS 129

10.4 IN PILE SITUATION 129

APPENDIX A IODINE FLOW RATE CALIBRATION. 133

A.1 INTRODUCTION 133

A.2 APPARATUS. 133

A.3 CALIBRATION PROCEDURE. 133

A.4 RESULTS AND DISCUSSION 135

A.5 CONCLUSION 138

APPENDIX B CALCULATION OF VAPOR PRESSURES OVER ALUMINUM IODIDE. 145

REFERENCES 148

LIST OF TABLES

Table 3-1 Composition of Sandvik Zr-2 (9AX32)

Table 5-1 Composition of Sandvik Zr-4 (JV11)

Table 8-1 Radiation enhanced CsI test results

Table 8-2 Adsorption, desorption, and sputtering calculation (specimen temperature = 350°C, test time = 22 hours)

Table 10-1 Chemical parameters for zircaloy SCC

LIST OF FIGURES

Figure 2-1 Iodine stress corrosion cracking apparatus

Figure 2-2 Irradiated cesium iodide stress corrosion cracking apparatus

Figure 3-1 Photo of the stress corrosion cracking apparatus

Figure 3-2 Stress relieved Zr-2 (Sandvik lot No. 9AX32) failed after 13.2 hrs under 316 MPa and 0.014 torr iodine at 300°C

Figure 3-3 Stress relieved Zr-2 (Sandvik lot No. 9AX32) failed after 5.0 hrs under 369 MPa and 0.014 torr iodine at 300°C

Figure 3-4 Stress relieved Zr-2 (Sandvik lot No. 9AX32) failed after 9.0 hrs under 369 MPa and 0.01 torr iodine at 300°C

Figure 3-5 Stress relieved Zr-2 (Sandvik lot No. 9AX32) failed after 3.2 hrs under 324 MPa and 0.02 torr iodine at 325°C

Figure 3-6 Stress relieved Zr-2 (Sandvik lot No. 9AX32) failed after 17.0 hrs under 311 MPa and 0.014 torr iodine at 270°C

Figure 3-7 Control specimens of Sandvik lot No. 9AX32 ruptured at 300°C without iodine at stresses of 383, 370, and 343 MPa

Figure 3-8 SEM fractography of pin-hole type failure (preflawed stress relieved Zr-2 from SRI); failed after 5.9 hrs under 361 MPa 0.025 torr iodine, and 320°C

Figure 3-9 SEM fractography of ductile failure (unflawed, stress relieved Zr-2 from SRI); failed after 51.8 hrs at 364 MPa and 320°C without iodine

Figure 3-10 Besides the main penetrating crack, there are many small cracks in iodine affected area. (Preflawed stress relieved Zr-2 from SRI failed after 59.3 hrs; 361 MPa, 0.025 torr iodine, 320°C).

Figure 3-11 Same specimen as Figure 3-8 showing many small cracks branching out from the main crack.

Figure 3-12 Transition from brittle mode to ductile dimple mode

Figure 3-13 Grains failed by cleavage (preflawed stress relieved Zr-2 from SRI failed after 5.9 hrs; 361 MPa, 0.025 torr iodine, 320°C)

Figure 3-14 Time to failure vs. iodine pressure relation for unflawed SRI specimens

Figure 3-15 Time to failure vs. iodine relationship pressure for preflawed SRI specimens

Figure 3-16 Time to failure versus stress relations for control specimens without corrosive agent and specimens under 0.014 torr iodine at 300°C (Sandvik specimens)

Figure 3-17 Time to failure versus temperature relationship for Sandvik specimens at 314 MPa and 0.014 torr iodine pressure

Figure 3-18 Time to failure versus iodine pressure for Sandvik specimens at 369 MPa and 300°C (the rupture time = 44.3 hrs for control specimen)

Figure 3-19 SEM fractography of a burst type failure 379 MPa, 300°C, 0.014 torr iodine pressure after 8.2 hours. Cleavage (brittle) characteristics are similar to those observed in pinhole-type failure

Figure 3-20 Time to failure versus iodine equivalent pressure for three lots of zircaloy tubes

Figure 4-1 Effects of aluminum iodide exposure on zircaloy SCC: the time to failure decreases as the 2/3 power of the AlI_3 pressure

Figure 4-2 SEM fractography of pinhole-type failure (Zr-2 (9AX32) failed after 36.7 hrs; 365 MPa, 300°C, 1.4 x 10^{-3} torr AlI_3) cleavage, transgranular failure

Figure 4-3 SEM fractography of burst type failure (Zr-2 (9AX32) failed after 9.4 hrs; 365 MPa, 300°C, 2.0 x 10^{-3} torr AlI_3)

Figure 4-4 Aluminum EDAX signal moving from outside surface of the tube into the crack (for different positions and different specimens) C_{Al} is the count of X-ray for aluminum, C_I is the count of X-ray for iodine, and C_{tot} is the total count of X-ray for all elements

Figure 4-5 Iodine EDAX signal moving from outside surface of the tube into the crack (for different positions and different specimens)

Figure 4-6 Unfailed specimen with visible crack initiation (1.1 x 10^{-3} torr AlI_3 equivalent pressure, 365 MPa, and 300°C for 43 hrs

Figure 4-7 SEM of cracked zone of specimen in Figure 4-6

Figure 4-8 Detailed view of the white deposit in Figure 4-7

Figure 4-9 EDAX signals from the white deposit in Figure 4-8

Figure 4-10 SEM picture of unfailed specimen under 365 MPa, 300°C, and 3.3×10^{-3} torr AlI_3 equivalent pressure for 43 hours

Figure 4-11 SEM picture of unfailed specimen under 365 MPa, 8.0×10^{-5} torr AlI_3 equivalent pressure, and 300°C for 43 hrs

Figure 5-1 Burst type failure for specimen under 379 MPa, 350°C, and 8.6×10^{-3} torr iron iodide equivalent pressure after 9.4 hrs

Figure 5-2 Pinhole type failure for specimen under 376 MPa, 360°C, and 8.6×10^{-3} torr iodide equivalent pressure after 3.3 hrs

Figure 5-3 Time-to-failure versus stress for control specimens without corrosive agent and specimens under fixed iron iodide equivalent pressure (8.6×10^{-3} torr) and temperature (350°C)

Figure 5-4 SEM fractography of pinhole-failed specimen in Figure 5-2

Figure 5-5 SEM fractography of burst-failed specimen in Figure 5-1

Figure 5-6 Time-to-failure versus iron iodide equivalent pressure relationship under fixed stress and temperature

Figure 5-7 Time-to-failure versus temperature relationship under fixed stress and iron iodide equivalent pressure

Figure 5-8 Brittle-to-ductile transition on the fracture surface (Figure 5-5 specimen)

Figure 5-9 Iodide-affected surface of specimen under 376 MPa, 350°C, and 8.6 x 10^{-3} torr iodine equivalent pressure; removal before failure

Figure 6-1 Auger electron spectrum of the specimen (under iron iodide for 20 percent of its lifetime) before argon sputtering (Surface shown in Figure 5-9b)

Figure 6-2 The sputtered region under SAM after 30 min

Figure 6-3 Auger Electron Spectrum for the specimen after removal of 0.5 μm)

Figure 6-4 Argon sputtered region under SEM

Figure 6-5 Region A (with high crack initiation probability)

Figure 6-6 Region B (with high crack initiation probability)

Figure 6-7 Region C (with high crack initiation probability)

Figure 6-8 Region D (with high crack initiation probability)

Figure 6-9 Region E (with high crack initiation probability)

Figure 6-10 Region F (with low crack initiation probability)

Figure 7-1 Burst type failure for specimen under 388 MPa, 350°C, and 8.3 x 10^{-3} torr cadmium equivalent pressure after 2.8 hrs

Figure 7-2 Time-to-failure versus stress relationship for control specimens without corrosive agent and specimens under fixed cadmium pressure (8.3 x 10^{-3} torr) and temperature (350°C)

Figure 7-3 Time-to-failure versus cadmium equivalent pressure relationship under fixed stress and temperature

Figure 7-4 Time-to-failure versus temperature relationship under fixed stress and cadmium equivalent pressure

Figure 7-5 SEM fractography of burst-failed specimen in Figure 7-1

Figure 7-6 SEM fractography of burst-failed specimen in Figure 7-1

Figure 7-7 Temperature window study for cadmium vapor embrittlement

Figure 7-8 Fractography of specimen failed under 395°C, 376 MPa, 8.3 x 10^{-3} torr Cd after 1.6 hours

Figure 7-9 Fractography of specimen tested under 2 mtorr and 360°C, showing ductile dimple fractography

Figure 8-1 Time to failure versus stress for control specimens and specimens subjected to CsI

Figure 8-2 Burst-type failure of specimen under 393 MPa, 1.5 x 10^{-3} torr CsI, and 350°C after 11 hours

Figure 8-3 Fractography of specimen in Figure 8-2

Figure 8-4 CsI-affected region on O.D. surface of specimen in Figure 8-2

Figure 8-5 Fractography of the specimen tested under radiation without CsI

Figure 8-6 Specimen tested under 4 x 10^{-4} torr CsI, 386 MPa, 350°C, and 0.35 MeV, 5 μA H_2^+ irradiation

Figure 8-7 Specimen tested under 5 x 10^{-5} torr CsI, 386 MPa, 350°C, and 0.35 MeV, 5μA H_2^+ irradiation

Figure 8-8 Optical microscopy of the film on specimen under 10^{-3} torr CsI, and radiation for 22 hours

Figure 8-9 Cesium iodide and radiation-affected region on specimen subject to 4 x 10^{-4} torr CsI (46 atom % I and 54 atom % Cs) no cracks visible.

Figure 8-10 Cesium iodide-affected zone outisde the irradiation region on μ in Figure 8-6 (44 atom % I and 56 atom % Cs)

Figure 8-11 The transition zone between Figure 8-9 and 8-10

Figure 8-12 White deposits on O.D. surface of the specimen in Figure 8-10 (on the CsI-H_2^+) spot)

Figure 10-1 Comparison of fractography

Figure A-1 Doser flow rate calibration apparatus

Figure A-2 Pressure drop versus time in the reservoir compared with Schock's model (Argon)

Figure A-3 Pressure drop versus time in the reservoir with and without target assembly (Argon)

Figure A-4 Peaking factor versus flow rate and doser-to-target distance (Argon)

Figure A-5 Peaking factor versus flow rate and doser-to-target distance (Argon)

Figure A-6 Peaking factor versus normalized doser-target distance (Argon)

Figure B-1 Relative pressures of vapor species over aluminum iodide crystals in a stainless steel Knudsen cell

ACKNOWLEDGEMENT

I would like to express my appreciation to the following people:

Professor Donald R. Olander, who suggested this topic, whose excellent guidance and advice contributed heavily to this thesis.

Professor Stanley G. Prussin, whose helpful discussions are deeply appreciated.

I would like to thank John Souza and Dan Winterbauer for fabricating the needed parts, and Jack Harrel for electronic support.

I would like to thank my parents and my wife for their everlasting encouragement.

This work was supported by the Director, Office of Energy Research, Office of Basic Energy Science, Materials Sciences Division of the U.S. Department of Energy under Contract No. W-7405-ENG-48.

RADIATION ENHANCEMENT OF STRESS CORROSION CRACKING OF ZIRCALOY

SHIH-HSIUNG SHANN

The Department of Nuclear Engineering of the University of California, and the Materials and Molecular Research Division of the Lawrence Berkeley Laboratory, Berkeley, California 94720

ABSTRACT

In order to examine the cause of the reactor fuel pin pellet-cladding interaction phenomenon (PCI), stress corrosion cracking (SCC) experiments of zircaloy under iodine, iron iodide, aluminum iodide, cesium iodide, and cadmium were undertaken. Radiation enhancement tests with CsI were also performed to check whether iodine released by irradiation can induce zircaloy SCC. Rupture lifetimes were measured as a function of stress, temperature, and the equivalent pressure of the corrosive agents.

Iodine, iron iodide, and aluminum iodide can reduce the failure times in comparison to those of control specimens at the same stress and temperature without corrosive agent. Fractography is of cleavage type, and is completely different from the ductile dimple type failure for control specimens. There exists a critical stress of 379 MPa for iodine and iron iodide above which "burst type" failure occurs. "Pinhole type" failure predominates for lower stresses. Both types showed brittle fracture surfaces.

The presence of cesium iodide did not have any influence on failure time of zircaloy. The failure is burst-type, and the fractography is ductile. Radiation enhancement tests with cesium iodide did not cause reduction in failure time either.

Compared to control specimens, failure times were decreased for the tests under cadmium. All specimens failed under cadmium vapor by a burst mode, and fractography showed cleavage brittle characteristics.

Chemical parameters such as reaction order, activation energy, and minimum pressure required for SCC were determined.

A crack propagation model originally designed for brittle solids was applied for SCC. This model can fit the present experimental data well. Variable stresses and surface roughness test results can be correlated quantitatively by the model.

RADIATION ENHANCEMENT OF STRESS CORROSION CRACKING OF ZIRCALOY

SHIH-HSIUNG SHANN

The Department of Nuclear Engineering of the University of California, and the Materials and Molecular Research Division of the Lawrence Berkeley Laboratory, Berkeley, California 94720

1. INTRODUCTION

1.1 Objective

The outstanding high temperature water corrosion resistance and highly desirable nuclear characteristics of zircaloy have made it an excellent cladding material for light water reactors. However, low ductility failures of the cladding still occasionally occur, pointing to the need for understanding of the fracture mechanism and prevention methods.

The fractography of cracked cladding resembles that of stress corrosion cracking in the laboratory.[1] Previous works[1-14] have studied mainly unirradiated specimens in iodine. Wood et al.[6,11] tested irradiation samples, but no tests concerning simultaneous irradiation and stress corrosion have been reported.

Iodine is present as a fission product in irradiated fuel rods. However, according to thermodynamics, all of this iodine should be combined with the more abundant fission product cesium to produce the stable solid CsI.[15] This substance is not an active stress corrosion cracking agent to zircaloy, as demonstrated by out-of-pile tests.[8,13] The main purpose of this project is to determine if sufficient free iodine is released from CsI by irradiation in order to activate the stress corrosion cracking process.

1.2 Review of Previous Work

At the beginning of the present project (April 1977), there were several works concerning metallurgical and chemical aspects of iodine SCC in the literature.[1-15] The effects of stress,[1-15] temperature,[6,7] strain rate,[1] strain hardening,[1] residual stress,[6] annealing,[6] and basal pole orientation[6] of zircaloy have been tested. But most tests used qualitative models to explain their results. The only quantitative empirical model was proposed by the Bettis Atomic Laboratory of Westinghouse.[5,14] Kreyns[5] curve fit the double cantilever beam experimental results of Wood[1] and found:

$$da/dt = CK^4 \tag{1-1}$$

where K is the stress intensity factor, a is the crack length, and C is a constant. They assumed that the crack propagation rate in zircaloy tube specimens is of the following form:[5,14]

$$da/dt = C_o \exp(-Q/RT)\,[I_2]^n\,K^4 \tag{1-2}$$

Eq (1-2) can be integrated from the initial crack length a_o (pre-existing through manufacture or machining) to the final crack length a_c, at which the net section stress of tube wall equals the ultimate tensile stress of zircaloy, to calculate the lifetime of tube specimen. Here they assumed the crack propagates from the initial length to the final length at which point ductile failure takes over and the tube fails immediately. They used their experimental results with least square curve fitting to determine the constants C_o, Q, and n.[5,14]

In March 1980, SRI International published their detailed experimental study of iodine SCC.[16] They used a tube burst technique with sealed iodine solid inside zircaloy to measure the lifetime as a function of stress. The effects of zircaloy tube manufacturing technique, texture, surface condition, axial stress to hoop stress ratio, and damage accumulation were determined.

In Arpil 1981, Miller et al. proposed a phenomenological model, SCCIG (Stress Corrosion Cracking Initiation and Growth), for iodine SCC.[17] They assumed diffusion-controlled iodine penetration into the crack tip according to the equation;

$$dI/dt \propto (I_2 F(\varepsilon) - I)$$

where I_2 is the external iodine concentration and I is the iodine concentration at the crack tip. $f(\varepsilon)$ is a function of crack tip strain ε. With a "Bundle of Sticks" geometry in the zircaloy wall, they performed stress and strain calculations by force and momentum balance. A statistical initial surface flaw distribution was proposed and the model was fitted to SRI's experimental results.[16] For a faster calculation of inpile fuel condition, an explicity CFM II (Cladding Failure Model II) model was derived.[17] The SCCIG calculation result is the data base of CFM II. CFM II is used within the Spear-β fuel performance code.

Peehs et al. performed tests to determine the threshold iodine concentration needed for SCC.[18] A treelike glass apparatus was used to prepare precise aliquots of iodine for the tube-burst specimens. The glass tree was first pumped down and filled with iodine gas of

known pressure. After valving off capsules (branches), the iodine vapor pressure and capsule volume determined the amount of iodine contained in each capsule. The iodine capsules were sealed in zircaloy specimens with both ends capped. As the start of an experiment, the capsule was broken, and iodine was released to attack the zirconium. They found the minimum iodine inventory needed for SCC to be 1 mg/cm^2, which corresponds to 10^{-12} torr if Zr/I equilibrium is achieved.

1.3 Experimental Approach

From a chemical point of view, the molecular beam method utilized in the present study has the possiblity for reaction order and activation energy measurements. No previos zircaloy SCC work used this method. The reported minimum pressure of iodine necessary is fairly high (~13 torr).[3] This value is beyond the range of our test apparatus. In order to examine the applicability of the present experimental method, establishment of a complete iodine-zircaloy stress corrosion data base is necessary for a reference system and for better understanding of fracture mechanism Also, metal iodides such as FeI_2 and AlI_3 could attain low partial pressures in a fuel rod, so the determination of minimum pressures required for metal iodide SCC is important. Study of iron iodide and aluminum iodide SCC can also help in understanding the surface chemistry of the iodine-zirconium system.

A Van De Graaff accelerator is used as the radiation source in the cesium iodide irradiation study. The reaction chamber that is connected to the accelerator beam tube is under vacuum. By molecular flow from a Knudsen cell, a molecular beam of cesium iodide impinges on the zircaloy surface at the same spot as the proton beam bombardment.

Cadmium is a fission product which thermodynamics suggests should exist inside a fuel pin in the metallic state.[19] Liquid cadmium is known to cause severe embrittlement of zircaloy.[19] In an in-pile situation, however, the cladding is in contact with the low partial pressure vapor phase rather than with a condensed phase, so atomic beams of cadmium served as the active agent in this phase of the program.

2. EXPERIMENTAL

2.1 Iodine

The present experient utilizes a tube-burst (biaxial) test mode. Tube samples internally pressurized with argon are connected to a pressure transducer (Statham PA-891-3M) and a filling valve (Figure 2-1). The assembly is placed in an enclosure and heated resistively.

For temperature measurement and control, a thermocouple is pushed against the zircaloy tube by a stainless steel spring, the force of which is enough for the good contact between thermocouple and zircaloy, but is too small to cause indentation of the tube. Thin thermocouple wires (0.25 mm diameter) are used in order to keep the heat loss through the thermocouple wires as small as possible. An electronic control system (Omega Engineer, Inc. Model 49) compares the output voltage of the thermocouple with a preset standard and operates a relay in order to turn on or off the heating current. The temperature can be controlled within ±5°C of the set temperature.

The tube is pressurized by inert gas prior to closing the filling valve and inserting into the vacuum system. The hoop stress in the zircaloy tube is calculated from the thin-wall tube formula

$$\sigma = PR/w \qquad (2\text{-}1)$$

where

σ = applied hoop stress

P = internal gas pressure

R = tube radius

w = tube wall thickness

To prevent damage to the diffusion pump following a burst of the internally pressurized test specimen, a loose-fitting glass rod is inserted in the tube specimen to reduce the gas volume. When the specimen fails, less than 0.01 moles of gas flow into the vacuum system.

2.2 Iodine Equivalent Pressure Calculation

Molecular iodine is supplied to the surface through a 4.6 mm diameter tubing which is 2 to 5 mm from the specimen surface. With this delivery system, iodine impinges on a spot ~5 mm in diameter on the outside surface of zircaloy specimen. The iodine flow rate through the doser (1*) is calculated from Shock's model.[20] Conversion to equivalent pressure is accomplished by a procedure involving calibration with argon. The details of the calibration and the calculation are discussed in Appendix A.

2.3 Metal Iodides and Cadmium

The same apparatus is used for metal iodides and cadmium cases. The iodine doser is replaced by a Knudsen cell. The corrosive agents are placed in the Knudsen cell and heated to a fixed temperature. The vapor pressure of the corrosive substances at that temperature determines the flow rate through 1 mm diameter hole on the cell. The Knudsen cell was placed at 5-10 mm from the zircaloy specimen. It created an 8 mm diameter impingement spot on the tube.

2.4 Metal Iodide and Cadmium Equivalent Pressures

The metal iodide or cadmium flow rate 1* through the orifice of the Knudsen cell an be expressed as:

$$1^* = (1/4)nv\pi a^2 \qquad (2\text{-}2)$$

where:

n = molecular density of corrosive agent in the Knudsen cell

v = average velocity of the gas molecules in the Knudsen cell

a = radius of the orifice on the Knudsen cell

The gas density and molecular speed are determined at the Knudsen cell temperature T_K: and

$$n = P_K/kT_K \qquad (2\text{-}3)$$

$$v = \sqrt{8kT_K/\pi m} \qquad (2\text{-}4)$$

where

P_K = vapor pressure of corrosive agent in Knudsen cell at T_K

m = molecular weight of the corrosive agent

k = gas constant

Assuming a cosine distribution of the molecular beam from the orifice, the rate at which the corrosive agent strikes a unit area of the zircaloy surface at a distance d from the orifice is given by

$$I^* = 1^*/\pi d^2 \qquad (2\text{-}5)$$

The equivalent pressure P_{eq} of the corrosive agent based on the impingement rate can be calculated by

$$I^* = P_{eq} \Big/ \sqrt{2\pi mkT_K} \tag{2-6}$$

Combining Eqs. 2-2 through 2-5 yields

$$P_{eq} = P_K (a/d)^2 \tag{2.7}$$

As an example, we can consider the cadmium case, $P_K = 0.6$ torr at 400°C, a = 0.5 mm, and d = 7 mm, we get $P_{eq} = 4 \times 10^{-3}$ torr.

2.5 Cesium Iodide Irradiation Study

For the cesium iodide simultaneous irradiation study, a Van de Graaff accelerator which serves as a radiation source is connected to the reaction chamber used in metal iodide experiments. When the sample bursts, argon flows into the vacuum system. This sudden increase in pressure could damage the accelerator beam tube. A slammer valve[21] was built and inserted between reaction chamber and the accelerator (Fig. 2-2). The valve closes in ~0.2 msec after the pressure signal received by the ion gauge on the reaction chamber. The total time interval after tube burst, ion gauge response, and valve activation is short enough to close the slammer valve sufficiently quickly and prevents the argon shock wave from reaching the beam tube. The accelerator can be protected.

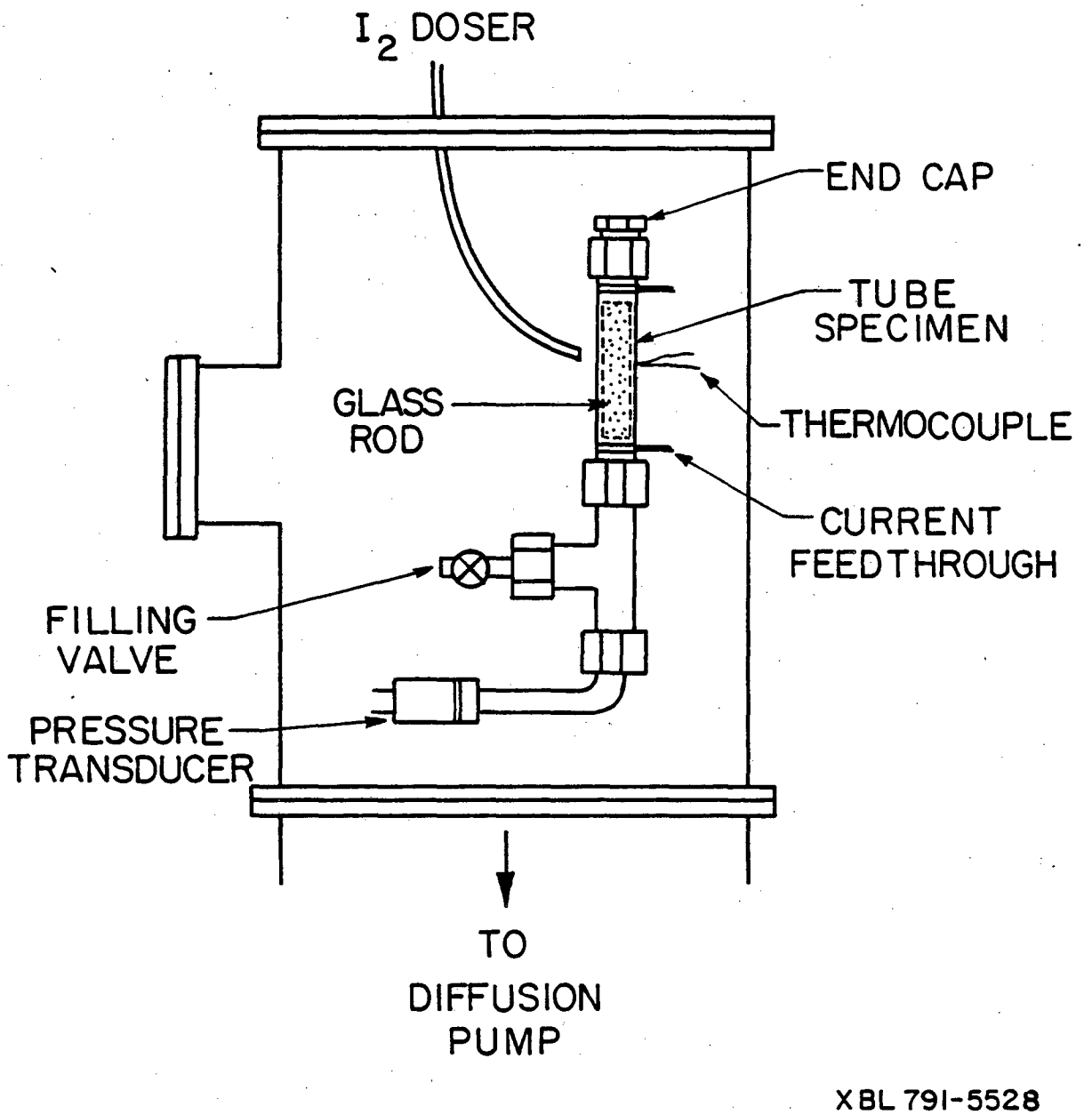

Figure 2-1. Iodine stress corrosion cracking apparatus.

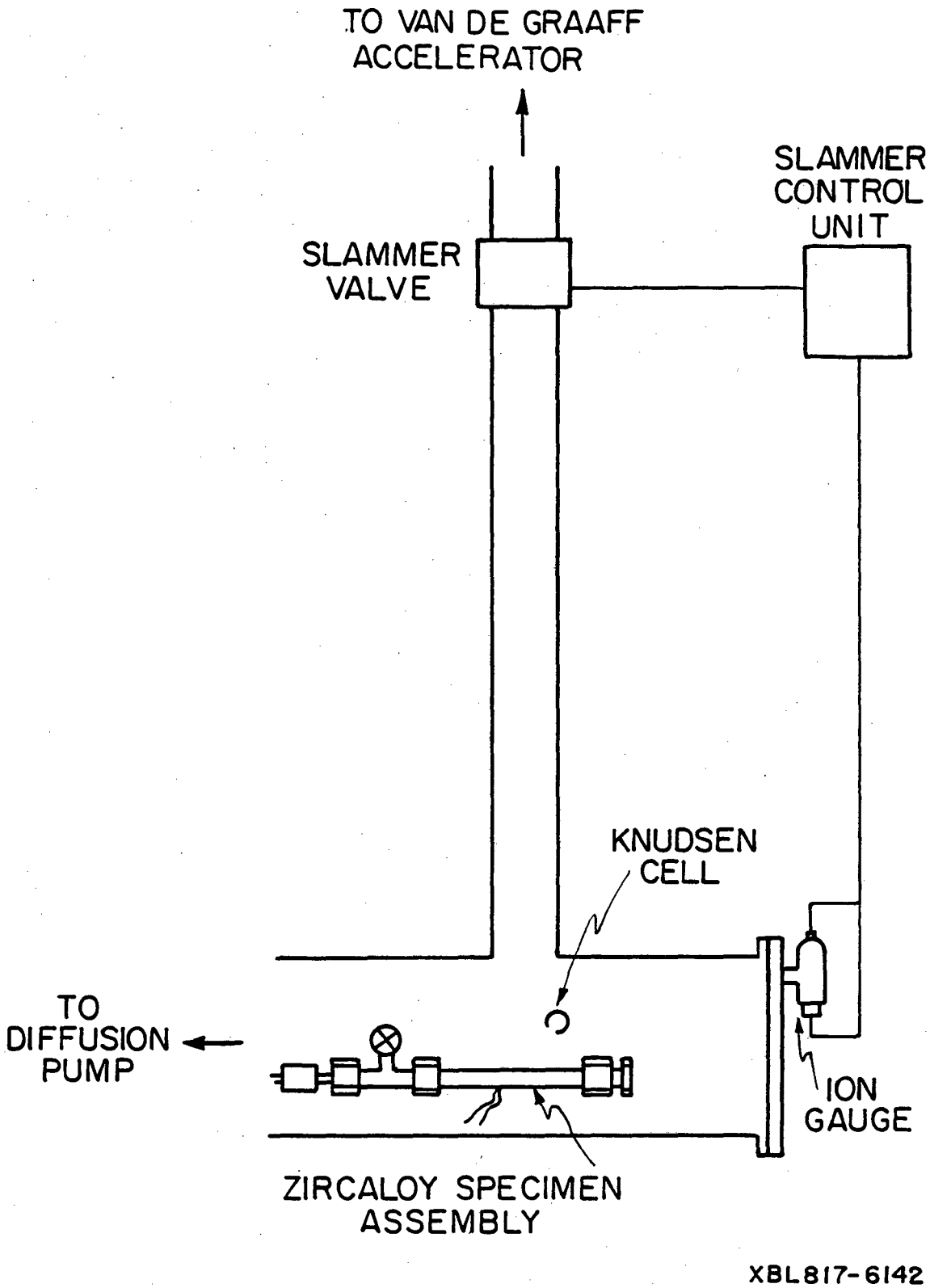

Figure 2-2. Irradiated cesium iodide stress corrosion cracking apparatus.

3. IODINE STRESS CORROSION CRACKING OF ZIRCALOY

3.1 Introduction

In order to achieve a long range pellet-cladding interaction study objective, and to examine the applicability of the molecular beam technique, the iodine stress corrosion cracking tests were undertaken. The results can be compared with previous work in the literature using different experimental methods. The iodine SCC data is necessary for a reference system and for better understanding of the fracture mechanism.

3.2 Experimental

Tube specimens are internally pressurized with argon in order to produce a biaxial tensile stress state. Rupture lifetimes are measured as a function of stress, temperature, and equivalent pressure of iodine, which impinges on the zircaloy surfaces as a molecular beam on a spot of 0.5 cm diameter. Figure 3-1 is a photo of the apparatus, which can be compared with Fig. 2-1 for detailed information. The fractography of the surface is observed by SEM.

3.3 Materials

Two lots of stress relieved zircaloy-2 were tested. One lot was obtained from SRI International (O.D. = 0.503" [12.8 mm], I.D = 0.453" [11.5 mm]; the other lot was purchased from Sandvik Special Metals, lot number 9AX 32 (O.D. = 0.486 ± 0.002" [12.3 mm], I.D. = 0.414 ± 0.002" [10.5 mm]). Table 3-1 gives the chemical composition. The Sandvik tubes were thinned down mechanically from the outside surface to 0.25 mm wall thickness in order to decrease the pressure of argon gas needed for the desired hoop stresses (see Fig. 2-1).

3.4 Results

3.4.1 Failure Modes With iodine, the majority of specimens exhibited pinhole-type failure (Figs. 3-1 through 3-6)), which was completely different from the burst-type failure which occurred in the absence of iodine (Fig. 3-7). The Sandvik specimens with stresses between 372 MPa and 290 MPa all fractured in the pinhole model. Iodine SCC was not observed below a threshold stress (see Section 3.5.3). Two specimens with stress > 379 MPa fractured in non-pinhole mode, even in the presence of iodine. They will be discussed in Section 3.5.4.

The fractography of pinhole and ductile failure are completely different. Figure 3-8 is a scanning electron micrograph of pinhole type failure. Figure 3-9 is for ductile failure. Figure 3-10 shows that besides the penetrating cracks, there are a number of non-penetrating cracks on the outside surface in the iodide-affected region. There are numerous small cracks branching out from the main crack at an angle to main crack propagation direction (Figure 3-11). As the main crack propagates, the remaining intact wall thickness decreases, so that the net section stress increases. After the crack length reaches a critical length, a transition to ductile failure occurs (Fig. 3-12) when the net section stress reaches the ultimate tensile stress and the tube fails immediately (see Eq. 3-4). Grains fail by cleavage, as shown in Fig. 3-13.

3.4.2 Time to Rupture The results from unflawed specimens from SRI are plotted in Fig. 3-14. Preflawed (25 μm deep, 25 mm long notches) data are shown in Fig. 3-15. Stress corrosion cracking was

observed at iodine pressure as low as 10^{-3} torr. The iodine pressure necessary to cause stress corrosion cracking is much less than previously reported.[20]

Control specimen results for the Sandvik tubes at 300°C and time to failure versus stress at fixed iodine pressure and temperature are shown in Fig. 3-16 for comparison. Figure 3-17 gives the time-to-failure versus temperature for fixed stress and iodine pressure tests, and Fig. 3-18 is a time-to-failure/equivalent pressure relationship for Sandvik tubes.

3.5 Discussion

3.5.1 Iodine Concentration Most other studies use mg/cm^2 as a unit to describe the iodine potential. According to basic chemistry, the partial pressure is the correct measure of chemical potential. Une[22] performed experiments with different volume-to-surface ratios, keeping one variable constant and changing the other. The influence of the two variables on the time to failure was recorded. He concluded that in zircaloy stress corrosion cracking, the iodine partial pressure (e.g. torr), not the surface density (mg/cm^2) is the correct unit for correlating the stress corrosion cracking phenomenon. We consider below the experimental methods for establishing the iodine concentration used in previous investigations:

(A) A fixed amount of iodine is sealed in the inside of a zircaloy tube.[13,16] In this case, there is considerable surface other than zircaloy on which iodine can plate out. In addition, only the zircaloy is heated and the iodine will

condense on the cold regions of the system. The actual iodine responsible for stress corrosion cracking is much lower than what is reported.

(B) A fixed amount of iodine is sealed inside the zircaloy tube, and the tube is plugged at both ends,[4,5,7,8,14,17] or iodine is sealed with zircaloy in closed system, as in some mandrel tests.[1,6,11] In these cases, the amount of iodine first decreases with time, eventually reaching an equilibrium between gaseous iodine, zircaloy, and a scale of lower iodide.[23] The monatomic iodine pressure approaches the equilibrium value, $P_I \sim 10^{-15}$ atm, calculated by Cubiciotti,[23] but we do not know how long it will take to achieve equilibrium.

From the discussion above, it is clear that in previous investigations, insufficient attention has been given to maintaining constant, known iodine concentration or even using the correct units to describe the iodine concentration.

3.5.2 Biaxiality In our specimen assembly (Fig. 2-1), one end is free. Under internal pressure, the hoop-axial stress is two (in other works, the ratio is between 2 and 1 or not given[8]). The yielding condition of anisotropic materials such as zircaloy under biaxial loading depends on the ratio of two principal stresses,[24,25] so a hoop stress measurement alone is not a sufficient condition for fixing the time to failure. The time to failure can change with different stress biaxiality ratios even though the hoop stress, iodine pressure, and temperature are fixed.

3.5.3 Stress and Iodine Pressure Threshold One Sandvik specimen, held at 300°C and 328 MPa, did not fail after 80 hrs at an iodine pressure of 0.004 torr. A possible explanation is that the stress was below the threshold stress for stress corrosion cracking for the particular iodine partial pressure used. Alternatively, the iodine pressure was below the threshold value for that stress level. The threshold concepts are accepted by most previous workers.[1-13] The threshold concept implies a change in fracture mechanism in narrow ranges of stress and iodine pressure, so that time to failure is greatly affected.

3.5.4 High Stress Failure Two Sandvik specimens stressed near 379 MPa did not exhibit pinhole type failure under iodine, but SEM fractography still showed cleavage fracture (Fig. 3-19). In zircaloy-4, iron iodide stress corrosion (Section 5.4.1), we also found that burst-type failure predominates for stresses higher than 376 MPa, while pinhole-type failure predominates at lower stresses. Similar conclusions also were reached by Yaggee[26] for their irradiated specimens and Baty[27] in his unirradiated zircaloy stress corrosion cracking tests.

3.5.5 Data Correlation Stress corrosion cracking of zircaloy is a low-ductility fracture process (strain in the range of a few percent). If crack propagation rather than crack initiation dominates the lifetime of specimen (Chapter 6), the model of slow crack growth under chemical attack for brittle solid may be applied to this situation.[28] In this model, the crack growth rate is described in chemical reaction rate terminology by:

$$da/dt = A[P_{eq}]^n \exp(-E^*/RT)F(K) \tag{3-1}$$

where

a = crack length

E^* = activation energy of the chemical step responsible for stress corrosion cracking

n = reaction order

A = constant

$F(K)$ in Eq. 3-1 is the functional dependence of the crack growth rate on the stress intensity factor, which is

$$K = Y\sigma \sqrt{a} \tag{3-2}$$

Y = geometric factor

Integrating Eq. 3-2:

$$t_f = (1/A[P_{eq}]^n)\exp(E^*/RT) \int_{a_o}^{a_c} da/F(K) \tag{3-3}$$

a_o = initial length of the crack pre-existing through manufacture (6 μm) or machining (25 μm)

a_c = crack length at which the net section stress is equal to the ultimate tensile stress:

$$\sigma w/(w-a_c) = \sigma_{UTS} \tag{3-4}$$

Here it is supposed that stress corrosion propagates the crack from the length a_o to a_c where ductile failure takes place very rapidly. This final process can be seen on the SEM picture of Fig. 3-12.

Least square curve fitting of the T-$\dot{P}_{eq}$ data at constant stress gives

$$E^* = 7.1 \pm 0.9 \text{ Kcal/mole} = 30 \pm 4 \text{ KJ/mole} \tag{3-5}$$

and

$$n = 1.0 \pm 0.2$$

from three sets of data (Sandvik tubes, preflawed SRI, and unflawed SRI tubes) in Fig. 3-20.

Two crack velocity/stress intensity factor relations[24] were tried:

$$F(K) = \exp(BK/T) \tag{3-6}$$

$$F(K) = K^m \tag{3-7}$$

where B and m are constants. Both relationships all fit the stress-dependence data equally well. The form F(K) = exp (BK/T) is theoretically based on Eyring's absolute rate theory,[29] being a manifestation of a pressure effect on the free energy of activation.[30] The

purely empirical function $F(K) = K^m$ case gives $m = 4.0 \pm 0.1$, which is consistent with the results of Tuck[5] and Polan.[14]

Table 3-1. Composition of Sandvik Zr-Z(9AX32)

INGOT ANALYSIS
COMPOSITION IN PERCENT

	Spec.	TOP	Middle	Bottom
Sn	1.20 - 1.70	1.55	1.47	1.46
Fe	0.07 - 0.20	0.14	0.13	0.14
Cr	0.05 - 0.15	0.10	0.09	0.09
Ni	0.03 - 0.08	0.05	0.04	0.04
Fe+Cr+Ni	0.18 - 0.38	0.29	0.27	0.28
Zr		balance		

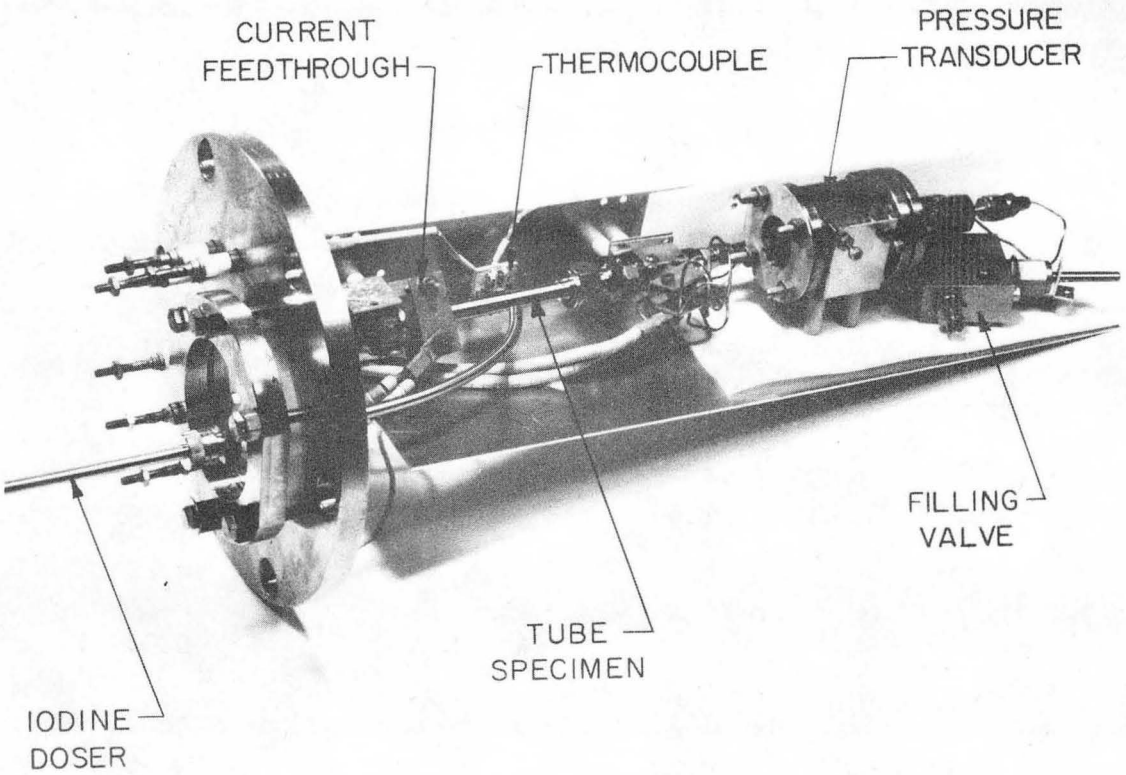

XBB 795-6560A

Figure 3-1. Photo of the stress corrosion cracking apparatus.

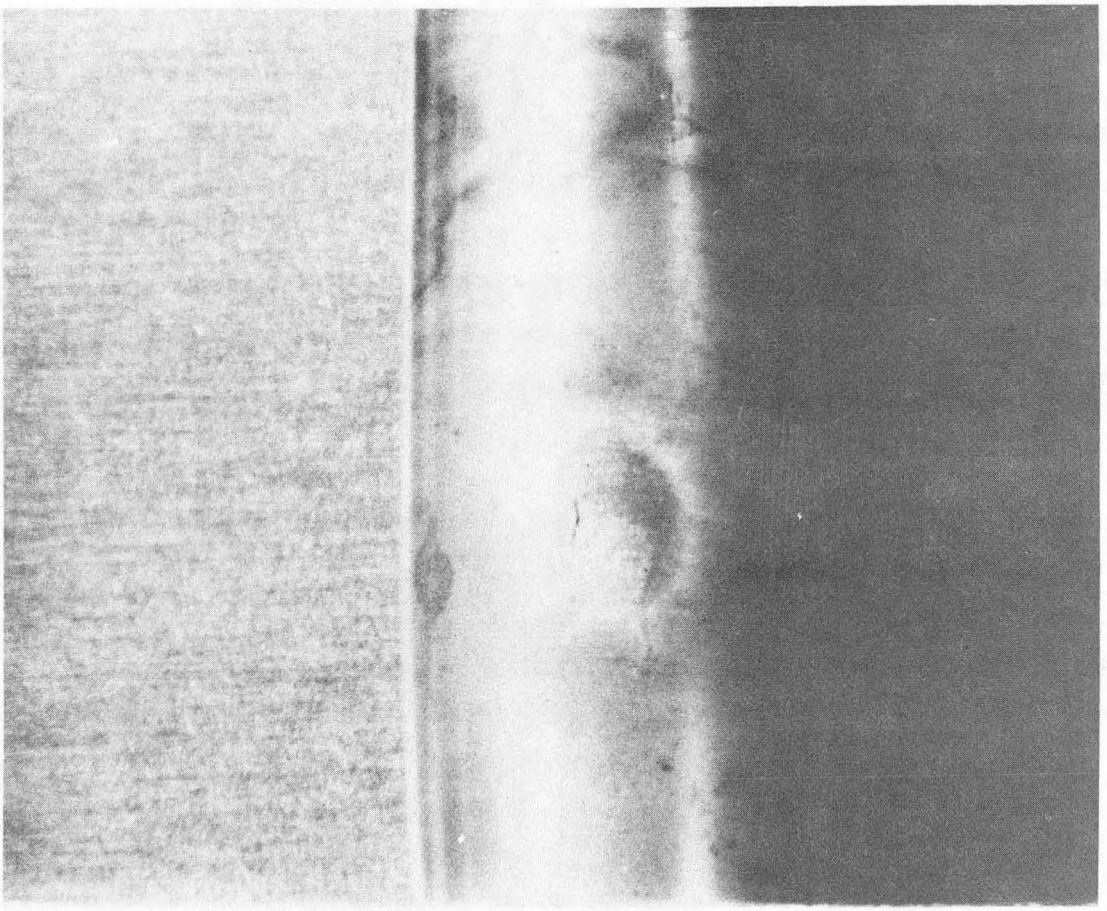

XBB 791-473

Figure 3-2. Stress relieved Zr-2 (Sandvik lot no. 9AX32) failed after 13.2 hrs under 316 MPa and 0.014 torr iodine at 300°C.

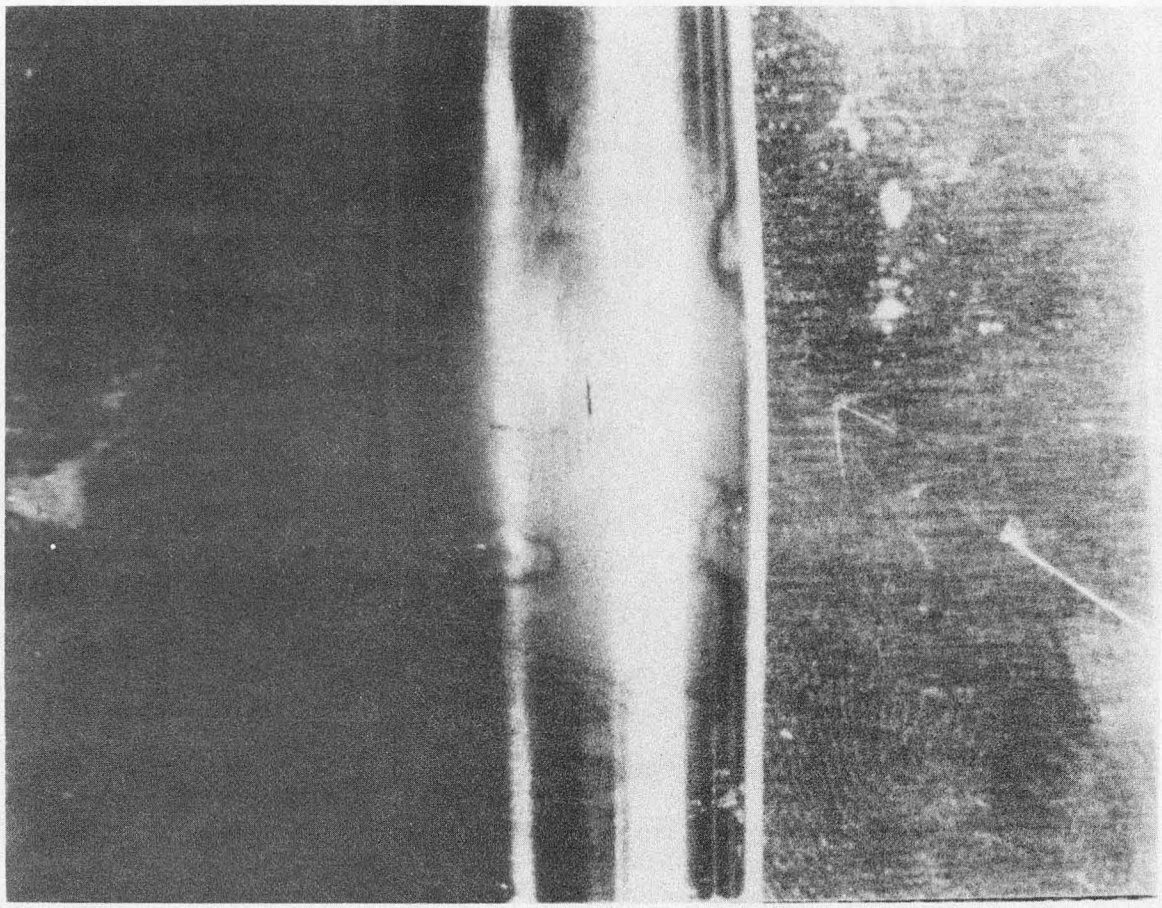

XBB 791-482

Figure 3-3. Stress relieved Zr-2 (Sandvik lot no. 9AX32) failed after 5.0 hrs under 369 MPa and 0.014 torr iodine at 300°C.

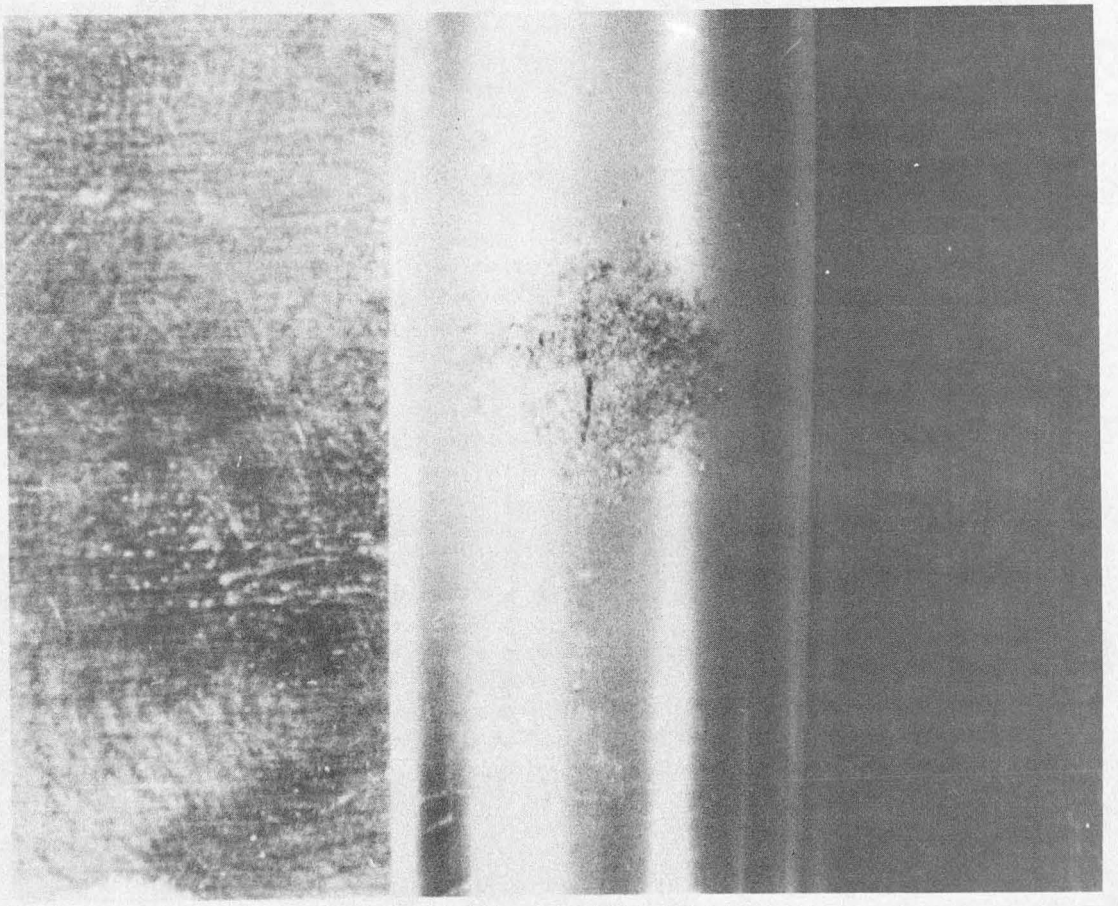

XBB 791-474

Figure 3-4. Stress relieved Zr-2 (Sandvik lot no. 9AX32) failed after 9.0 hrs under 369 MPa and 0.01 torr iodine at 300°C.

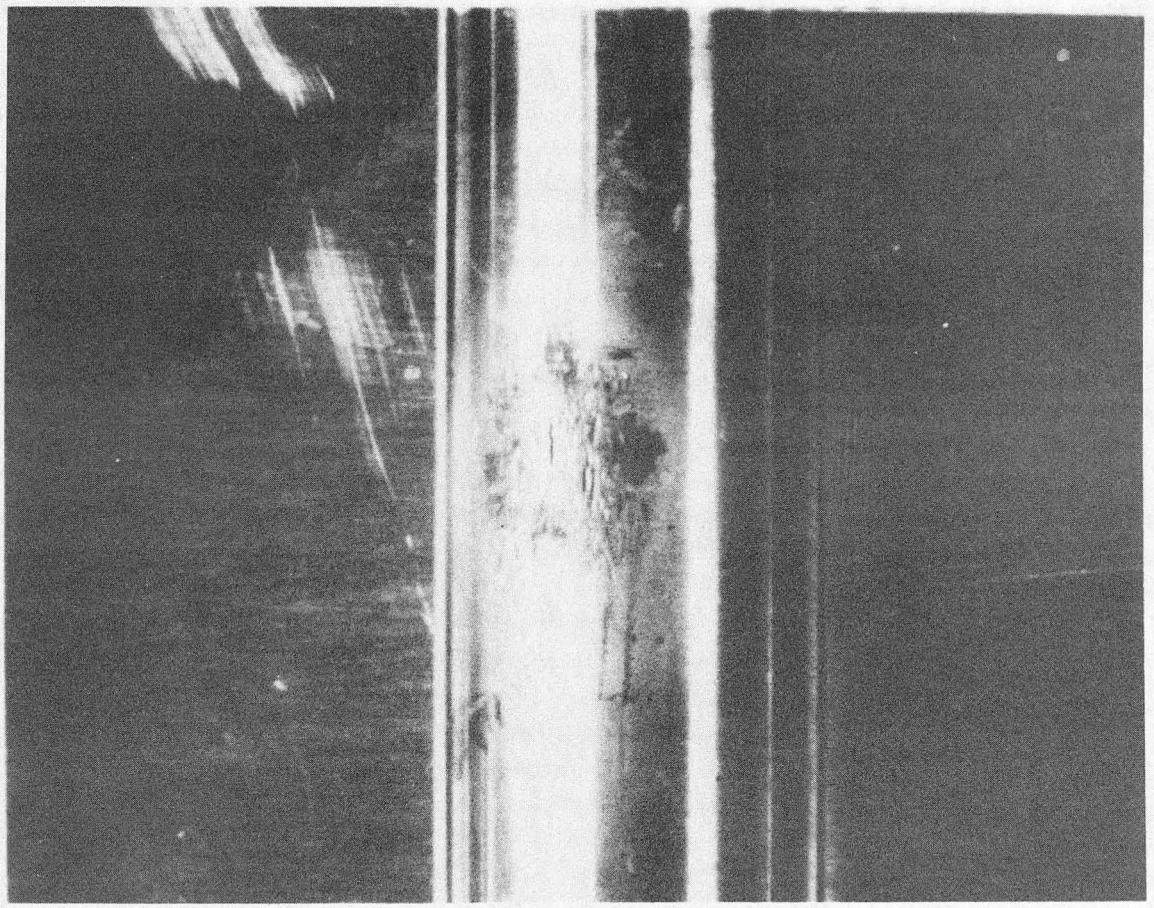

XBB 791-476

Figure 3-5. Stress relieved Zr-2 (Sandvik lot no. 9AX32) failed after 3.2 hrs under 324 MPa and 0.02 torr iodine at 325°C.

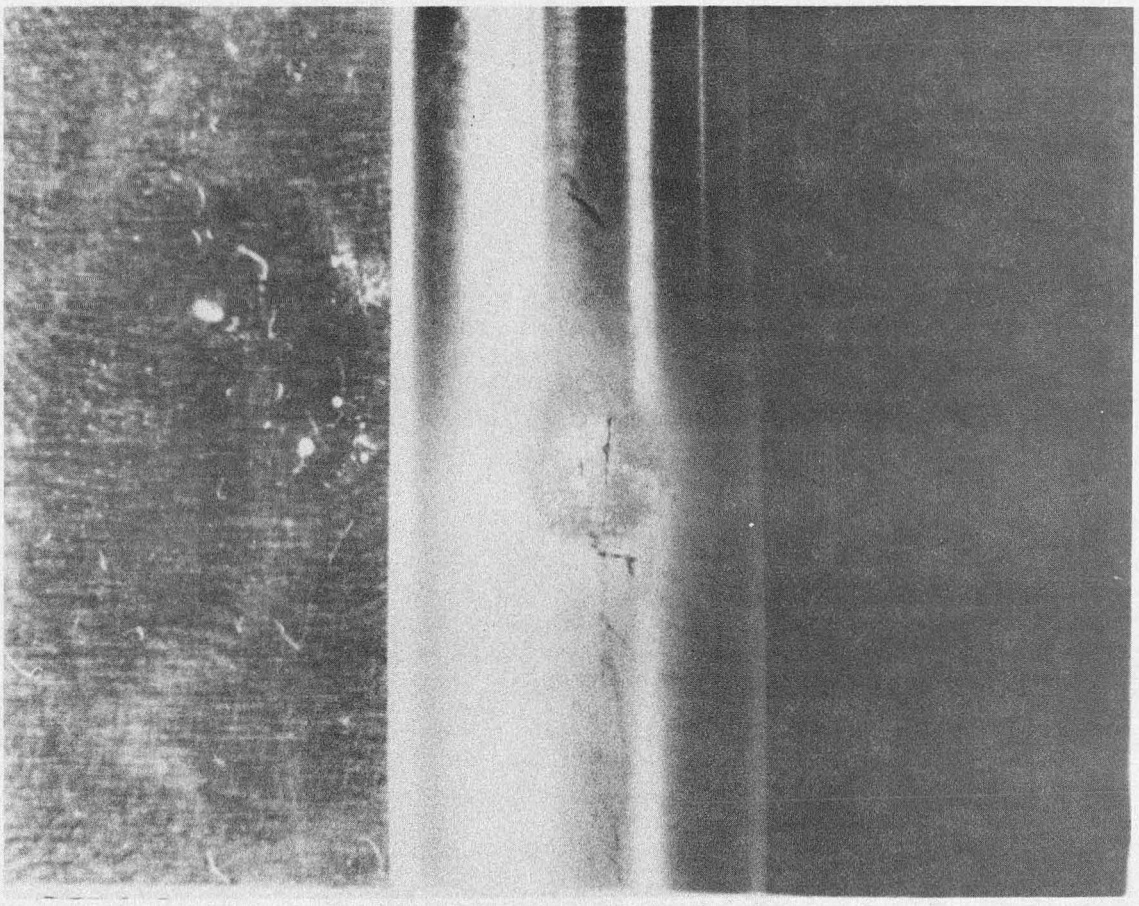

XBB 791-481

Figure 3-6. Stress relieved Zr-2 (Sandvik lot no. 9AX32) failed after 17.0 hrs under 311 MPa and 0.014 torr iodine at 270°C.

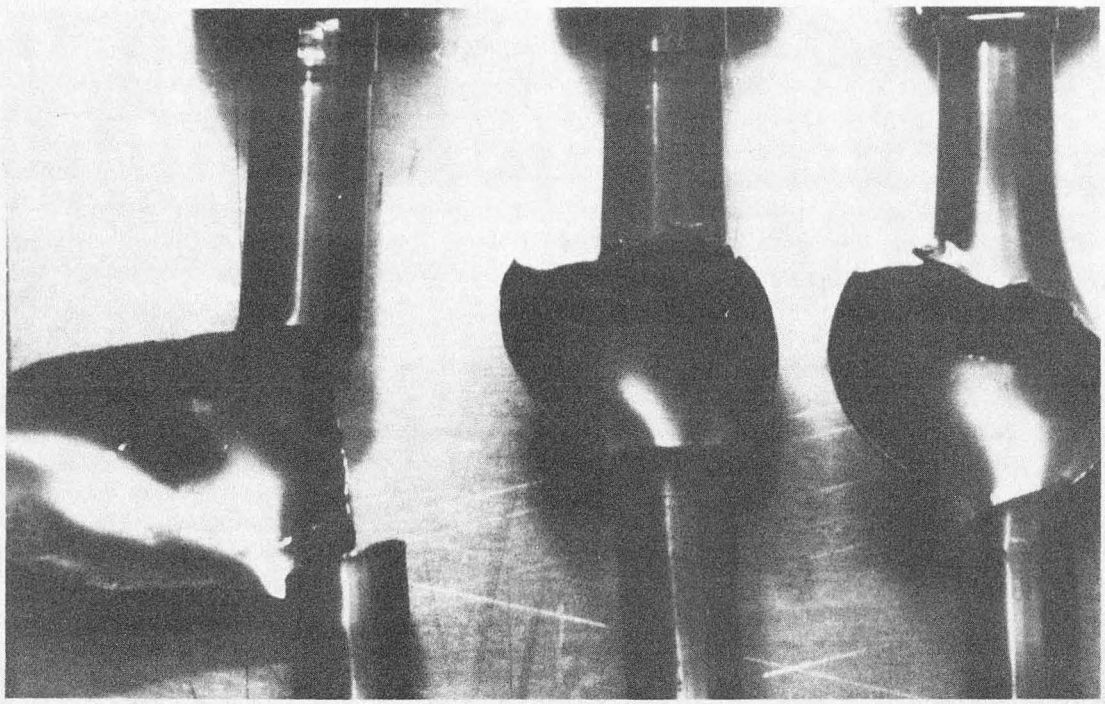

XBB 791-329

Figure 3-7. Control specimens of Sandvik lot no. 9AX32 ruptured at 300°C without iodine at stresses of 383, 370, and 343 MPa.

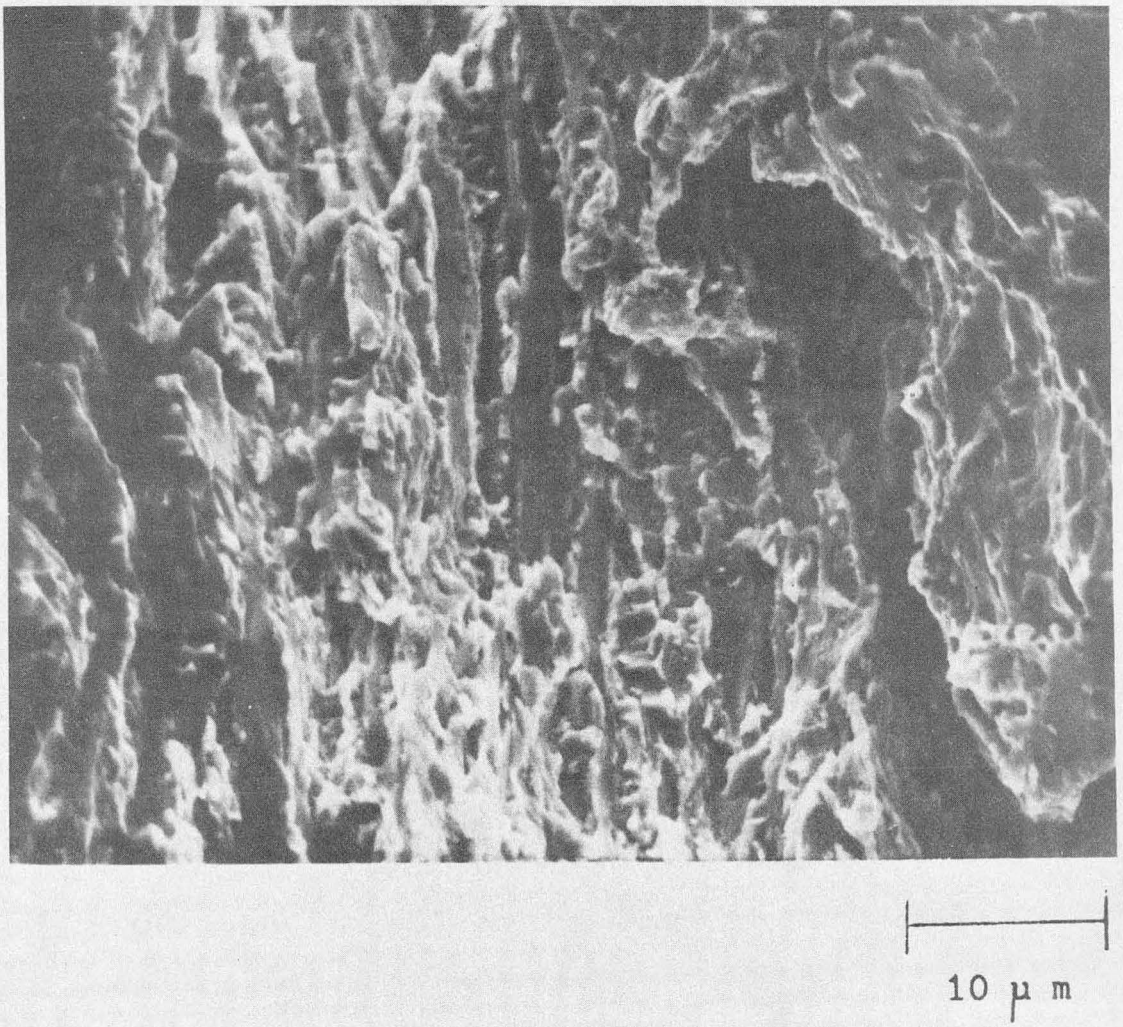

XBB 816-5516

Figure 3-8. SEM fractory of pin-hole type failure (preflawed stress relieved Zr-2 from SRI) failed after 5.9 hrs under 361 MPa 0.025 torr iodine, and 320°C.

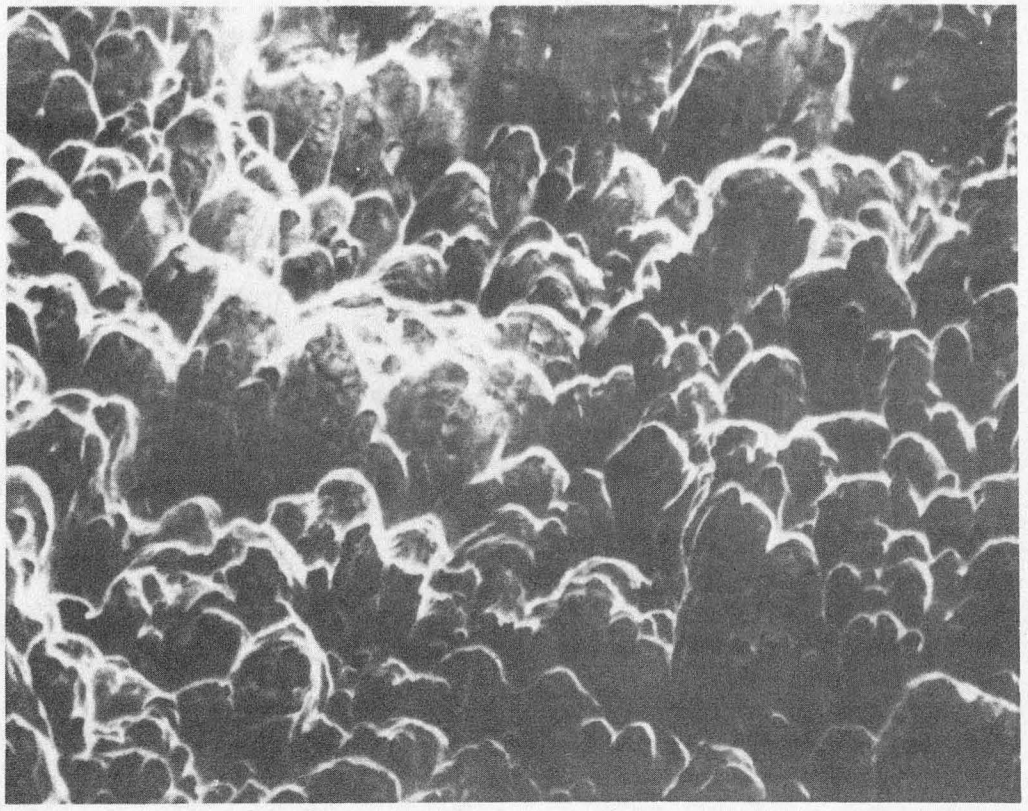

40 μ m

XBB 816-5501

Figure 3-9. SEM fractography of ductile failure (unflawed, stress relieved Zr-2 from SRI); failed after 51.8 hrs at 364 MPa and 320°C without iodine.

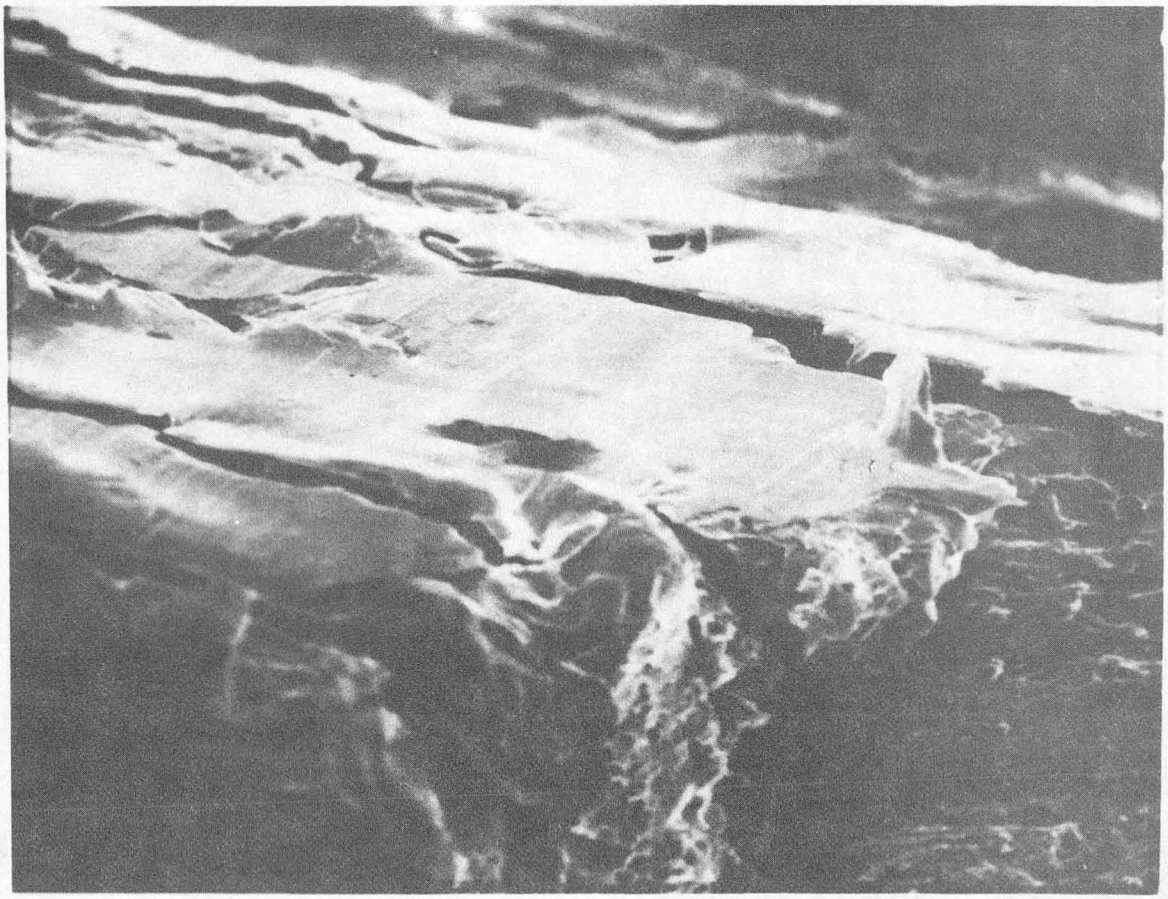

40 μ m

XBB 816-5533

Figure 3-10. Besides the main penetrating crack, there are many small cracks in iodine affected area. (Preflawed stress relieved Zr-2 from SRI failed after 59.3 hrs; 361 MPa, 0.025 torr iodine, 320°C).

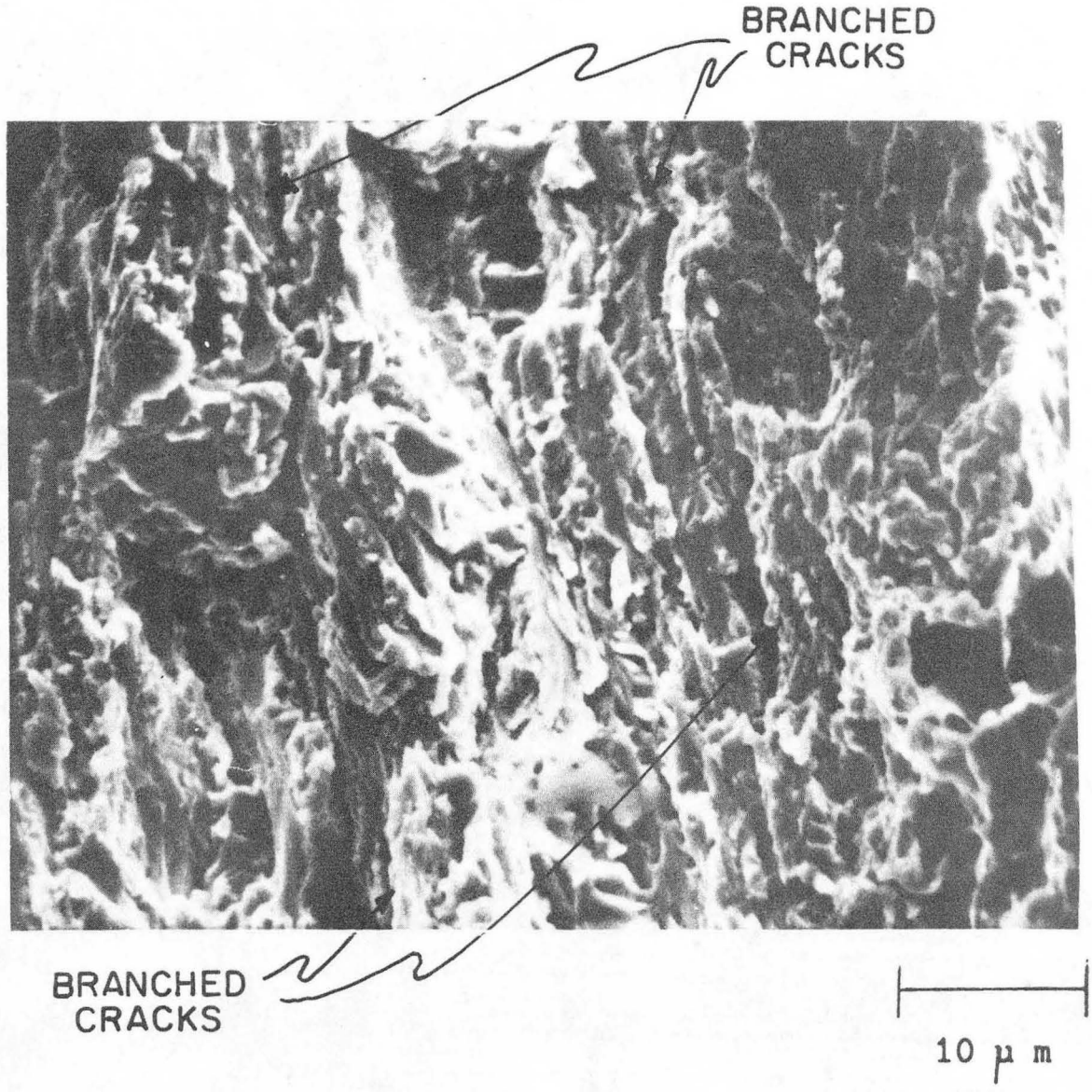

XBB 816-5523A

Figure 3-11. Same specimen as Fig. 3-8 showing many small cracks branching out from the main crack.

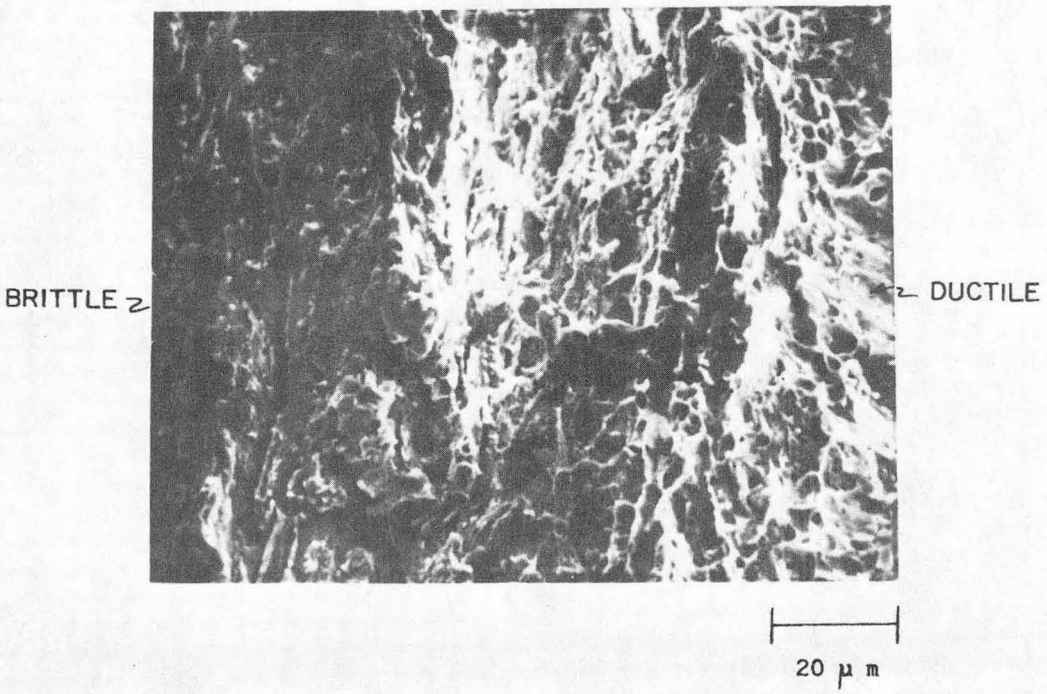

XBB 816-5500A

Figure 3-12. Transition from brittle mode to ductile dimple mode.

4 μm

XBB 816-5496

Figure 3-13. Grains failed by cleavage (preflawed stress relieved Zr-2 from SRI failed after 5.9 hrs; 361 MPa, 0.025 torr iodine, 320°C).

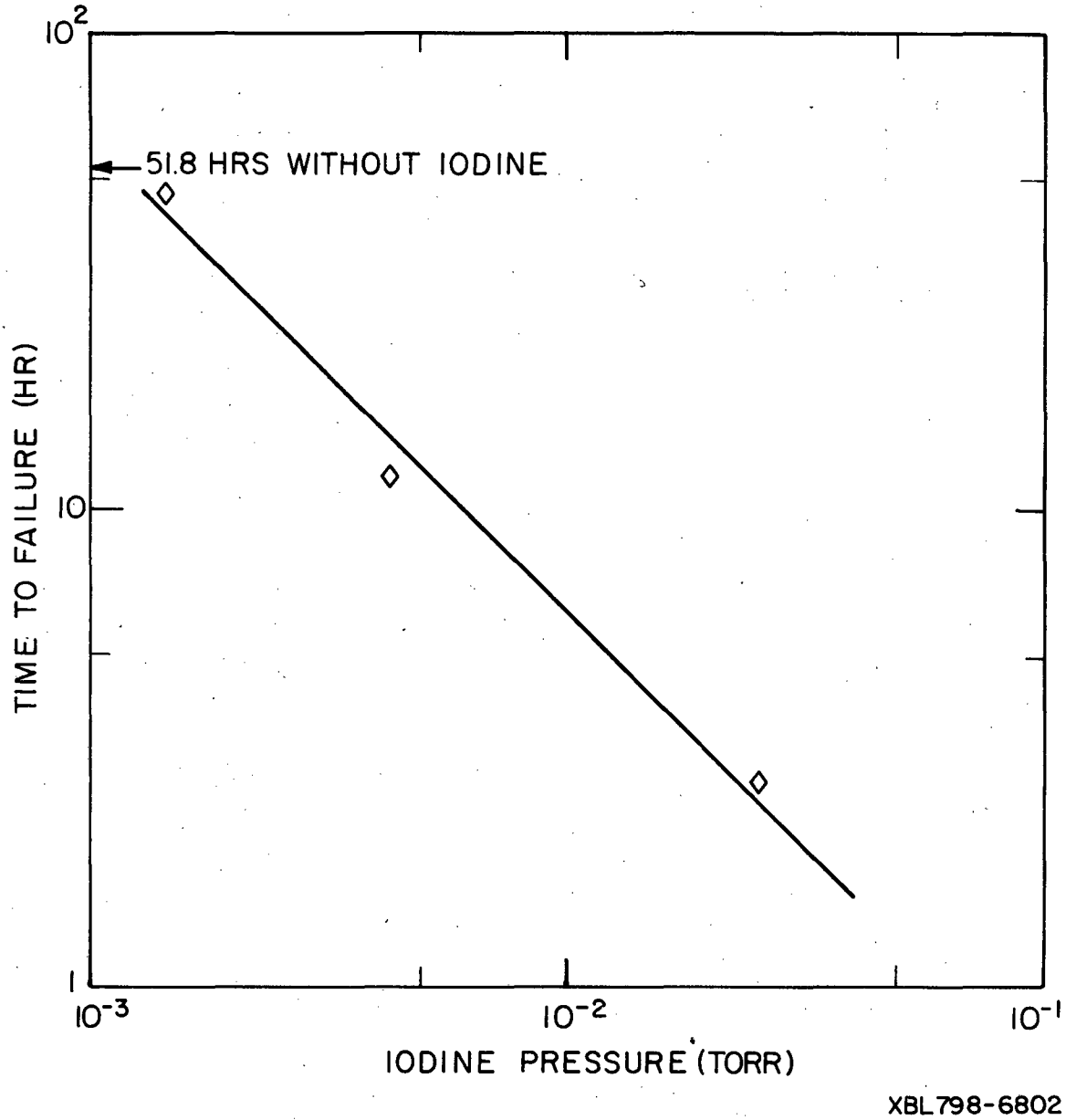

Figure 3-14. Time to failure vs. iodine pressure relation for unflawed SRI specimens.

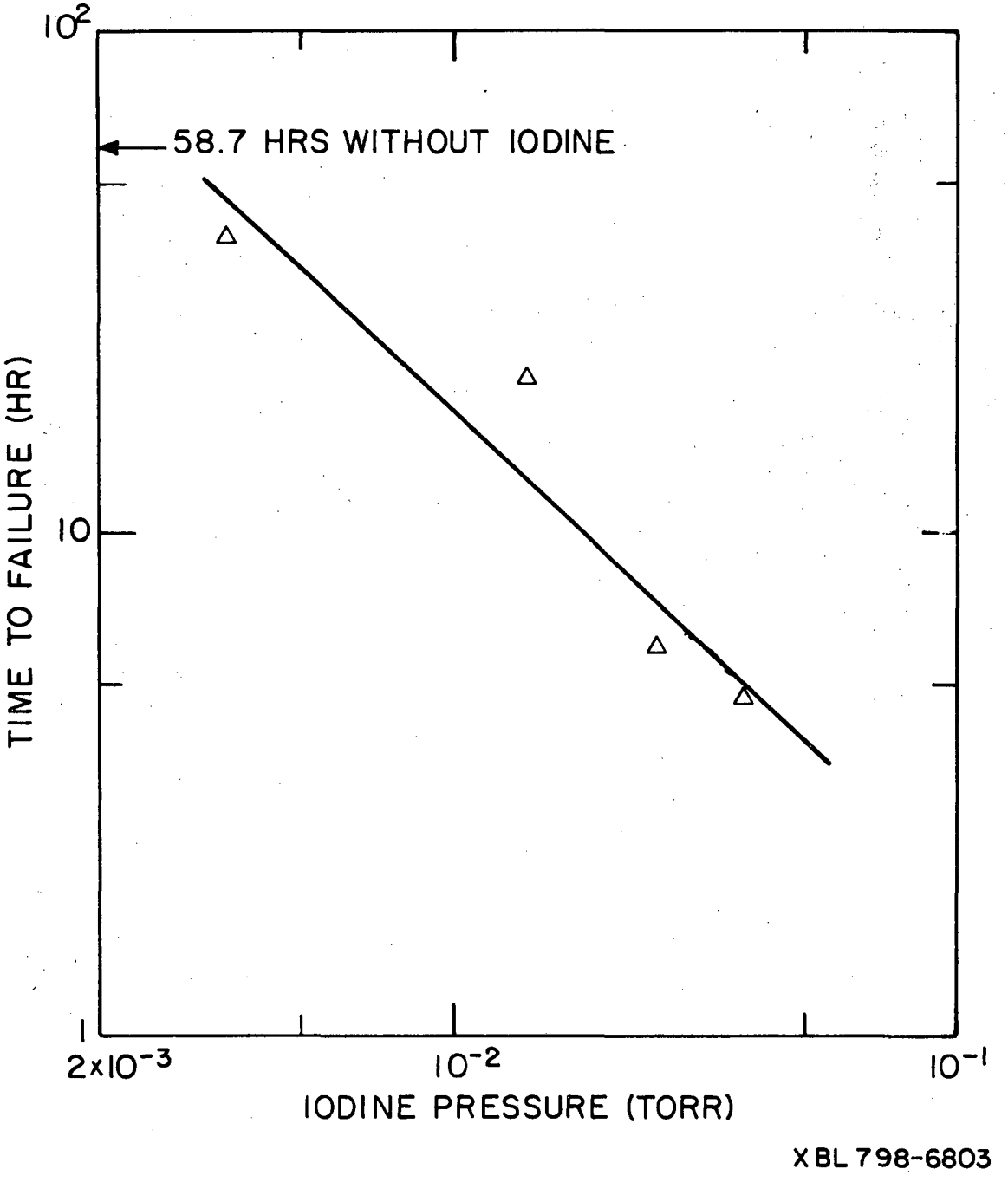

Figure 3-15. Time to failure vs. iodine relationship pressure for preflawed SRI specimens.

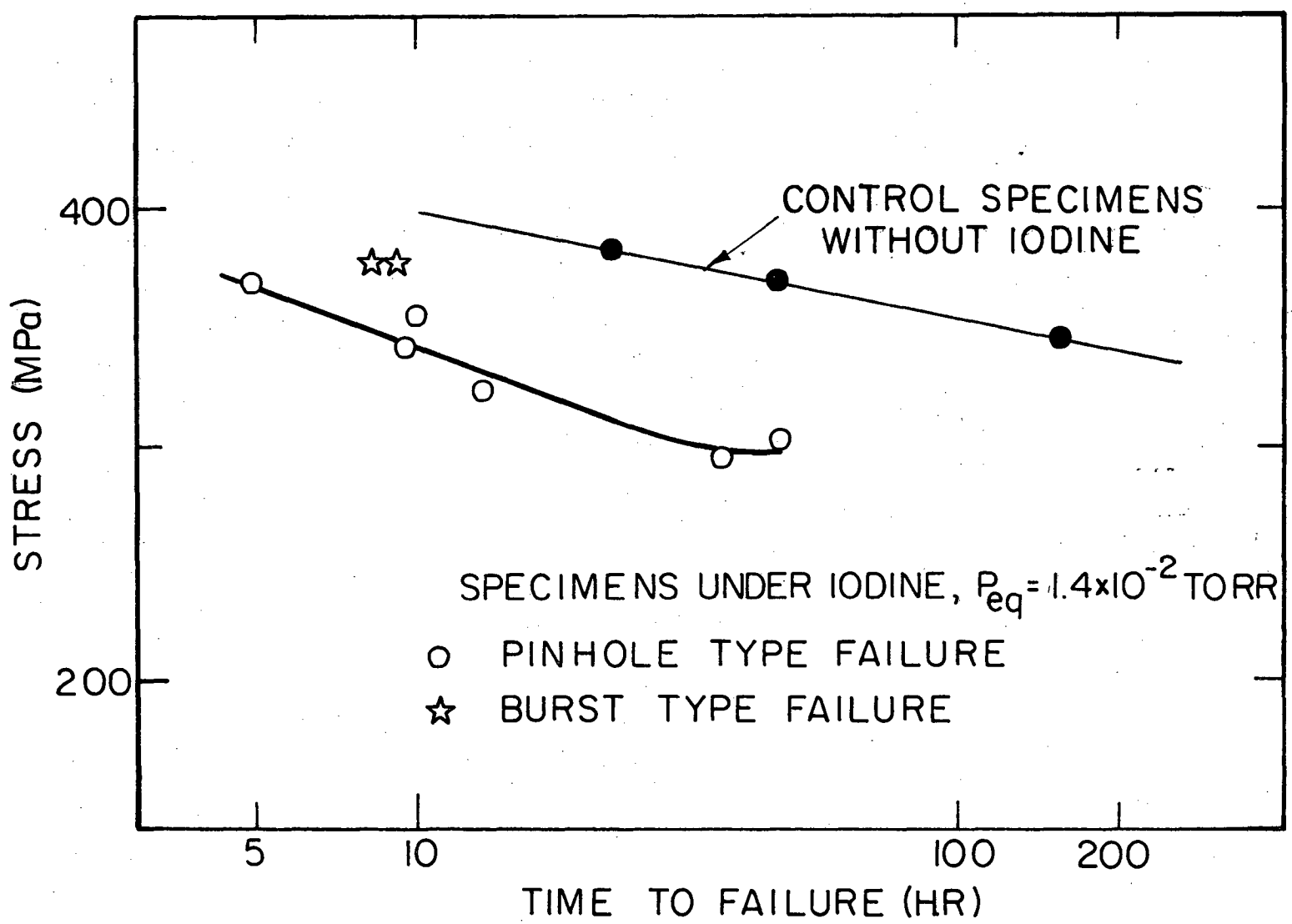

Figure 3-16. Time to failure vs. stress relations for control specimens without corrosive agent and specimens under 0.014 torr iodine at 300°C (Sandvik specimens).

XBL812-5220A

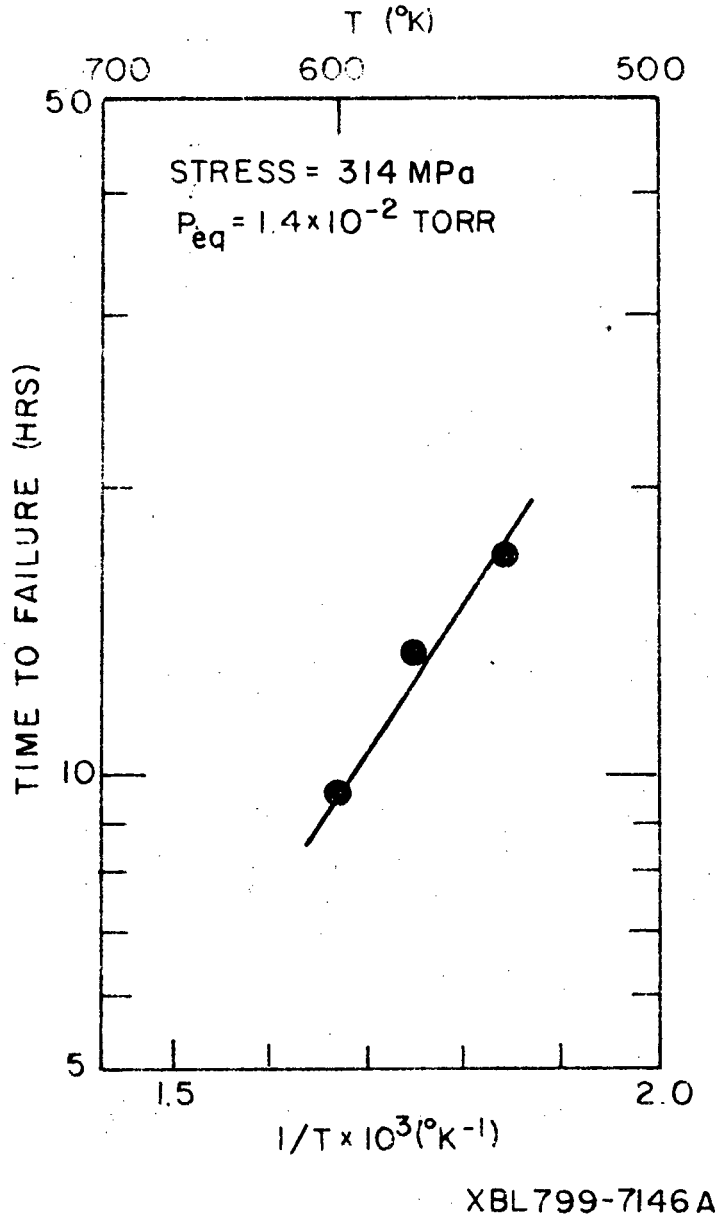

Figure 3-17. Time to failure vs. temperature relationship for Sandvik specimens at 314 MPa and 0.014 torr iodine pressure.

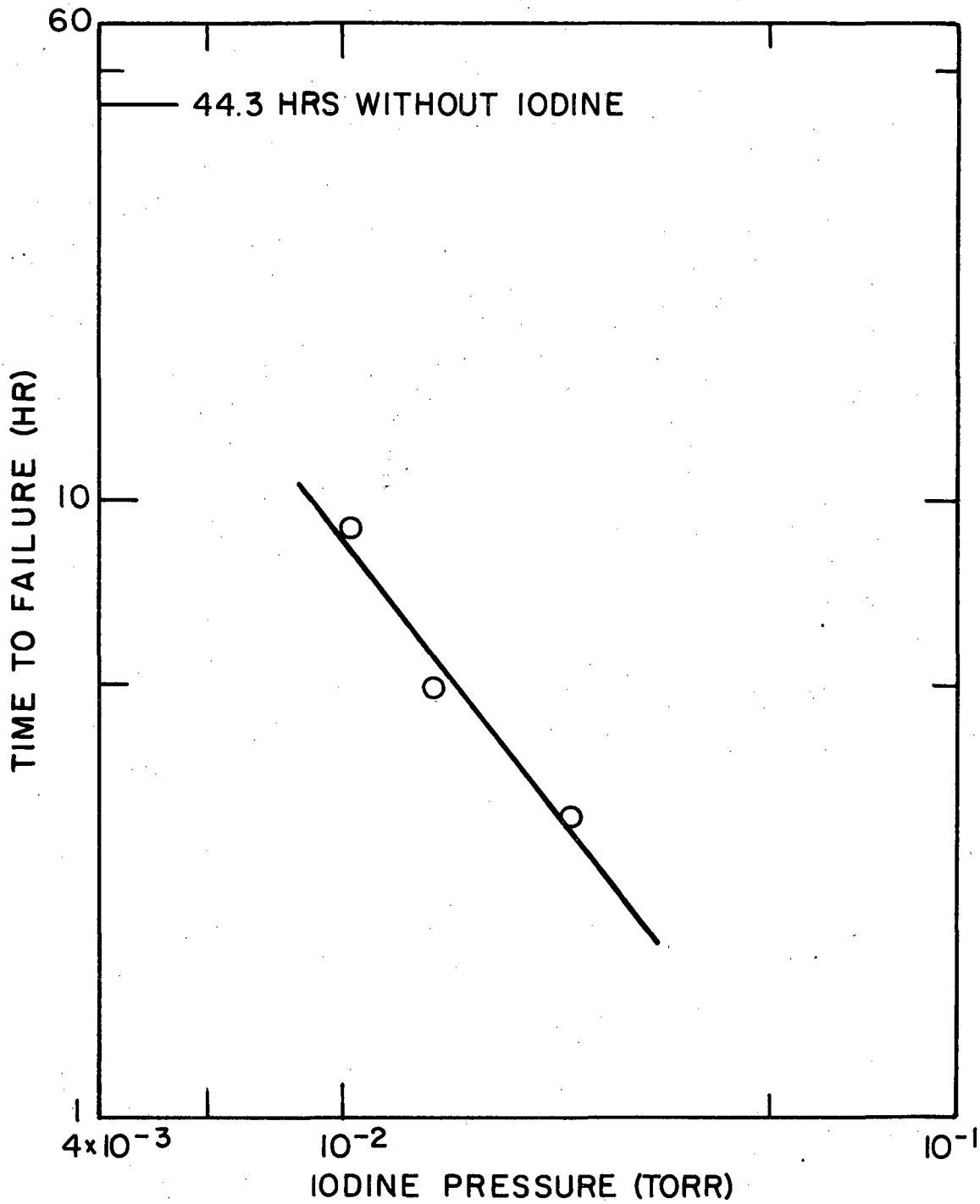

XBL 798-6804

Figure 3-18. Time to failure vs. iodine pressure for Sandvik specimens at 369 MPa and 300°C (the rupture time = 44.3 hrs for control specimen).

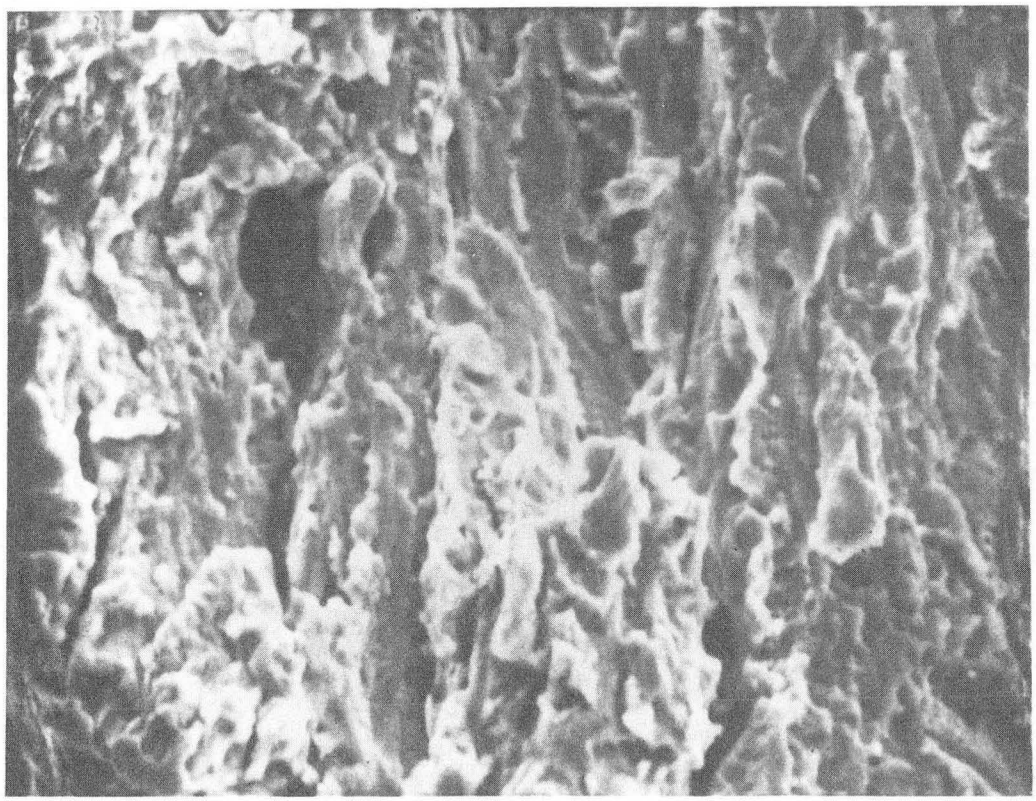

10 μ m

XBB 816-5520

Figure 3-19. SEM fractography of a burst type failure 379 MPa, 300°C, 0.014 torr iodine pressure after 8.2 hrs. Cleavage (brittle) characteristics are similar to those in pinhole-type failure.

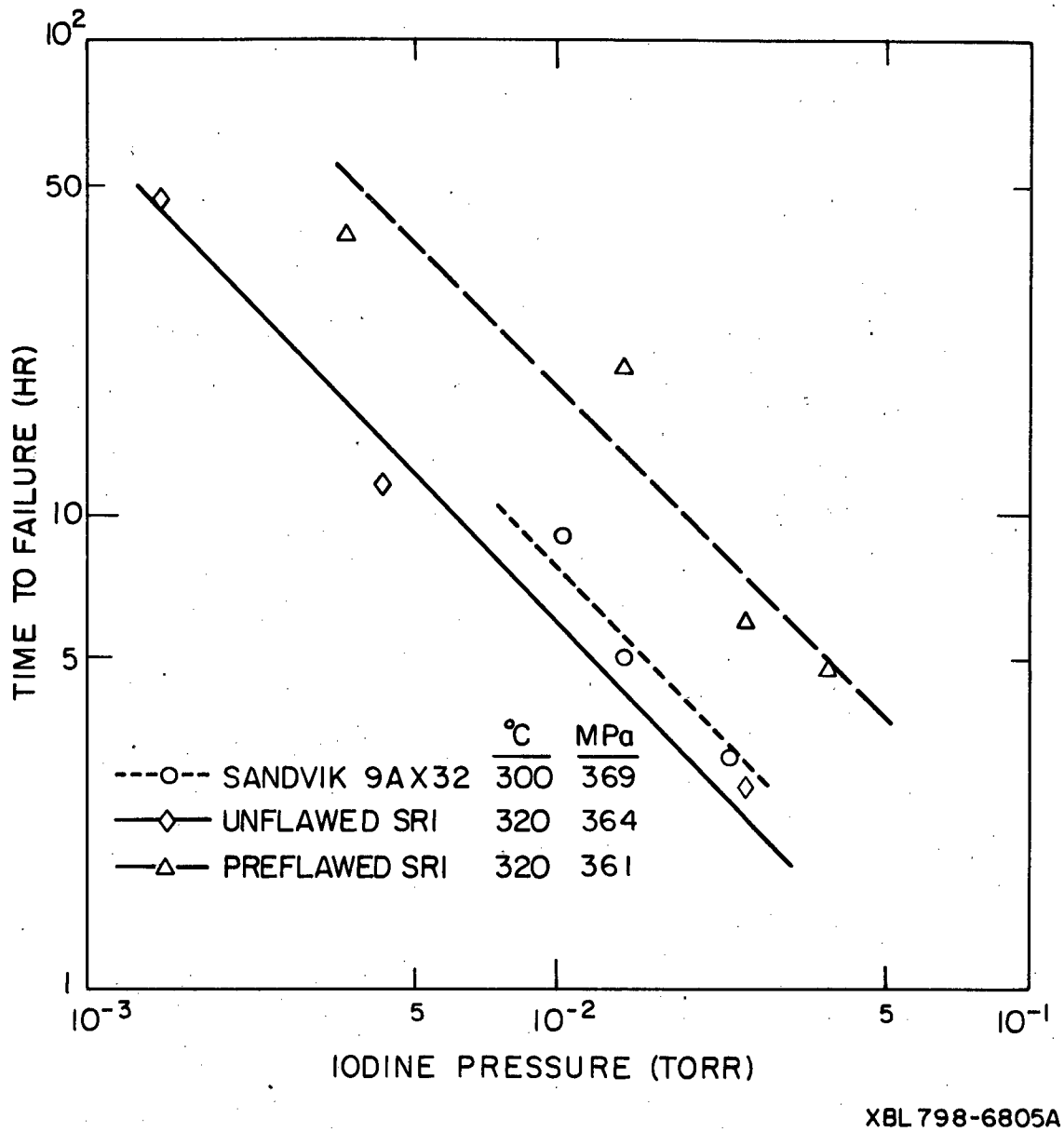

Figure 3-20. Time to failure vs. iodine equivalent pressure for three lots of zircaloy tubes.

4. ALUMINUM IODINE STRESS CORROSION CRACKING OF ZIRCALOY

4.1 Introduction

The study of iodine stress corrosion cracking of zircaloy showed that this phenomenon can occur at very low iodine partial pressure ($\sim 10^{-3}$ torr) (Section 3.4.2). According to thermodynamics, inside a reactor fuel pin, iodine will be present mainly as cesium iodide. There is some possibility that other kinds of iodides can exist at low partial pressure, which provides a reason for investigating metal iodide SCC.

4.2 Experimental

The apparatus is the same as that used in the iodine experiments (Section 2.1 and 3.2), except that a Knudsen cell replaces the iodine doser. Aluminum iodide crystals are placed in the Knudsen cell and heated to create a molecular beam which impinges on the zircaloy specimen. Thermodynamic analysis suggests that only one major species, AlI_3 (g), is present in the vapor phase. The vapor pressures of all other components are several orders of magnitude lower (Appendix B).

4.3 Materials

Stress relieved zircaloy-2 from Sandvik Special Metals, lot No. 9AX32, was studied. Detailed information about the tube is given in Table 3-1. The specimens were machined down to 0.25 mm wall thickness from the outside surface as discussed in Section 3.3.

4.4 Results

Figure 4-1 gives the results of failure time versus equivalent aluminum iodide pressure. For the same time-to-failure, aluminum

iodide can cause stress corrosion cracking at lower pressure than iodine.

4.5 Discussion

4.5.1 Fractography Although there are both pinhole- and burst-type failure under aluminum iodide, as shown in Fig. 4-1, the fracture surfaces of both types are of the cleavage brittle mode which is totally different from the ductile dimple surfaces observed in control specimens without any corrosive agent. Figure 4-2 and 4-3 show the fractography of the two types of failure.

4.5.2 EDAX Examination Results Through EDAX (Energy Dispersive Analysis of X-rays) examination of the fracture surface, we detected both iodine and aluminum signals. There is a tendency for both signals to decrease on moving from the tube outside surface into the crack. Figures 4-4 and 4-5 give several test results as different positions on different specimens.

4.5.3 Data Correlation By least square curve fitting of the failed specimens, the slope of $\ln t_f$ versus $\ln P_{eq}$ plot was found to be $-2/3 \pm 0.1$ (Fig. 4-1) compared to -1 for iodine (Section 3.5.5) and iron iodide (Section 5.5.2).

4.5.4 Iodide-Affected Surface Study of Unfailed Specimens Three specimens exposed to aluminum iodide without failure for a period longer than 43 hours underwent surface examination in order to locate any cracks which had initiated. The specimen with visible cracks (unpenetrated cracks) was the one under highest aluminum iodide equivalent pressure (1.1×10^{-3} torr) among the three unfailed tubes (Fig. 4-1). Figure 4-6 is a photo of iodide-affected region of that

specimen. Many small cracks have been initiated, but it is difficult to identify which one will be the main crack. One of the initiated cracks is shown under SEM in Fig. 4-7. Figure 4-8 is a higher magnification picture of the white deposit in Fig. 4-7, quite a few of which appeared on the surface. Through EDAX analysis, the white deposits were shown to contain extremely high aluminum- and iodine-to-zirconium ratios (Fig. 4-9).

The specimen with medium aluminum iodide equivalent pressure (3.3×10^{-4} torr) did not indicate any visible cracks. However, under SEM magnification, some initiated cracks are seen (Fig. 4-10). Figure 4-11 is an SEM picture of an unfailed specimen surface with the lowest aluminum iodide equivalent pressure (8.0×10^{-5} torr). A suggestion of cracks is seen on the surface. Both surfaces (Fig. 4-10 and 4-11) without visible crack initiation exhibit aluminum and iodine EDAX signals.

From Fig. 4-7 and 4-10, we can confirm crack initiation, but it is hard to say whether the cracks in Fig. 4-11 are initiated in the substrate metal or only on a thin corrosion film over the surface. The general surface in Fig. 4-11 looks like a surface corrosion film. Whether the crack propagates into the underlying metal is uncertain. Three specimens survived without failure for 43 hrs with initiated cracks. Crack initiation occurs at very low iodide partial pressure (1.1×10^{-3}, 3.3×10^{-4}, and 8.0×10^{-5} torr). Cracks did not penetrate the wall thickness. We can draw the conclusion that crack initiation is not the only slow step which determines the time-to-failure. Crack propagation will take some portion of specimen's lifetime.

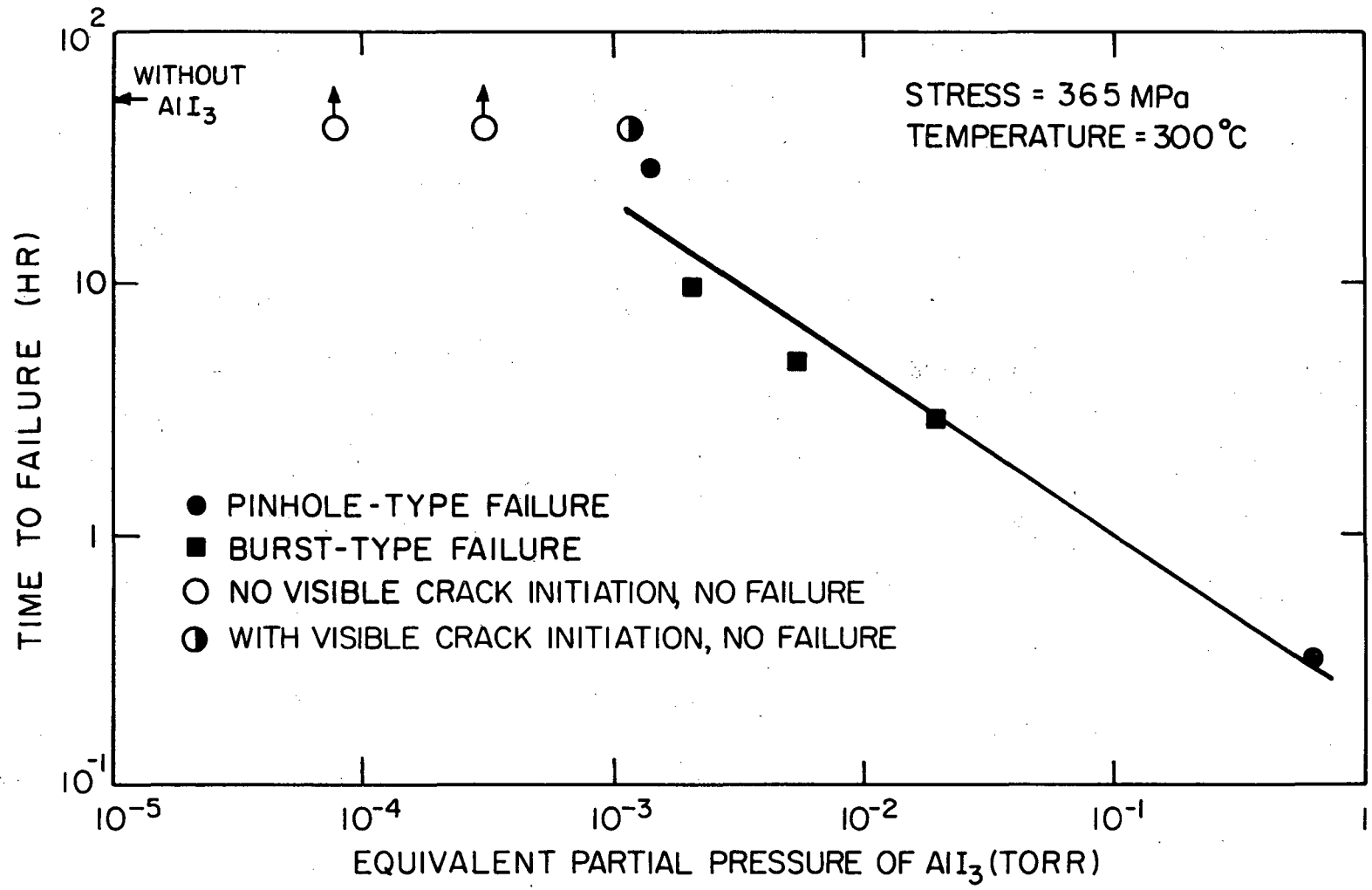

Figure 4-1. Effects of aluminum iodide exposure on zircaloy SCC: the time to failure decreases as the 2/3 power of the AlI_3 pressure.

XBL801-4595A

2 μm

4 μm

XBB 816-5505A

Figure 4-2. SEM fractography of pinhole-type failure (Zr-2 (9AX32) failed after 36.7 hrs, 365 MPa, 300°C, 1.4 x 10^{-3} torr AlI_3) cleavage, transgranular failure.

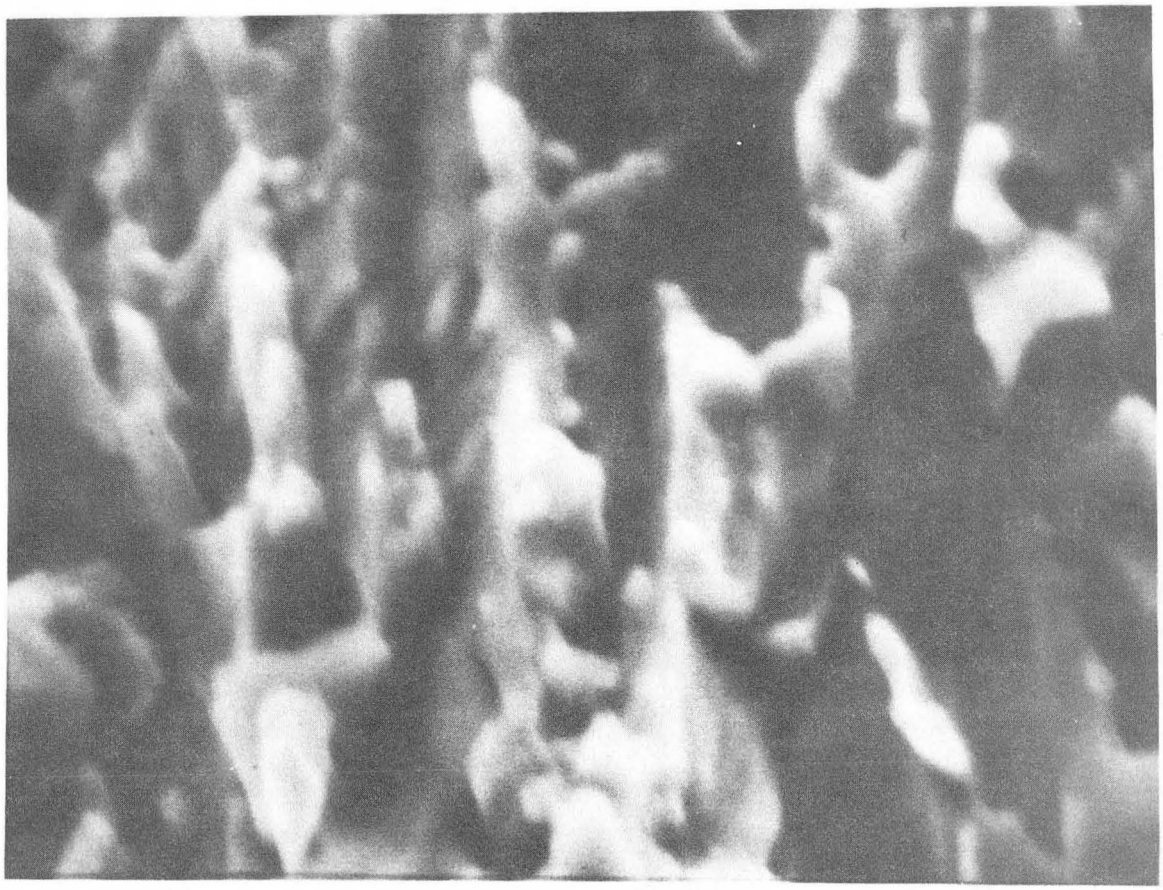

2 μm

XBB 816-5525

Figure 4-3. SEM fractography of bu-st type failure (Zr-2 (9AX32) failed after 9.4 hrs; 365 MPa, 300°C, 2.0 x 10^{-3} torr AlI_3).

Figure 4-4. Aluminum EDAX signal moving from outside surface of the tube into the crack (for different positions and different specimens) C_{Al} is the count of X-ray for aluminum, C_I is the count of X-ray for iodine, and C_{tot} is the total count of X-ray for all elements.

$P_{eq} = 1.4 \times 10^{-3}$ torr, $t_f = 36.7$ hrs: ▼ ■ ◆

$P_{eq} = 2 + 10^{-3}$ torr, $t_f = 9.4$ hrs: ○ X △ ▽

$P_{eq} = 5.1 \times 10^{-3}$ torr, $t_f = 4.8$ hrs: [] ◇ +

$P_{eq} = 2 \times 10^{-2}$ torr, $t_f = 2.9$ hrs: ▲

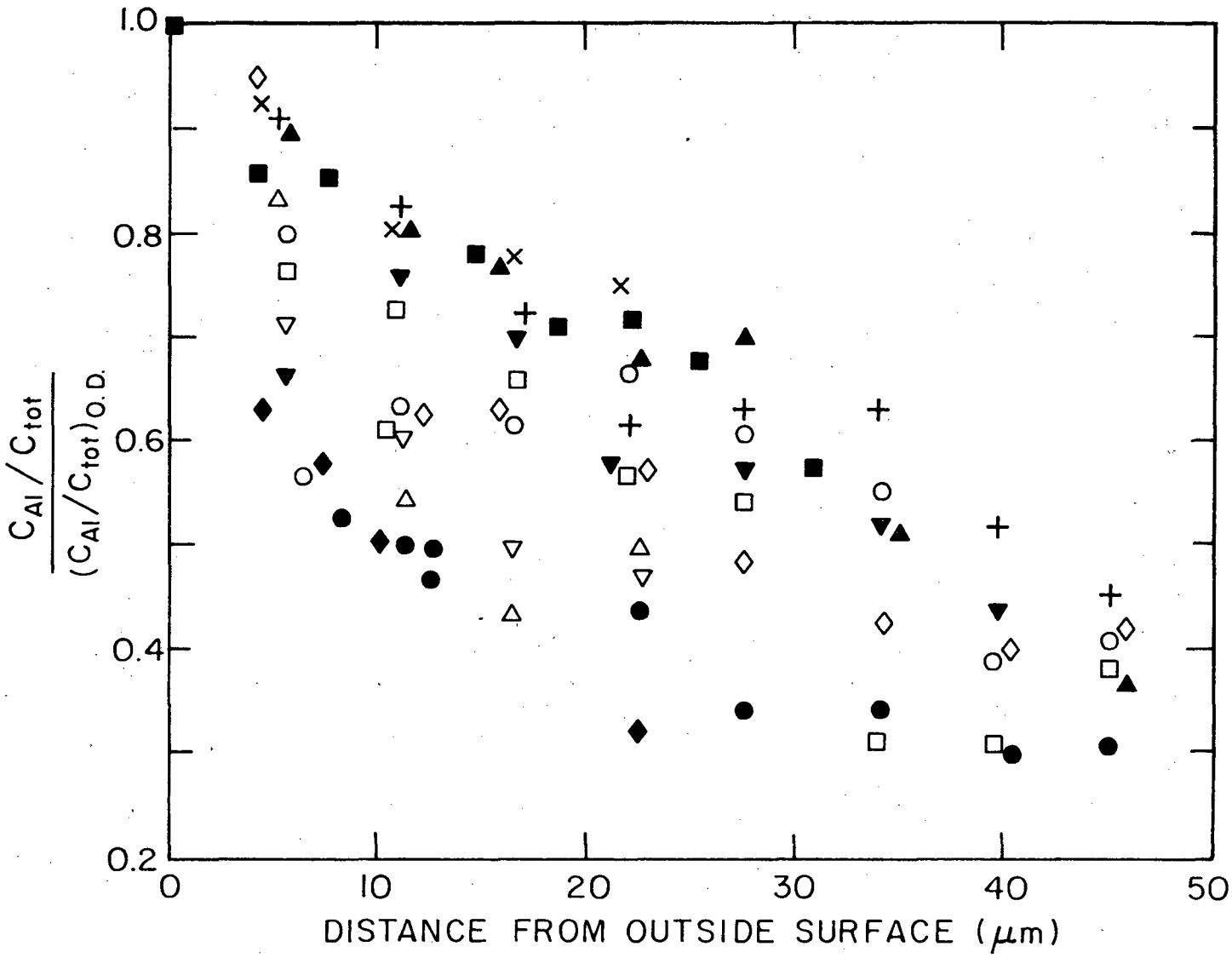

XBL 7911-7292

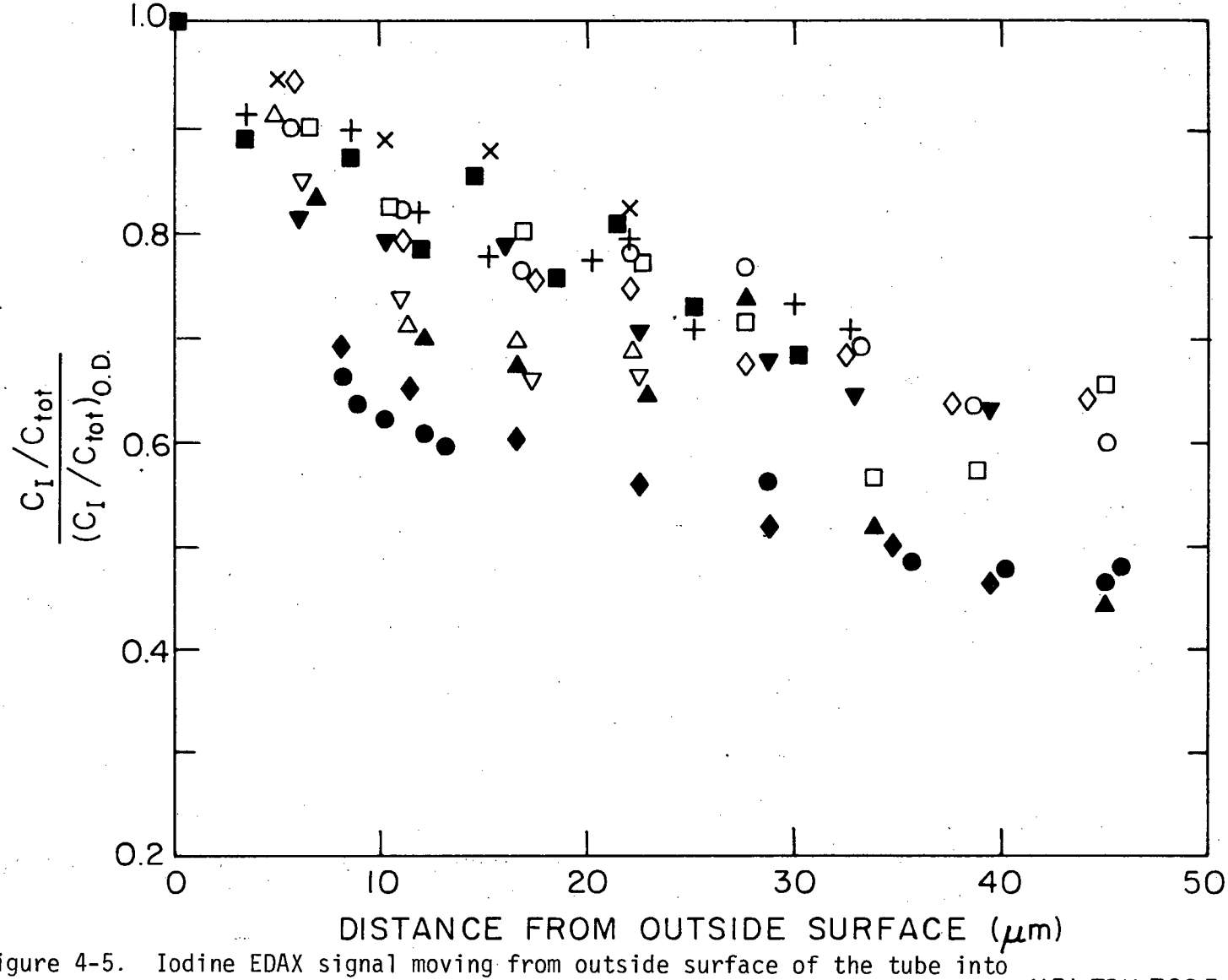

Figure 4-5. Iodine EDAX signal moving from outside surface of the tube into the crack (for different positions and different specimens).

XBL 7911-7293

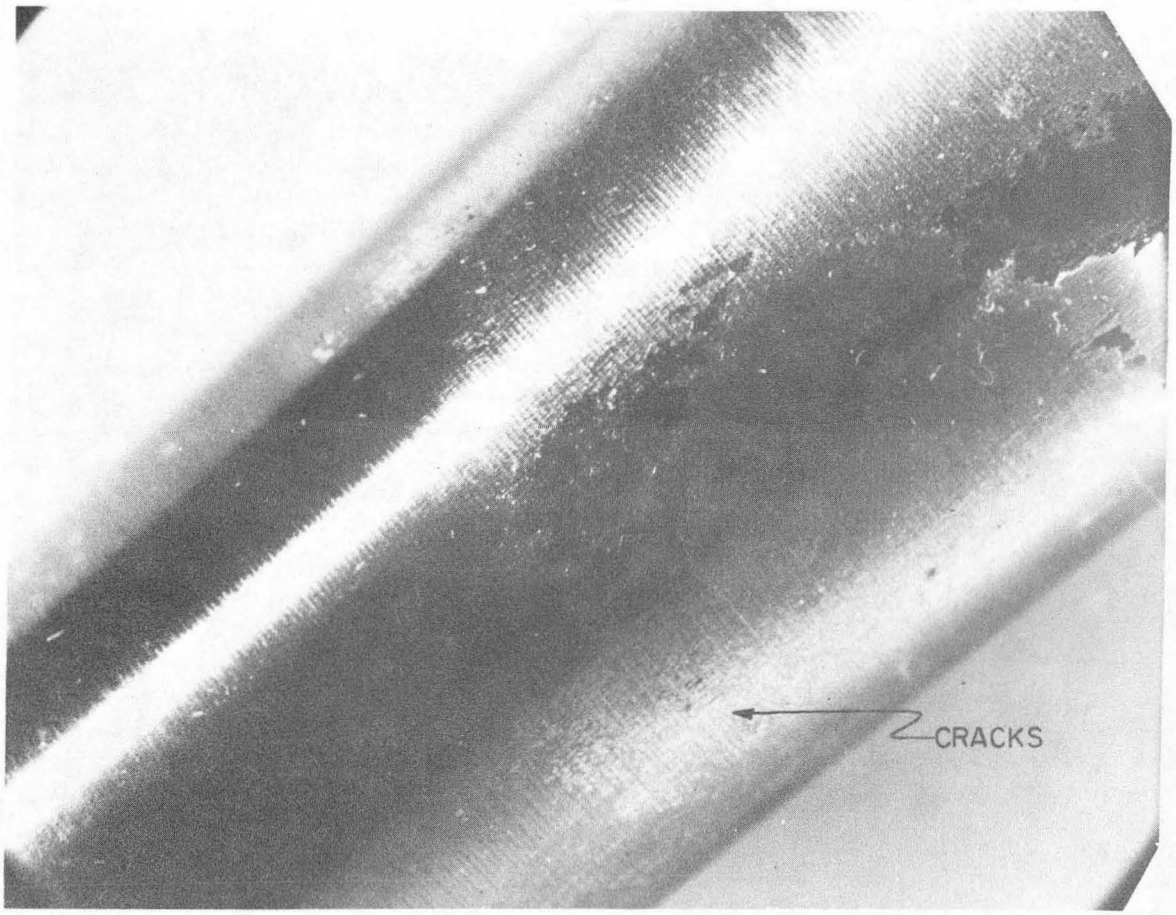

XBB 790-14811A

Figure 4-6. Unfailed specimen with visible crack initiation (1.1×10^{-3} torr AlI_3 equivalent pressure, 365 MPa, and 300°C for 43 hrs).

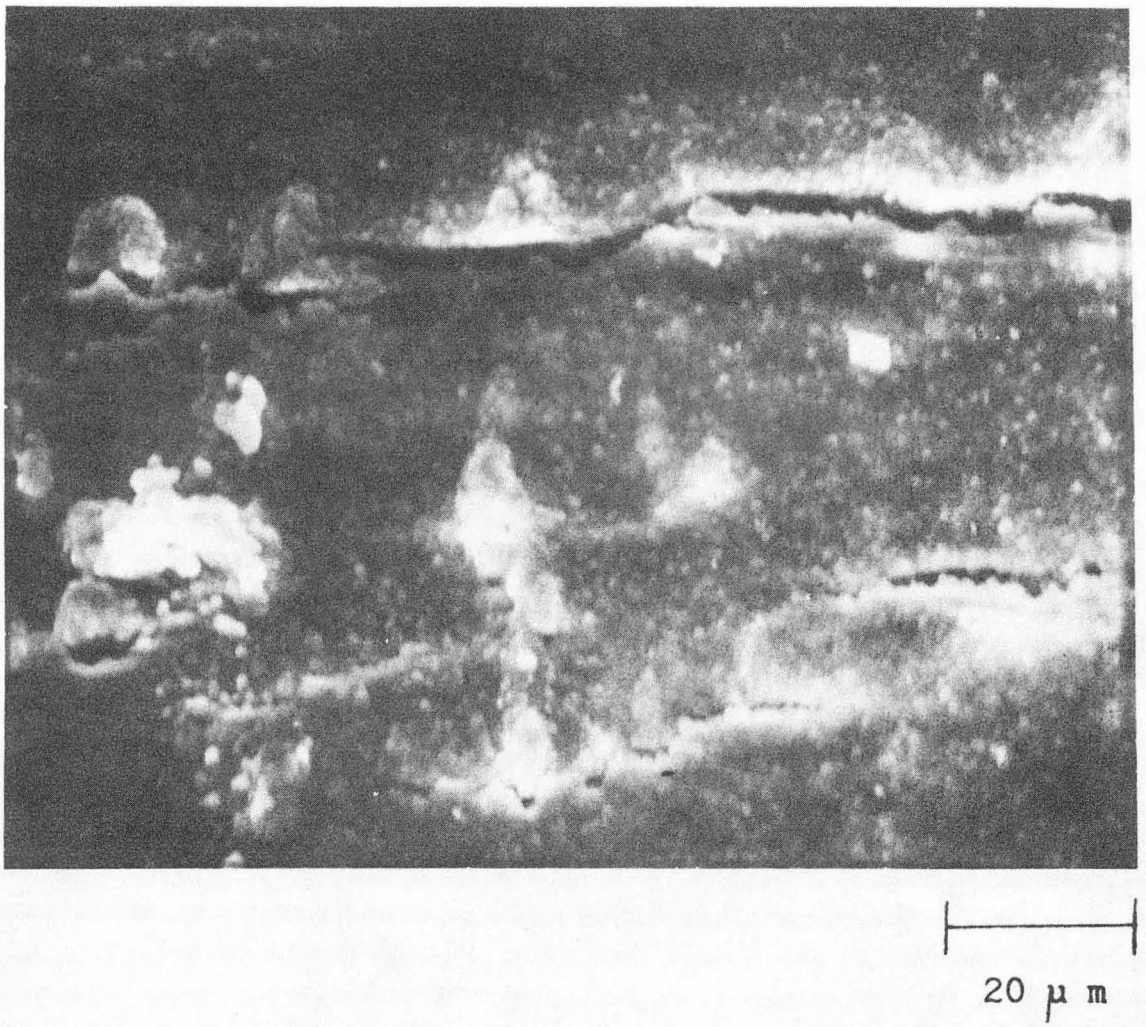

Figure 4-7. SEM of cracked zone of specimen in Fig. 4-6.

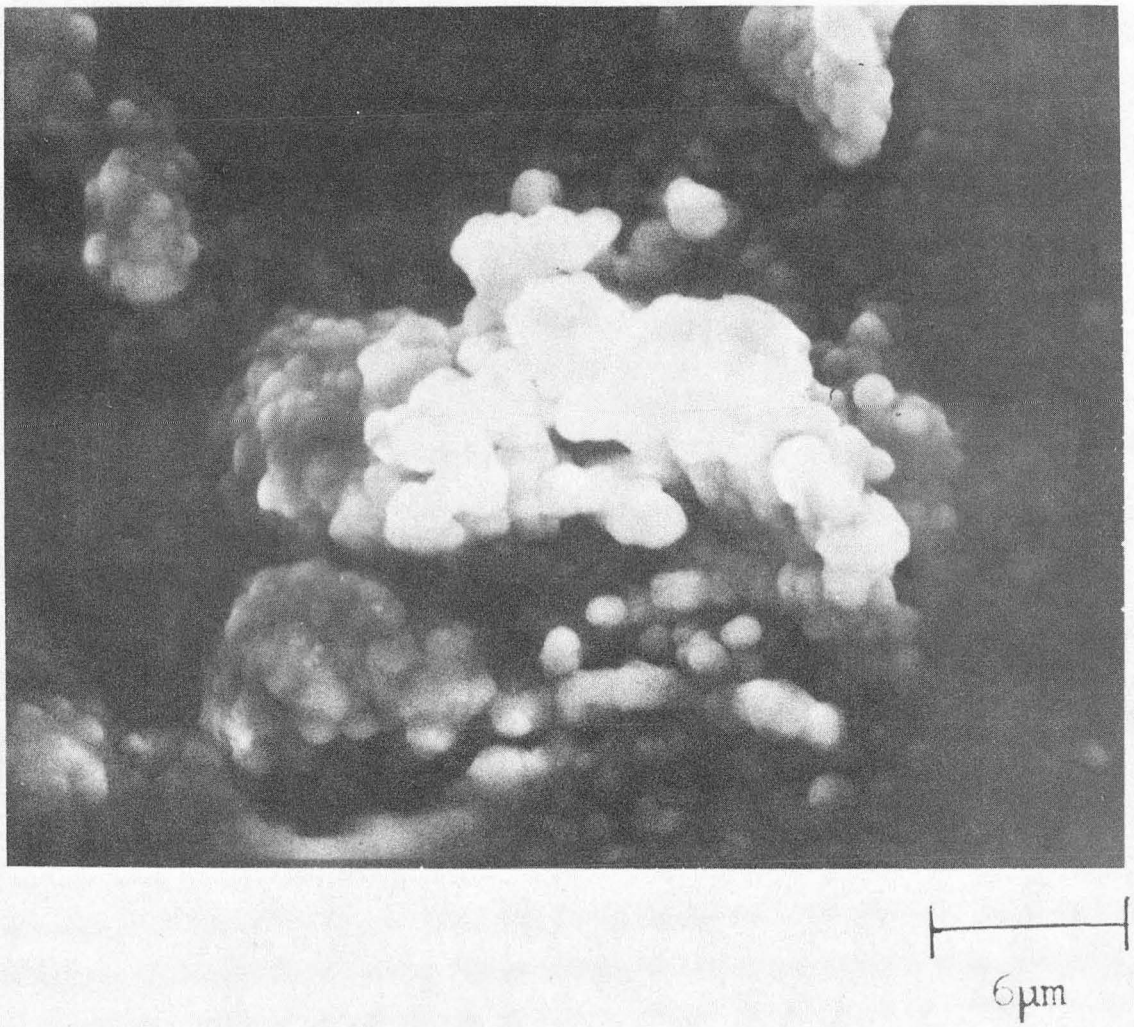

XBB 816-5499

Figure 4-8. Detailed view of the white deposit in Fig. 4-7.

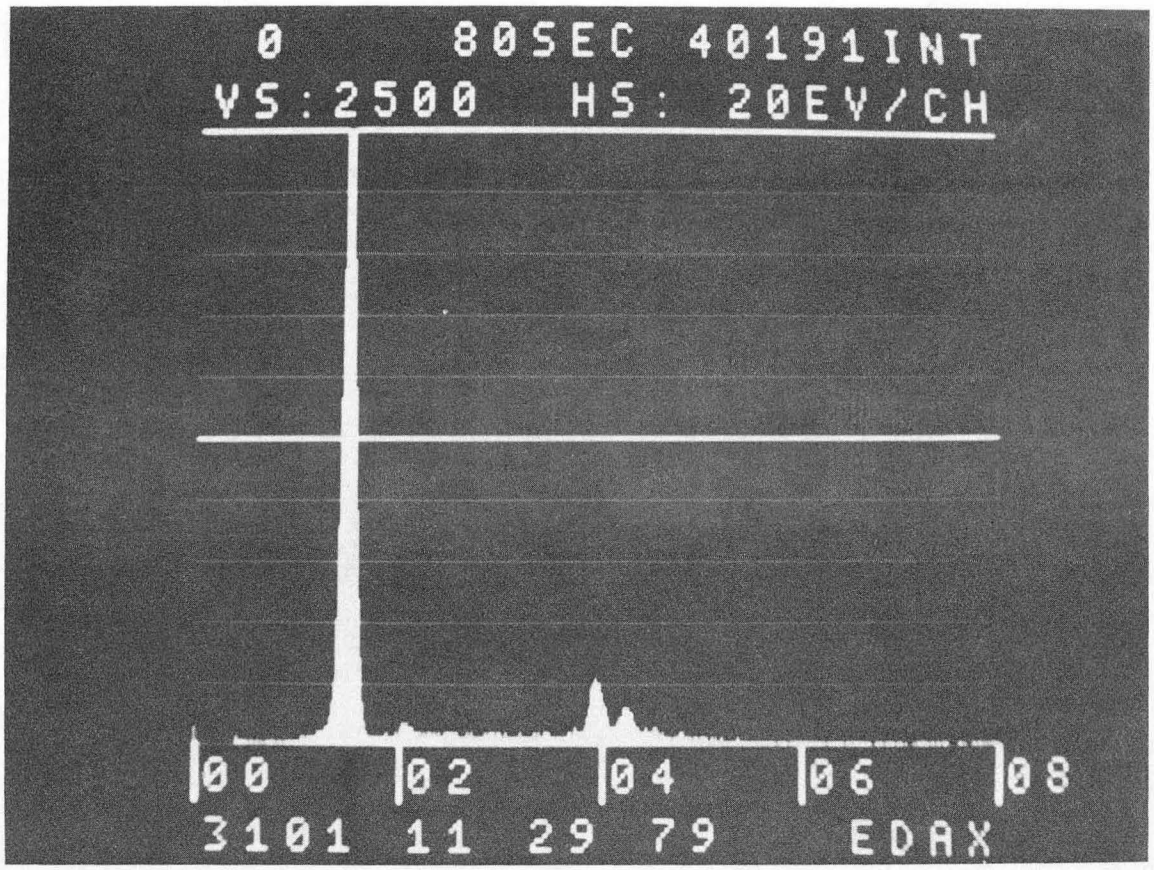

Al Zr I

XBB 806-7326

Figure 4-9. EDAX signals from the white deposit in Fig. 4-8.

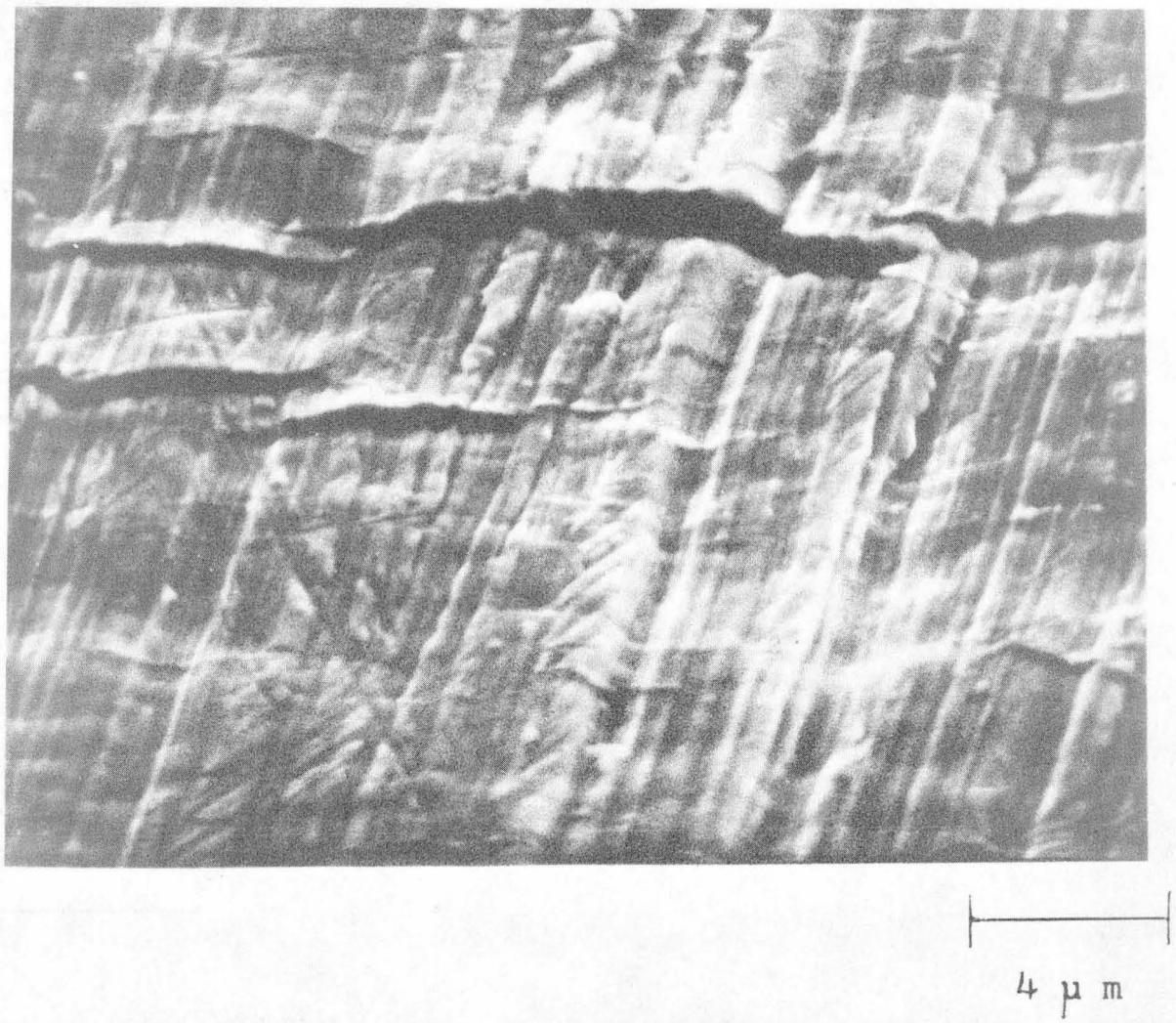

XBB 816-5541

Figure 4-10. SEM picture of unfailed specimen under 365 Mpa, 300°C, and 3.3×10^{-3} torr AlI_3 equivalent pressure for 43 hrs.

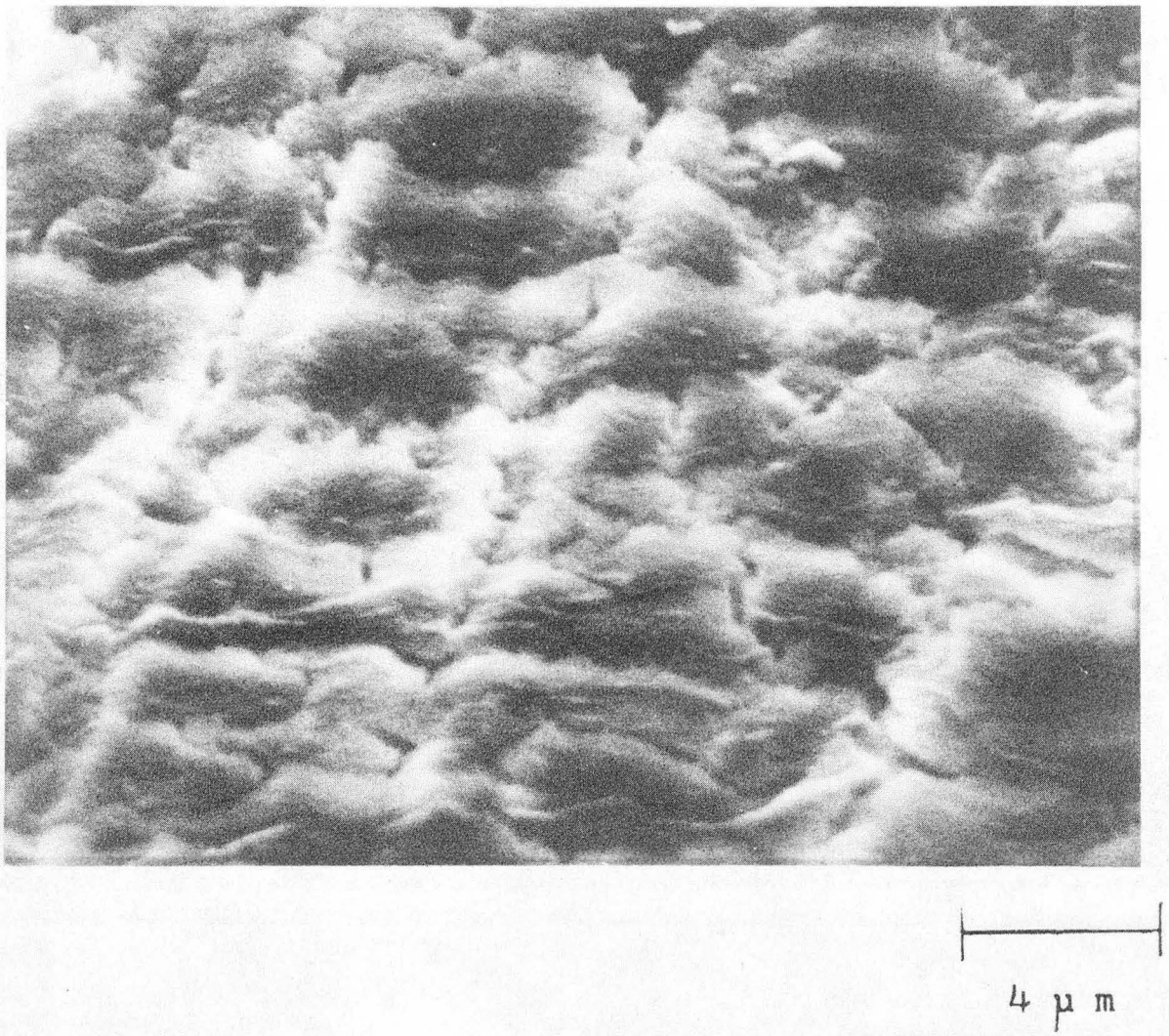

XBB 816-5542

Figure 4-11. SEM picture of unfailed specimen under 365 MPa, 8.0×10^{-5} torr AlI_3 equivalent pressure, and $300^{o}C$ for 43 hrs.

5. IRON IODIDE STRESS CORROSION CRACKING OF ZIRCALOY

5.1 Introduction

Previous experiments showed that iodine can cause stress corrosion cracking of zircaloy at low equivalent pressures (10^{-3} torr) (Section 3.4.2). For the same time-to-failure, aluminum iodide can cause stress corrosion at lower partial pressure than that of iodine (Section 4.4). According to thermodynamics, in a reactor fuel pin most of the iodine should form cesium iodide but there still is a possibility of other iodides at low pressure. This possiblity is the reason for the present iron iodide study.

5.2 Experimental

The present experiment utilizes a tube burst type (biaxial) system as in the iodine (Section 3.2) and aluminum iodide (Section 4.2) tests. Iron iodide crystals are placed in a Knudsen cell and heated to create a molecular beam which impinges on a small spot on the zircaloy tubing. Thermodynamic analysis suggests that $FeI_2(g)$ is the only major species present in vapor phase.

5.3 Materials

As received stress relieved zircaloy-4 tubing (Sandvik Special Metals lot No. JV11) was tested. The chemical composition of zircaloy is listed in Table 5-1. The outside diameter of the tube was 9.5 mm, and the wall thickness was 0.64 mm. Specimens 12.7 cm long were used in the experiment.

5.4 Results

5.4.1 Failure Mode The control specimens without FeI_2 exposure failed by a burst mode. Under iron iodide, specimens stressed higher

than 379 MPa also showed burst-type failure (Fig. 5-1). Lower stresses produced pinhole-type failure (Fig. 5-2). Our experience with iodine stress corrosion led to the same transition stress (Section 3.5.4). Yaggee et al.,[26] in their irradiated zircaloy iodine stress corrosion susceptibility study, and Baty[27] in his zircaloy iodine SCC test also concluded that failure by a burst mode predominates at high stresses, while failure by a pinhole mode predominates at low stresses.

5.4.2 Time to Failure Figure 5-3 gives the results of time-to-failure versus stress at fixed temperature and iron iodide equivalent pressure. This plot shows that the time-to-failure was greatly reduced by 9×10^{-3} torr FeI_2 no matter what the fracture mode.

5.5 Discussion

5.5.1 Fractography The SEM fractography of a pinhole-type failure is shown in Fig. 5-4. and a burst-type failure is shown in Fig. 5-5. Both indicates brittle cleavage, which is also found with iodine and aluminum iodide (Section 3.4.1, 3.5.4, and 4.5.1). Branch cracks at an angle to the main crack seen in Fig. 5-5 are completely different from the surface of the ductile dimple failure mode for control specimens (Fig. 3-9). The shortened lifetime due to the presence of iron iodide and cleavage fracture serve to classify iron iodide as a stress corrosion cracking agent to zircaloy.

5.5.2 Iron Iodide Equivalent Pressure Figure 5-6 shows the time-to-failure versus iron iodide equivalent pressure (P_{eq}) at constant stress and temperature. The line in this figure results from least square fitting of the data points. The slope of $\ln t_f$ vs. $\ln P_{eq}$ is

-0.9 ± 0.1, which is to be compared with slope of -1 for iodine (Section 3.5.5) and $-2/3$ for AlI_3 (Section 4.5.3).

5.5.3 Temperature Dependence Time-to-failure versus temperature at constant stress and equivalent iron iodide pressure results are shown in Fig. 5-7. Least square curve fitting gives the slope of $\ln t_f$ versus $1/T$ which corresponds to an activation energy of 131 Kcal/mole.

5.5.4 Data Correlation The model for crack growth in a brittle solid is applied to present situation. In this model, the crack growth rate is described in chemical reaction terminology by Eq. 3-1.

The crack velocity/stress intensity factor relations given by Eqs. 3-6 and 3-7 were tried. The first one gives the best fit to the stress dependence data. The second one gives $m = 20$.

5.5.5 Crack Initiation Experiment shows failure times for a stress of 375.8 MPa, temperature of 350°C, and 8.6×10^{-3} torr FeI_2 equivalent pressure in the range of 15 to 16.7 hrs (Fig. 5-3. Specimens with this stress, temperature, and FeI_2 pressure were held for 3 and 4.5 hrs then taken out for surface examination. No visible crack initiation was observed. However, SEM showed cracks in both cases (Fig. 5-9). Whether the cracks are present only on the outside surface corrosion film or penetrate into the underlying metal will be discussed in the next chapter (Chapter 6).

Table 5-1. Composition of Sandvik Zr-4(JV11)
INGOT ANALYSIS
COMPOSITION IN PERCENT

	Spec.	TOP	Middle	Bottom
Sn	1.20 - 1.70	1.54	1.51	1.58
Fe	0.18 - 0.24	0.20	0.21	0.23
Cr	0.07 - 0.13	0.11	0.11	0.12
Fe+Cr	0.28 - 0.37	0.30	0.31	0.35
Zr	balance			

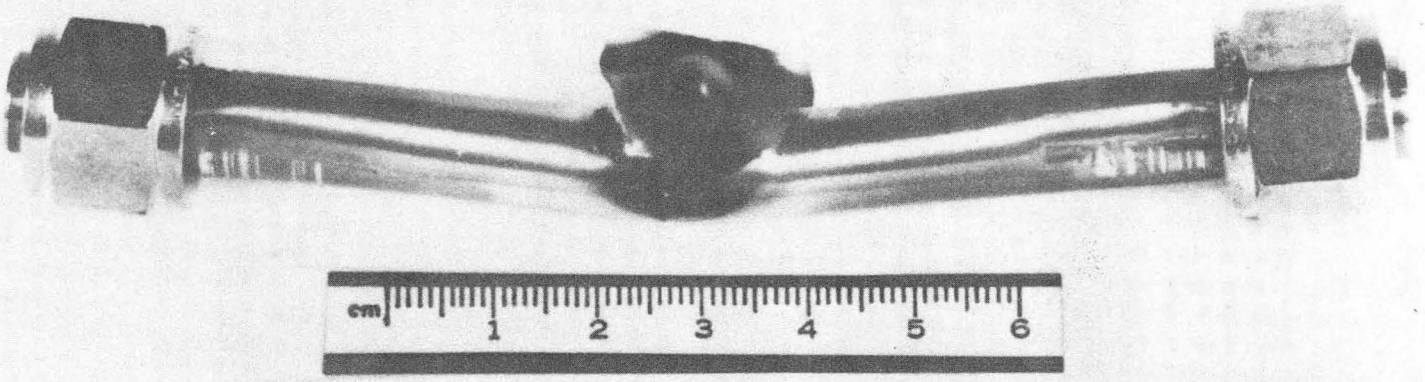

XBB 816-5493

Figure 5-1. Burst type failure for specimen under 379 MPa, 350°C, and 8.6 x 10^{-3} torr iron iodide equivalent pressure after 9.4 hrs.

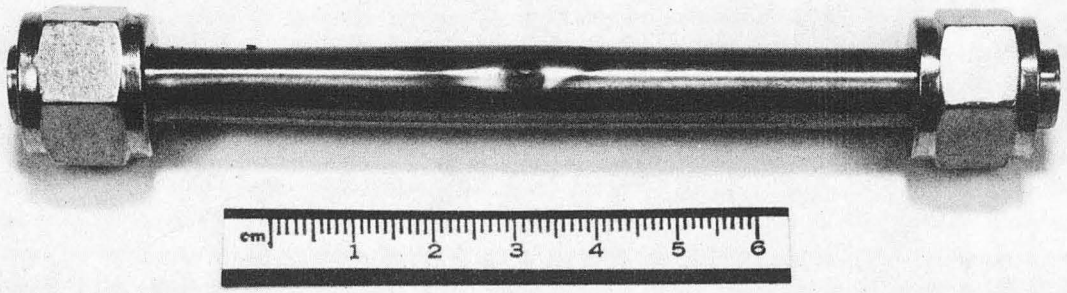

CBB 805-6069

Figure 5-2. Pinhole type failure for specimen under 376 MPa, $360^{o}C$ and 8.6×10^{-3} torr iron iodide equivalent pressure after 3.3 hrs.

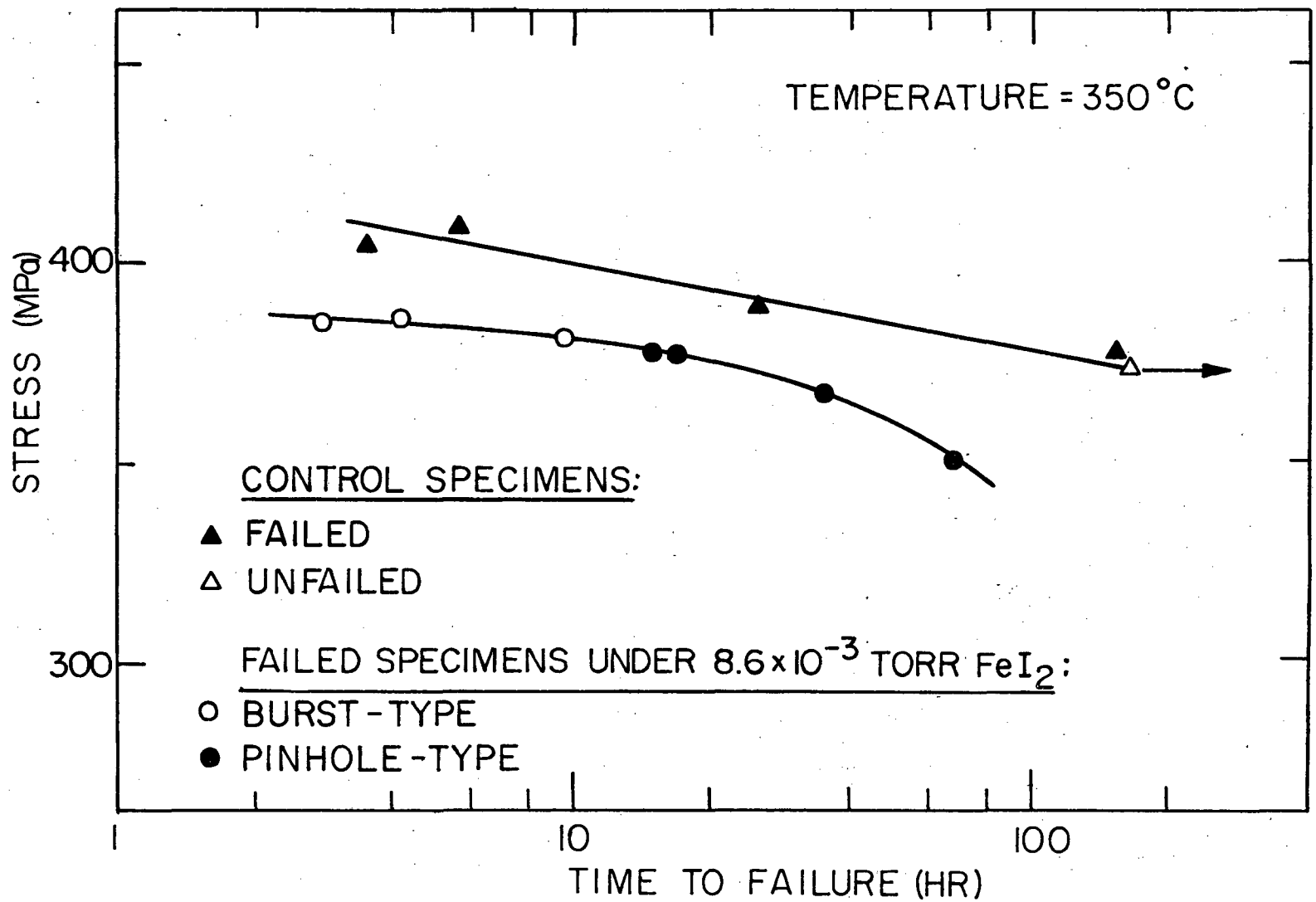

Figure 5-3. Time-to-failue vs. stress for control specimens without corrosive agent and specimens under fixed iron iodide equivalent pressure (8.6×10^{-3} torr) and temperature (350°C)

XBL 8012-13431A

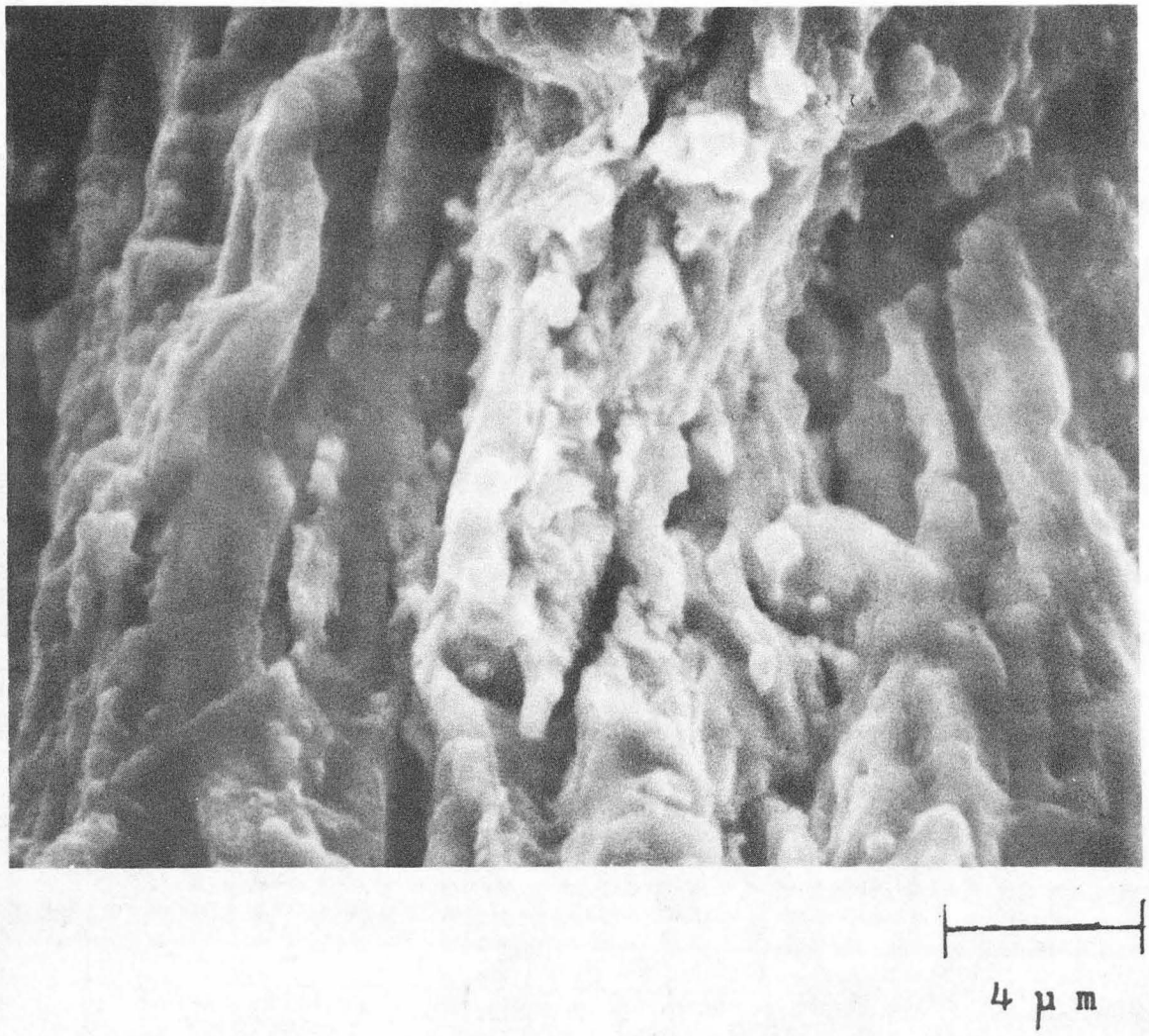

XBB 816-5535

Figure 5-4. SEM fractography of pinhole-failed specimen in Fig. 5-2.

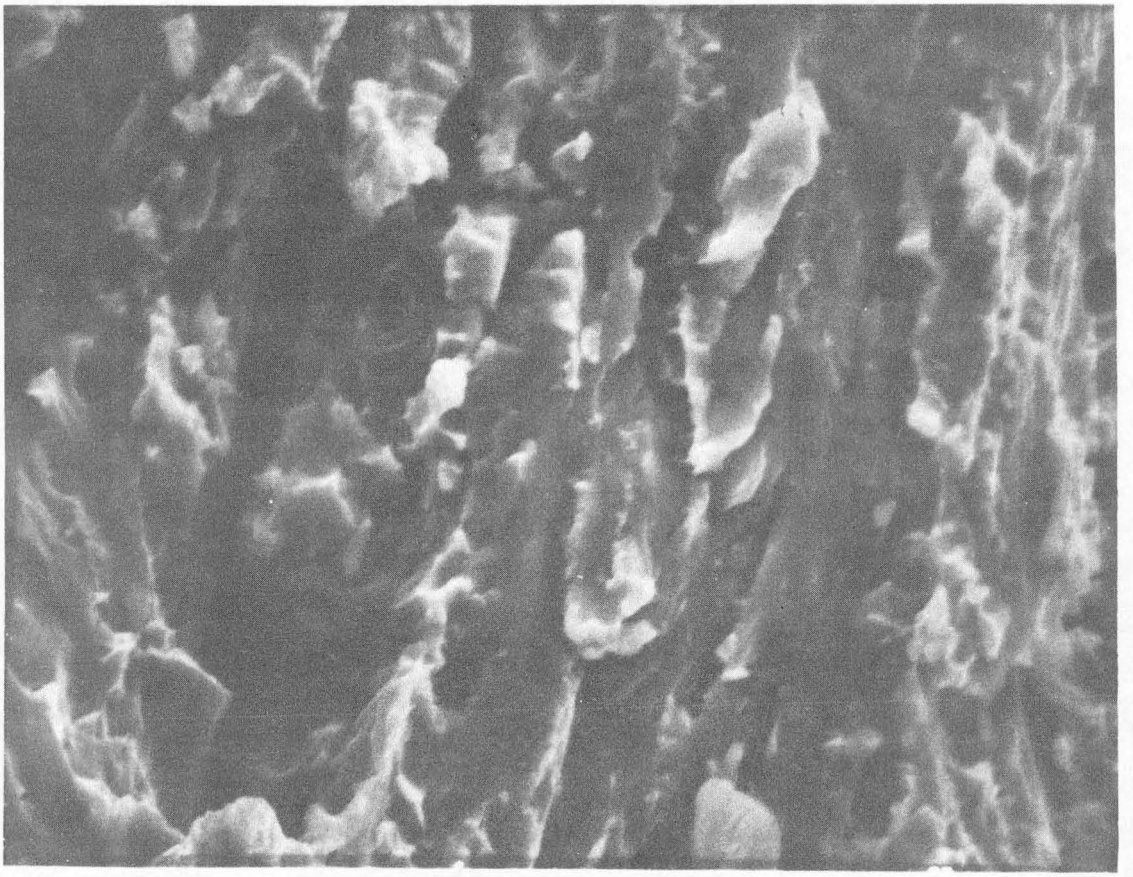

4 μm

XBB 816-5503

Figure 5-5. SEM fractography of burst-failed specimen in Fig. 5-1.

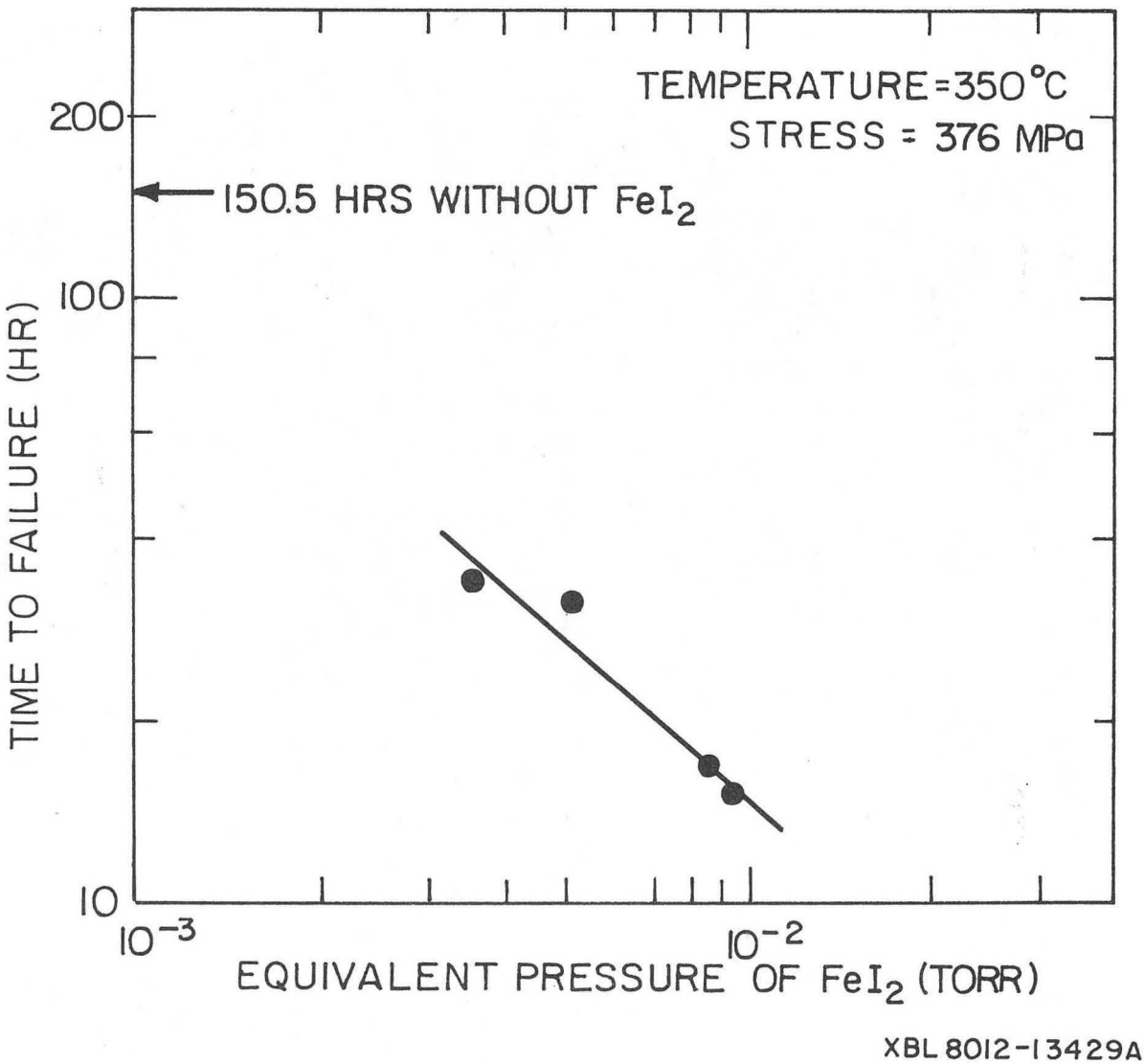

Figure 5-6. Time-to-failure vs. iron iodide equivalent pressure relationship under fixed stress and temperature.

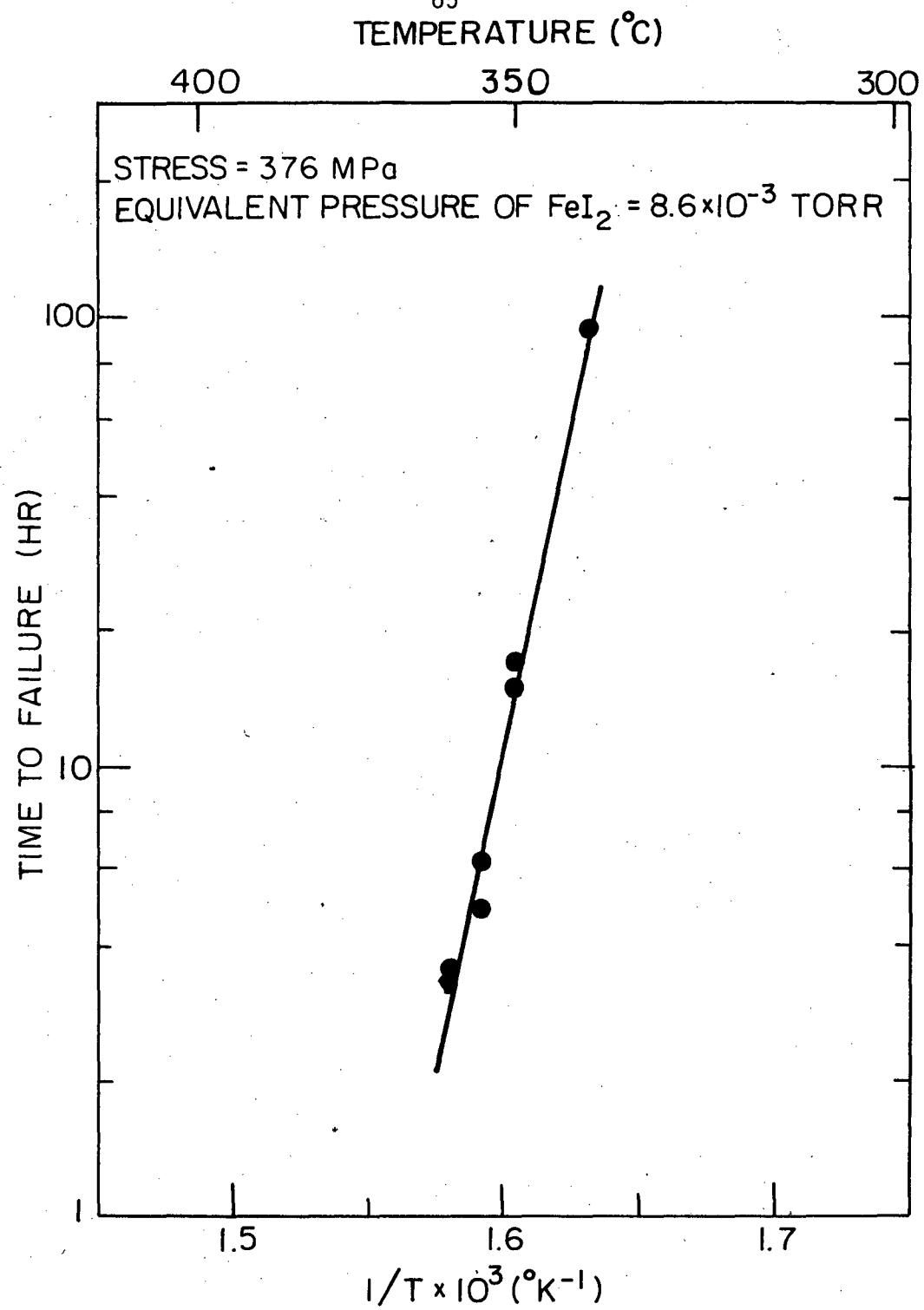

XBL 8012-13428A

Figure 5-7. Time-to-failure vs. temperature relationship under fixed stress and iron iodide equivalent pressure.

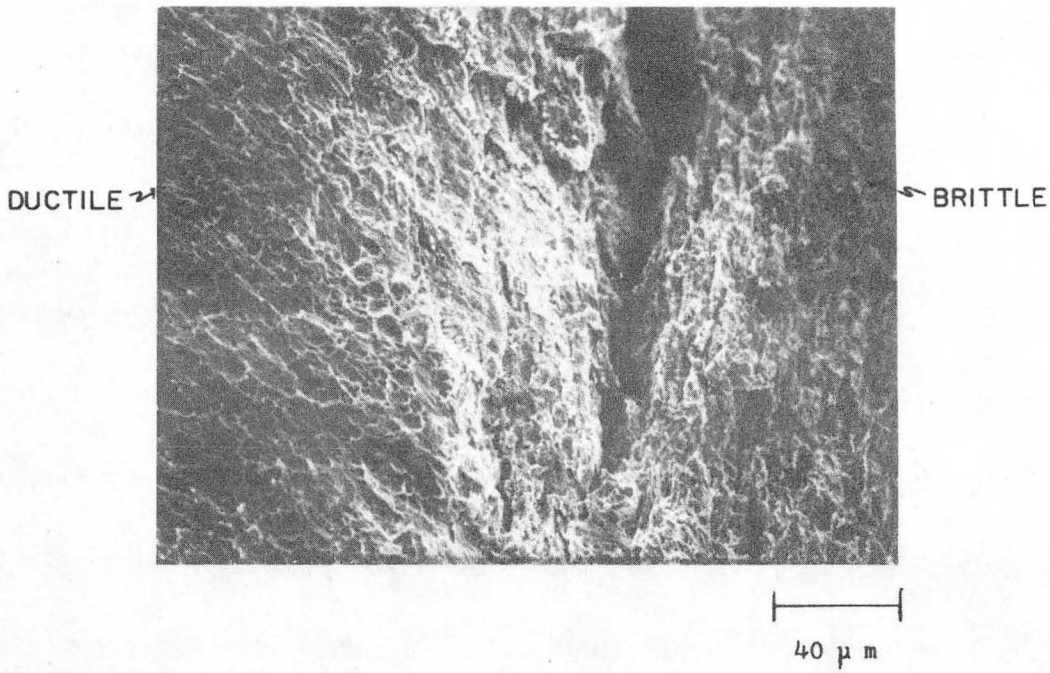

XBB 816-5502A

Figure 5-8. Brittle-to-ductile transition on the fracture surface (Fig. 5-5 specimen).

4 μm

(a) 3 hrs explosure

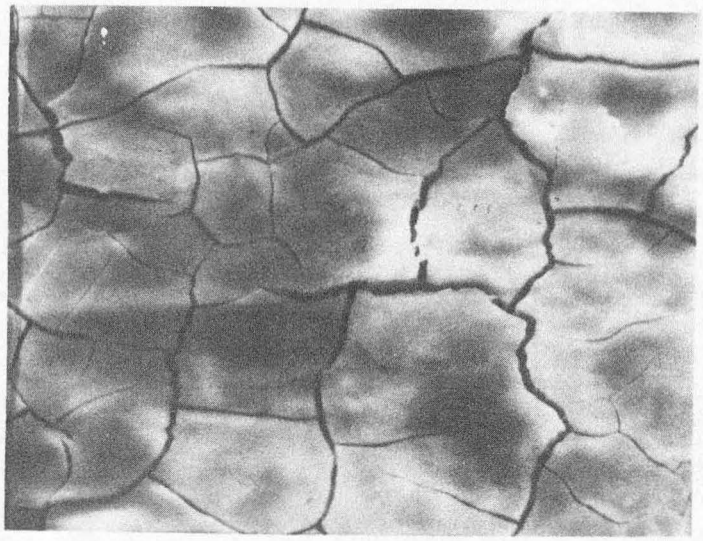

4 μm

(b) 4.5 hrs explosure XBB 816-5512A

Figure 5-9. Iodide-affected surface of specimen under 376 MPa, 350°C, and 8.6 x 10^{-3} torr iodine equivalent pressure; removal before failure.

6. CRACK INITIATION STUDY FOR IRON IODIDE SCC

6.1 Introduction

A specimen was exposed to a molecular beam of iron iodide, stress, and temperature typical of the SCC tests for 20 percent of its failure time, and then removed. Following this test cracks were found on the iodide-affected surface (Section 5.5.5). In order to check whether these cracks were present only on the corrosion film or penetrated into the underlying metal, scanning Auger electron microscope (SAM) and argon ion beam sputtering techniques were used. Since Auger electrons are of low energies, those emitted by atoms deep from the surface cannot escape, so we can study near-monolayer surface chemical compositions by SAM.

6.2 Experimental

The surface Auger electron spectrum of the specimen is shown in Fig. 6-1. Both iron and oxygen signals were detected (FeO), but no zirconium was found. Iodine peaks are not seen, but would lie between the oxygen peaks. Since SAM sensitivity for oxygen is orders of magnitude higher than that of iodine,[31] we cannot draw any conclusions concerning the presence of iodine. Then argon sputtering was started on the region shown in Fig. 6-2. After 30 minutes of sputtering, or removal of 0.5 μm (a rough estimate from the rate of 0.04 μm/min on Ta_2O_5 calibration specimen[31,32]). Sputtering was terminated when the surface Auger electron spectrum showed only zirconium. The final spectrum is shown in Fig. 6-3. Since the metal surface was exposed, we can check if cracks penetrated into the metal. The specimen was examined with SEM for better resolution.

6.3 Results and Discussion

6.3.1 Crack Propagation Dominates the Specimen Lifetime After examination, we find that cracks penetrated into the underlying metal. We conclude that the initiation period for iron iodide stress corrosion cracking is less than 20 percent of its lifetime. Crack propagation is the time consuming step in the SCC process.

6.3.2 Crack Initation Sites Figure 6-4 is a picture of sputtered region under SEM and EDAX. It is the same spot depicted in Fig. 6-2. Figures 6-5 through 6-9 are regions with high incipient crack densities. Their EDAX spectra show abnormally high tin and iron concentrations by comparison with the larger area covered in Fig. 6-4. Figure 6-10 is a region of low crack density, with normal tin and iron concentrations. Different chemical composition can change the hardness of metal, and so affect the sputtering rate;[13] the features in Fig. 6-5 to 6-9 may be artifacts caused by different sputtering rates. Nonetheless, regions with higher concentrations of alloying elements (tin or iron) appear to act as sites for crack initiation. Jones et al. arrived at the same conclusion in their indenter crack initiation study.[13]

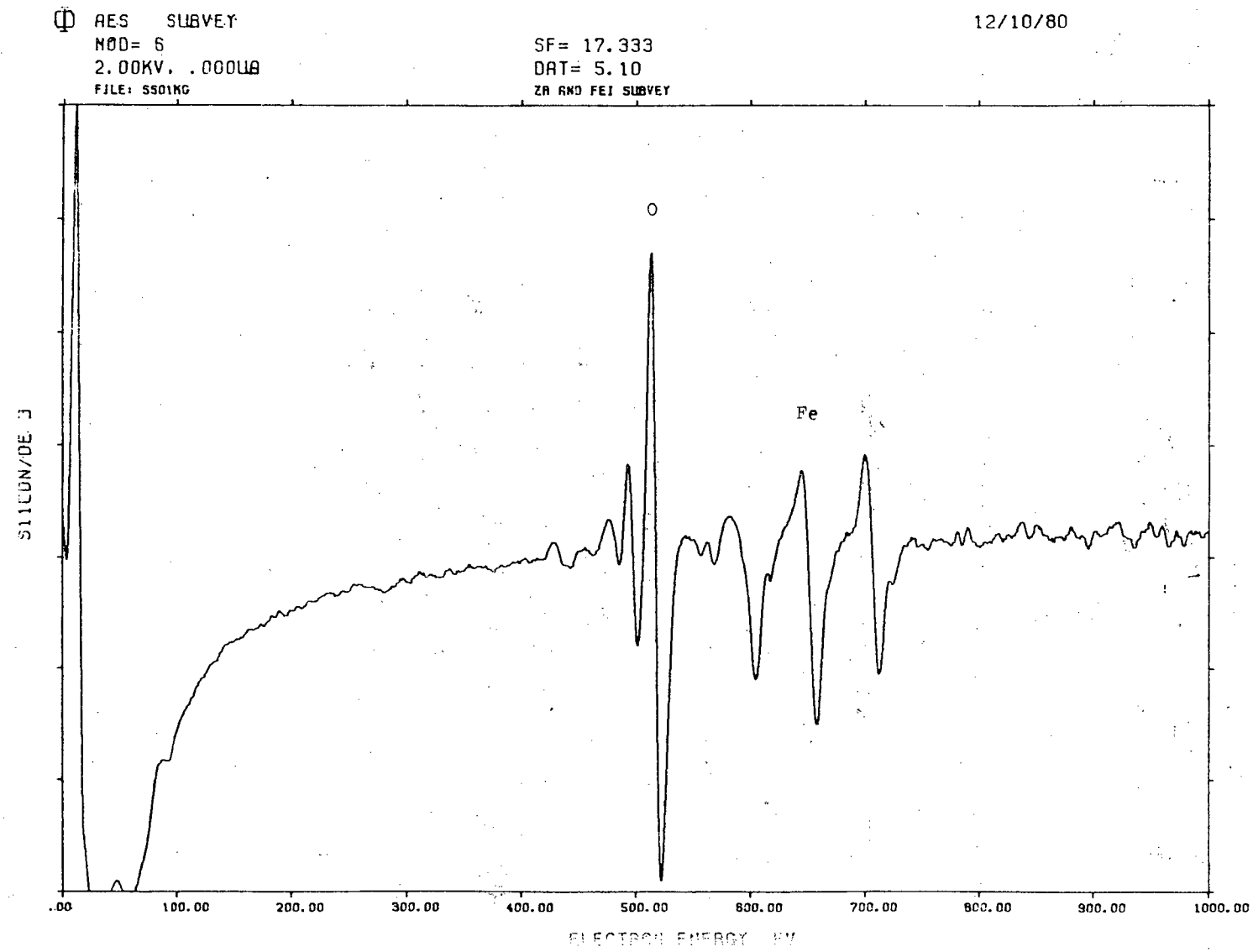

Figure 6-1. Auger electron spectrum of the specimen (under iron iodide for 20% of its lifetime) before argon sputtering (Surface shown in Fig. 5-9b) XBL 816-10394

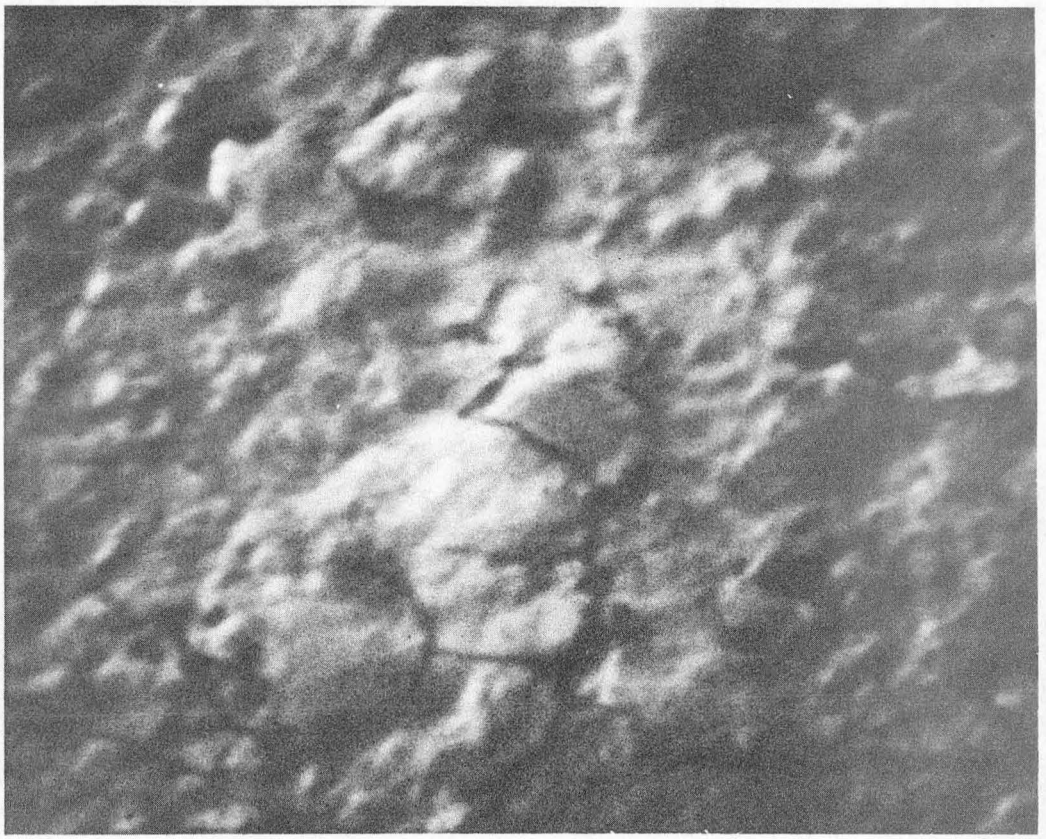

40 μ m

XBB 816-5515

Figure 6-2. The sputtered region under SAM after 30 min.

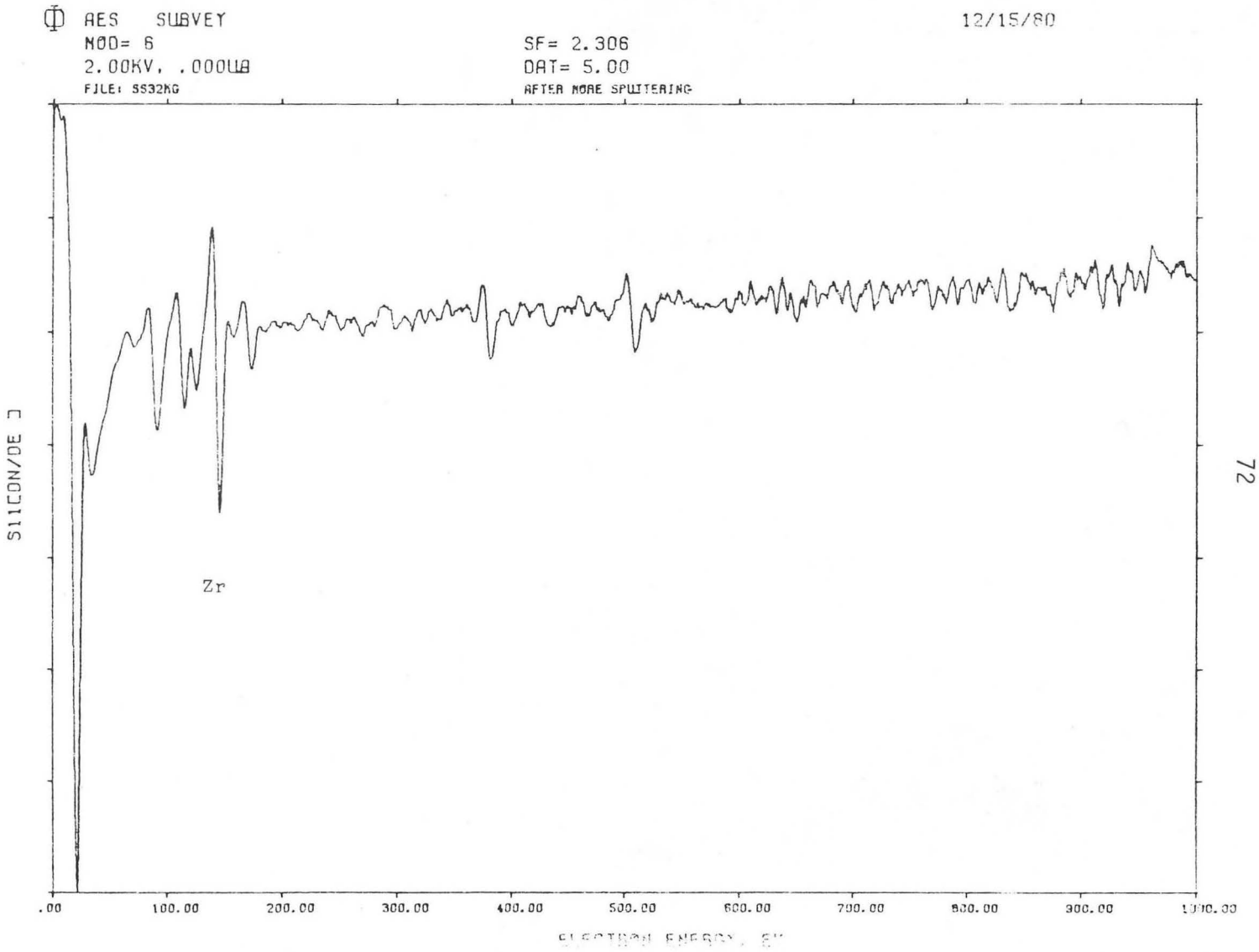

XBL 816-10395

Figure 6-3. Auger Electron Spectrum for the Specimen after removal of 0.5 μm).

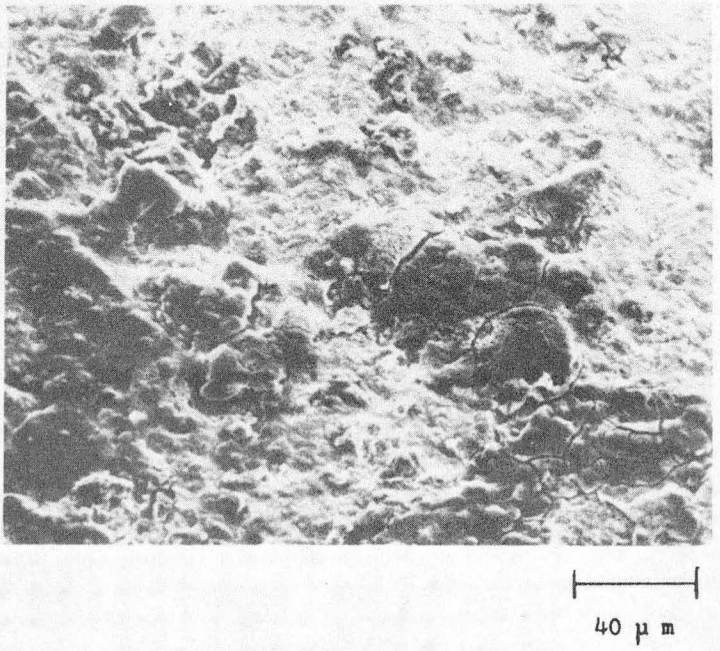

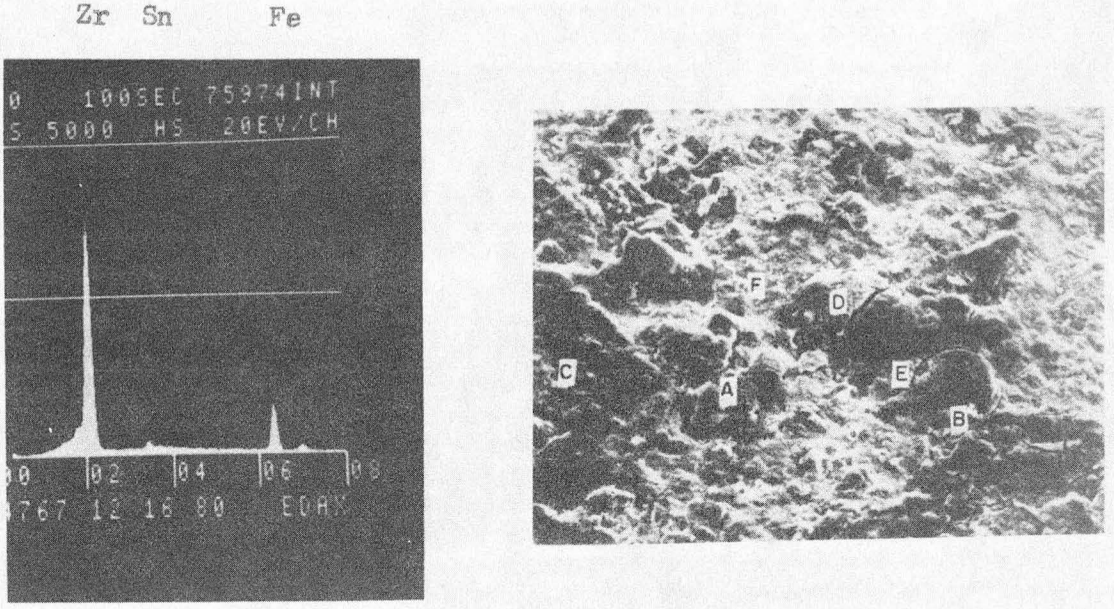

XBB 816-5514B

Figure 6-4. Argon sputtered region under SEM.

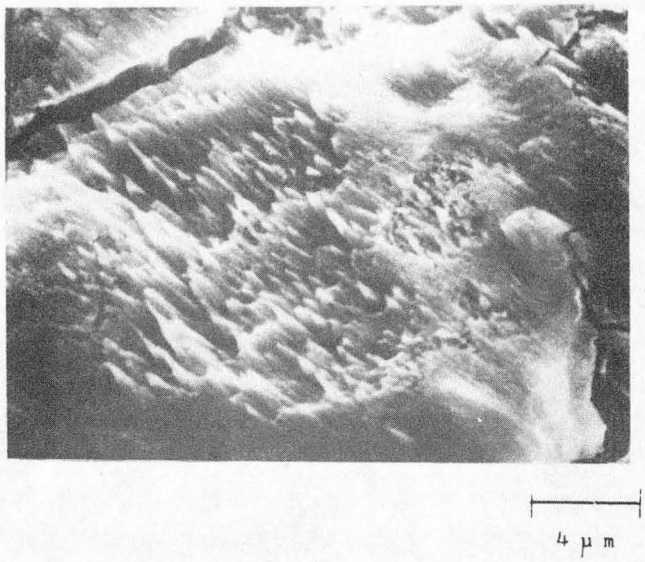

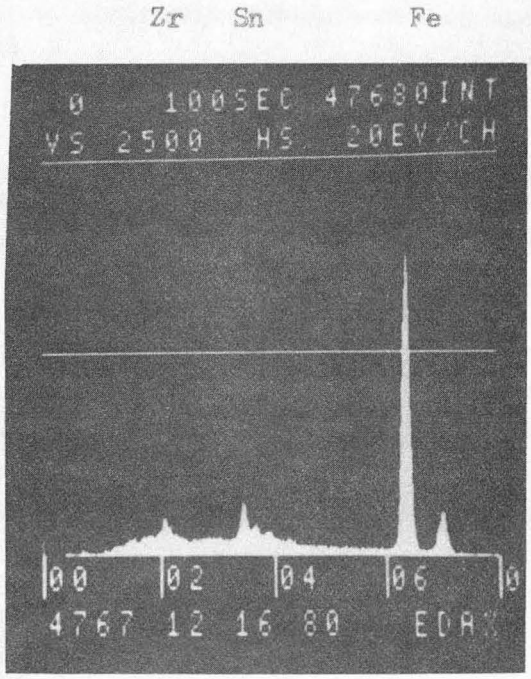

XBB 816-5540A

Figure 6-5. Region A (with high crack initiation probability).

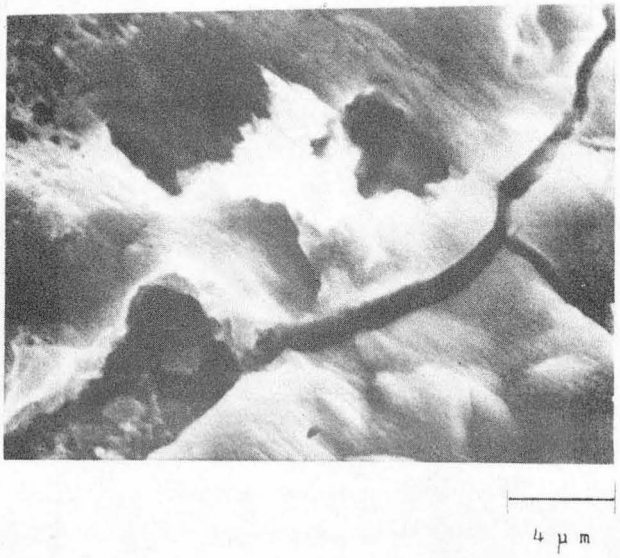

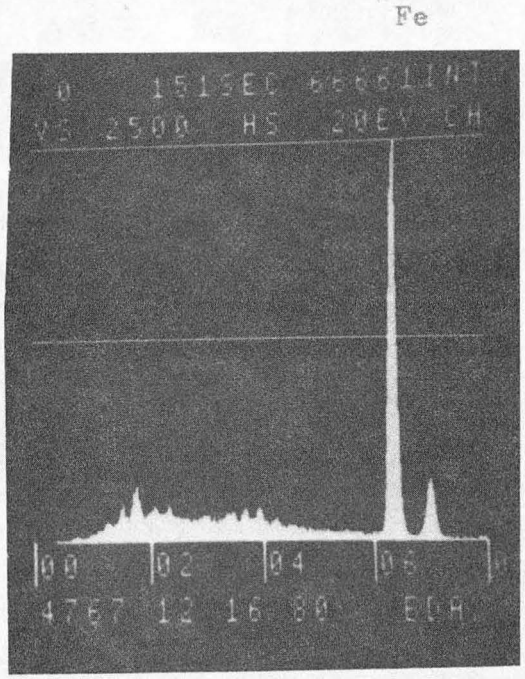

XBB 816-5539A

Figure 6-6. Region B (with high crack initiation probability).

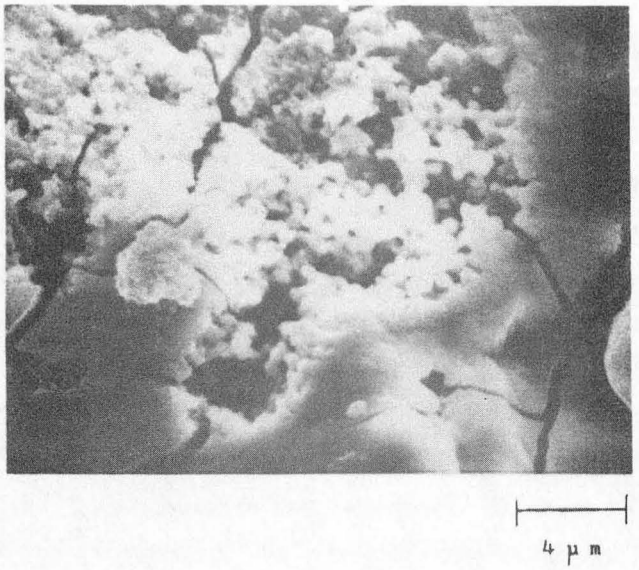

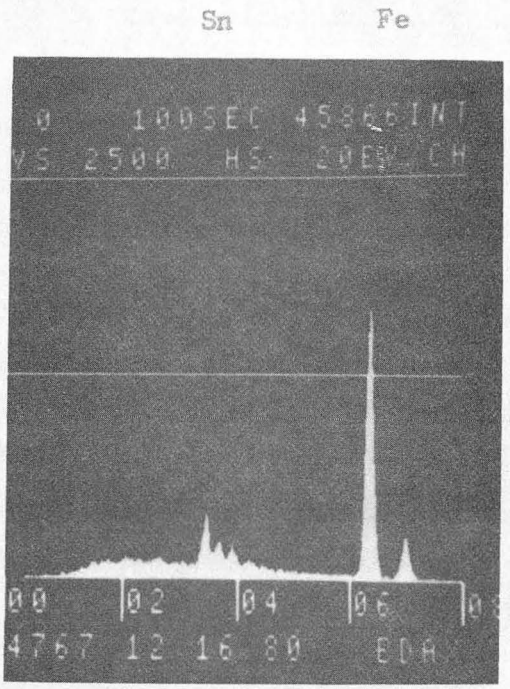

XBB 816-5527A

Figure 6-7. Region C (with high crack initiation probability).

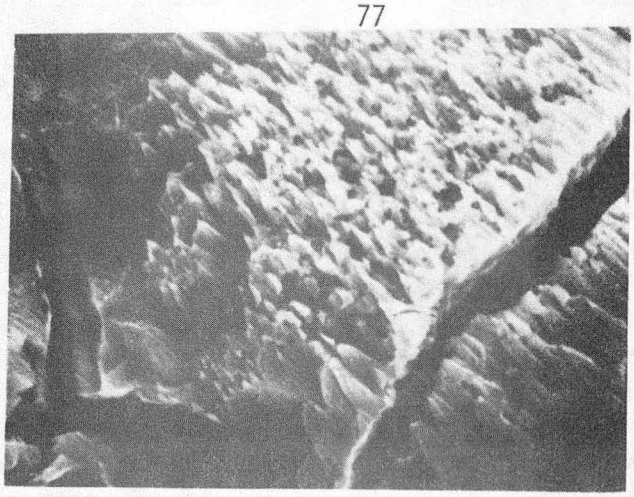

4 μm

Fe

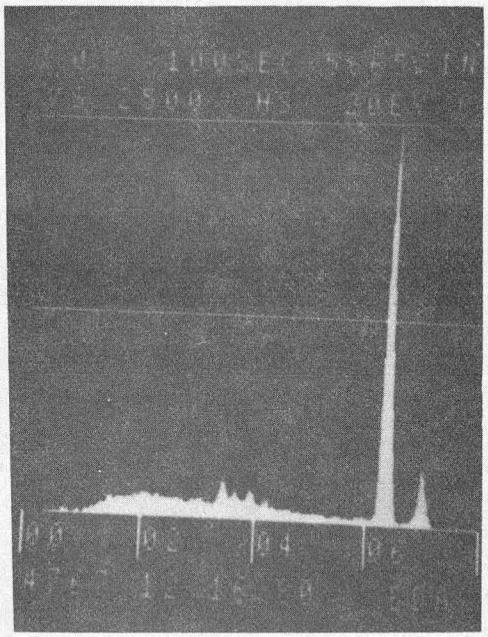

XBB 816-5528A

Figure 6-8. Region D (with high crack initiation probability).

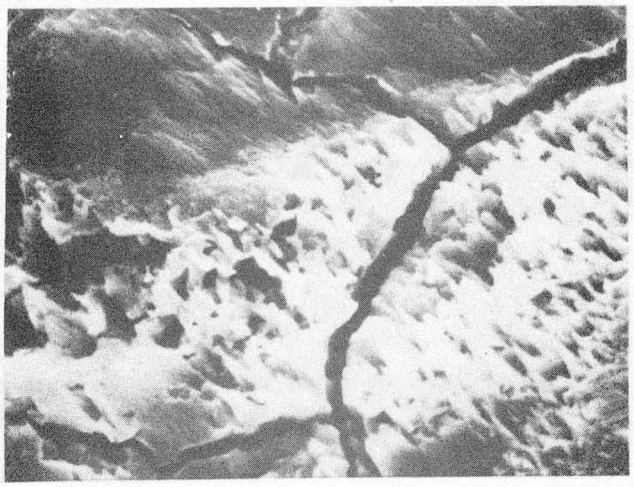

Fe

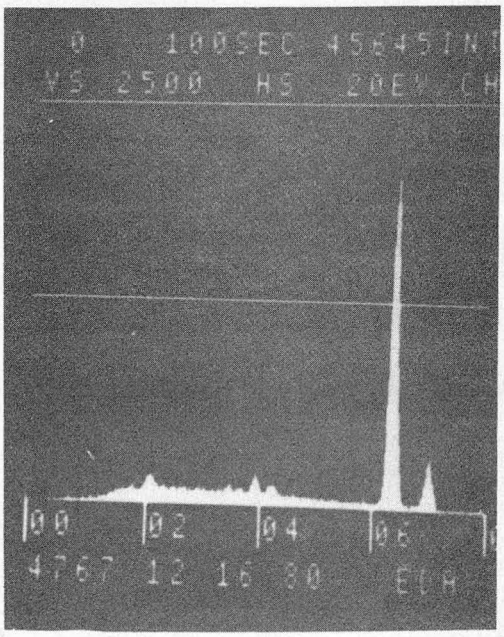

XBB 816-5513A

Figure 6-9. Region E (with high crack initiation probability).

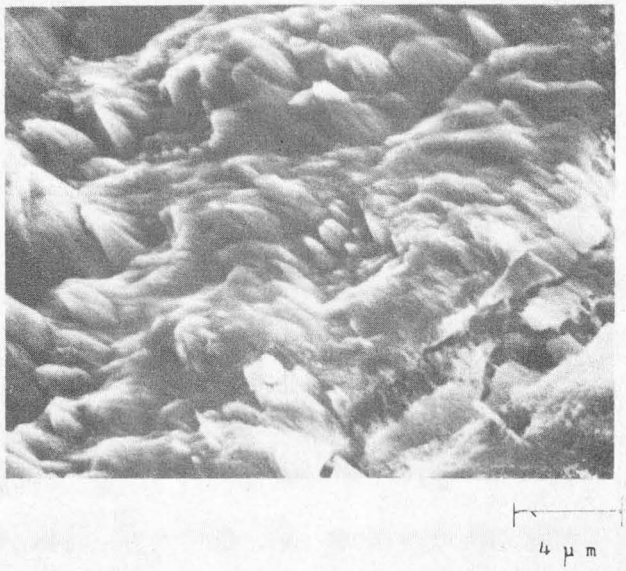

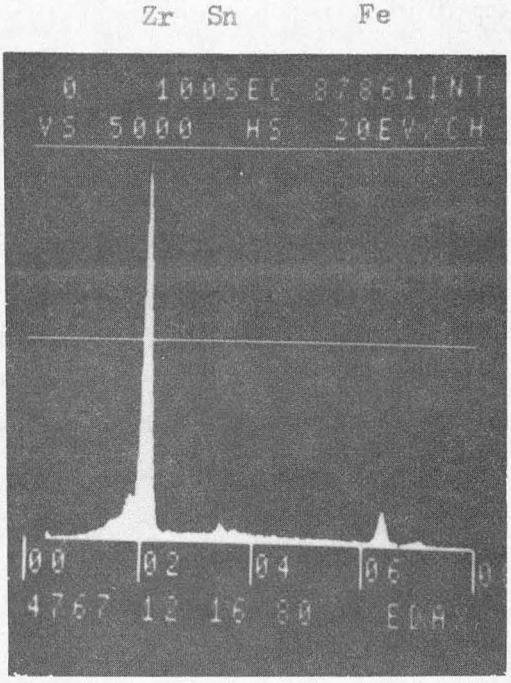

XBB 816-5511A

Figure 6-10. Region F (with low crack initiation probability).

7. CADMIUM VAPOR EMBRITTLEMENT OF ZIRCALOY

7.1 Introduction

Cadmium is a fission product which thermodynamics suggests should exit inside a fuel pin in the metallic state.[19,33] Based on specimens exposed to liquid cadmium or contacting a solid cadmium film (produced by vacuum evaporation), cadmium severely embrittles zircaloy.[13,19,33] In an inpile situation, the probability that the cladding is in contact with metallic (solid or liquid) cadmium is much smaller than exposure to cadmium vapor. This points the need for a study of zircaloy-cadmium vapor behavior under stress.

7.2 Experimental

The present experiment utilized a tube-burst type (biaxial) test mode. The same apparatus for creating the stress as the one used in iodine, aluminum iodide, and iron iodide studies was employed. Cadmium solid was placed in a Knudsen cell and heated to create a molecular beam impinging on the zircaloy surface. The rate at which cadmium atoms strike the zircaloy surface (moles/sec cm^2) can be transformed to equivalent pressure (torr) by the method outlined in Section 2.4.

7.3 Materials

As received stress-relieved zircaloy-4 (Sandvik Special Metals lot number JV 11) was used in this study. The same lot of zircaloy-4 was tested in iron iodide stress corrosion cracking. Detailed chemical composition and dimensions are listed in Table 5.1.

7.4 Results

7.4.1 Failure Mode Every tube tested under cadmium showed burst-type failure (Fig. 7-1) even when the rupture time was less than

that of the control specimens. The pinhole mode characteristics of iodine, aluminum iodide and iron iodide did not appear in the case of cadmium. Recently, Wood et al.[34] have shown that the strain at failure in an iodine environment is much smaller than in cadmium, which can explain the difference in fracture mode. Pinhole failure occurs with low failure strain (less than several percent) in iodine and iodides, while cadmium fracture occurs at high strain.

7.4.2 Time-to-Failure Figure 7-2 gives the time-to-failure versus stress relationship for cadmium-affected specimens. The presence of cadmium vapor decreased the zircaloy lifetime. As an example, at 376 MPa, we can compare the 151 hr lifetime for controls specimen with the less than 16 hr lifetime of samples under cadmium.

7.5 Discussion

7.5.1 Scatter of Data The tubes of lot JV 11 came in 1 m lengths. The specimens we used were 12.7 cm long, so seven could be cut from each tube. Figure 7-2 shows some scatter in experimental results for specimens from different tubes. Fortunately, in Figure 7-2, 7-3, and 7-4, systematic results can be obtained by dealing with specimens from the same tube. The scattering phenomenon only exits between tubes but not for samples taken from the same tube. The reason for the scatter between tubes is still unknown. The following gives two possibilities:

(A) Comparison of Figs. 3-16 and 5-3 with Fig. 7-2 shows that the t_f versus stress curves are much flatter for Cd than for I_2 or FeI_2. Since the slope of the time-to-failure versus

stress plot is near zero, a small change in stress could cause a large change in the time-to-failure. The uncertainty in stress may come from small differences in wall thickness.

(B) Some factors affecting the cadmium-zircaloy interaction change from tube to tube. In iodine and metal iodide SCC, failure always occurred at the center of iodide-affected region where the beam impingement rate is the highest, while in the cadmium case, the failure occurred randomly inside the cadmium-affected region. There may be some unknown surface factor, or surface inhomogeneity, controlling the process.

7.5.2 Fractography The SEM fractography shown in Figs. 7-5 and 7-6 reveals many reaction products (i.e., alloys) on the fracture surface. The white deposits show higher cadmium-to-zirconium ratios (corresponding to ZrCd or Zr_2Cd) than that of the average surface (< 5 percent Cd). Some of them even show peaks of iron besides zirconium and cadmium. Beneath the reaction products, we still can see that the fracture surface is of cleavage type with considerable branching from the main crack (Fig. 7-5 and 7-6).

Because of the brittle fracture mode (on a microscopic level) and shortened lifetimes, we can conclude that the cadmium vapor has an influence on zircaloy mechanical behavior.

7.5.3 Data Correlation The brittle solid crack propagation model (Eq. 3-3) used for iodine and iron iodide is applied to the cadmium results. Because the results for t_f versus stress scatter appreciably between tubes, good fitting values of the parameters could not be

derived. However, the stress exponent in Eq. 3-7 appears to be ~20. In Fig. 7-4, we utilize specimens for time-to-failure versus temperature experiments which are all from one tube. The same is true for t_f versus equivalent pressure tests (Fig. 7-3). The equivalent pressure and temperature dependence relations will be discussed in the next two sections.

7.5.4 Cadmium Equivalent Pressure The relationship of time-to-failure and equivalent pressure of cadmium is shown in Fig. 7-3. Least squares fitting of those data gives:

$$t_f \propto (P_{eq})^{-1.0 \pm 0.2} \tag{7.3}$$

7.5.5 Temperature Window In Fig. 7-4, we find that the specimens tested at 8.3×10^{-3} torr cadmium vapor and 330°C did not fail for 300 hrs, thereby departing from the general trend of the curve. According to Old,[35] there is a temperature window for liquid metal embrittlement; the strain of failed specimens is reduced only in a small temperature range. Outside of this temperature window, there is no significant reduction in failure strain in comparison to that of the control specimens. We conducted additional experiments in order to examine the phenomenon with gaseous metal embrittlement.

Figure 7-7 shows the experimental results. For 8.3×10^{-3} torr Cd, we find reductions of failure time for temperatures between 380°C and 335°C. In this range the plot of ln t_f versus 1/T gives an activation energy $E^* = 54 \pm 2$ Kcal/mole. Specimens tested at 385°C and

395°C fall in the scatter band of the control specimen curve. Both of them showed ductile dimple fractography (Fig. 7-8). Specimens tested at 330°C did not fail for 200 and 300 hrs. The 8.3×10^{-3} torr curve in Fig. 7-7 showed a bend of the failure-time versus temperature curve at 330°C. We conclude that a temperature window exists between 335°C and 380°C for 8.3×10^{-3} torr cadmium vapor. Likewise, there is temperature window, 370°C to 325°C, for 4×10^{-3} Cd equivalent pressure, and 385°C to 315°C for 16×10^{-3} torr Cd equivalent pressure. The specimen tested under 2×10^{-3} torr did not show reduction of lifetime, and exhibited ductile dimple fractography at test temperature (Fig. 7-9). We conclude that 2×10^{-3} torr is below the threshold pressure for Cd SCC.

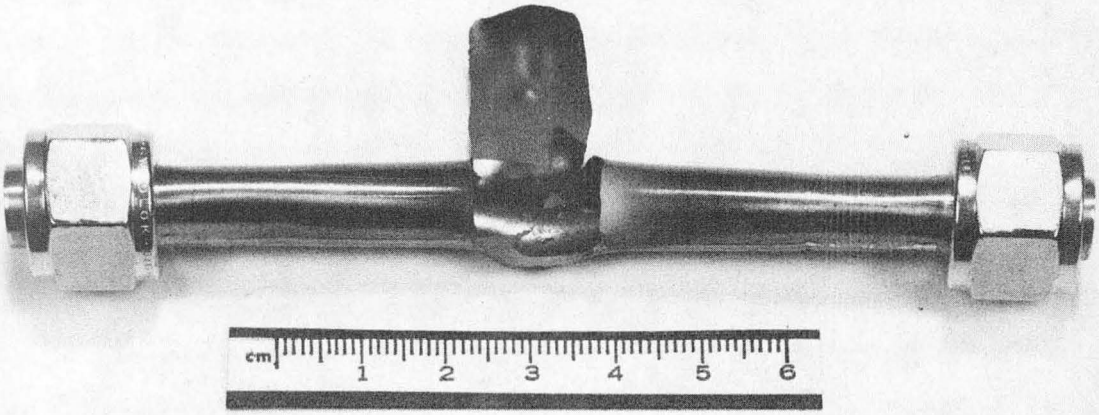

CBB 805-6067

Figure 7-1. Burst type failure for specimen under 388 MPa, 350°C, and 8.3×10^{-3} torr cadmium equivalent pressure after 2.8 hrs.

Figure 7-2. Time-to-failure vs. stress relationship for control specimens without corrosive agent and specimens under fixed cadmium pressure (8.3×10^{-3} torr) and temperature ($350^{o}C$).

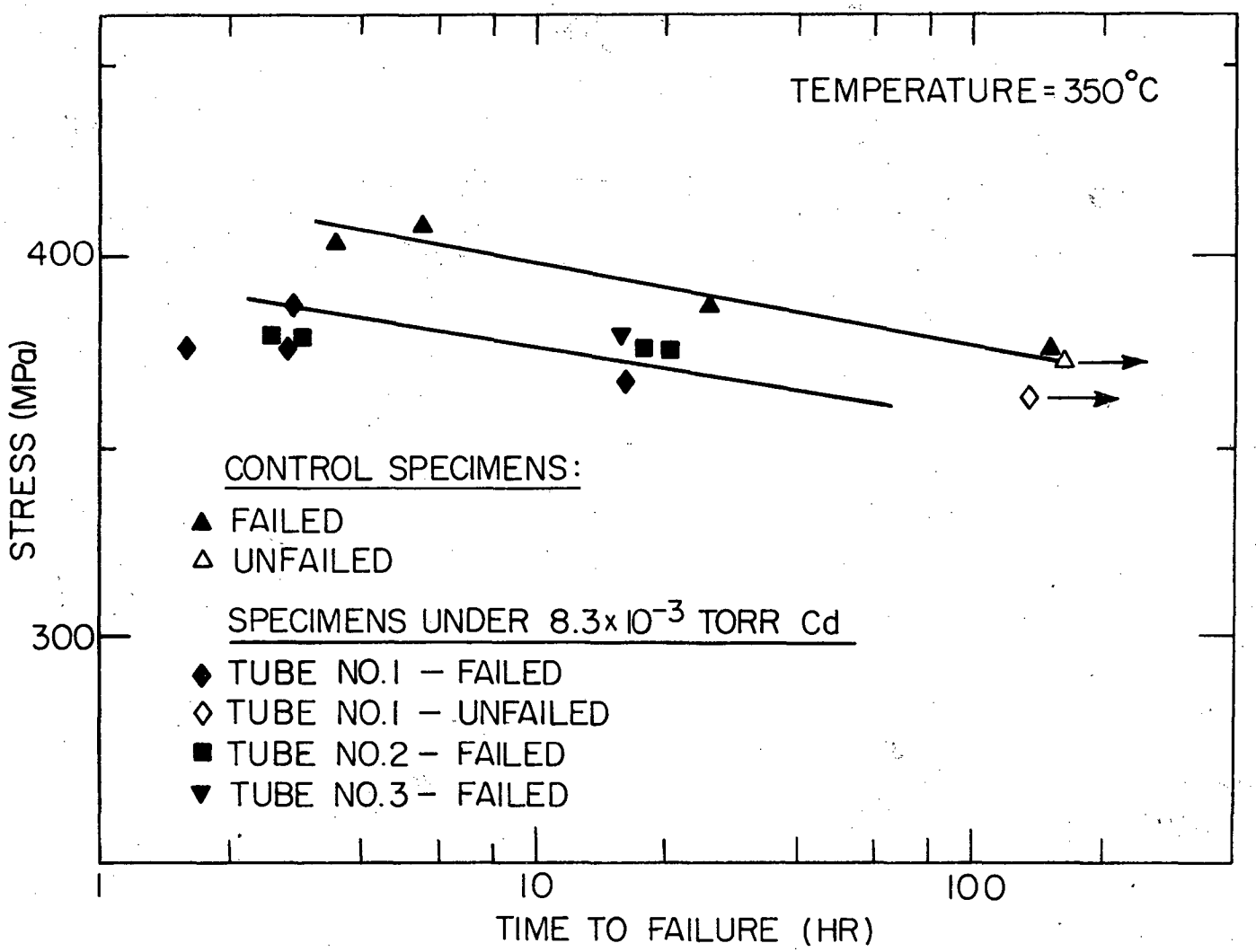

XBL 8012-13430A

Figure 7-2.

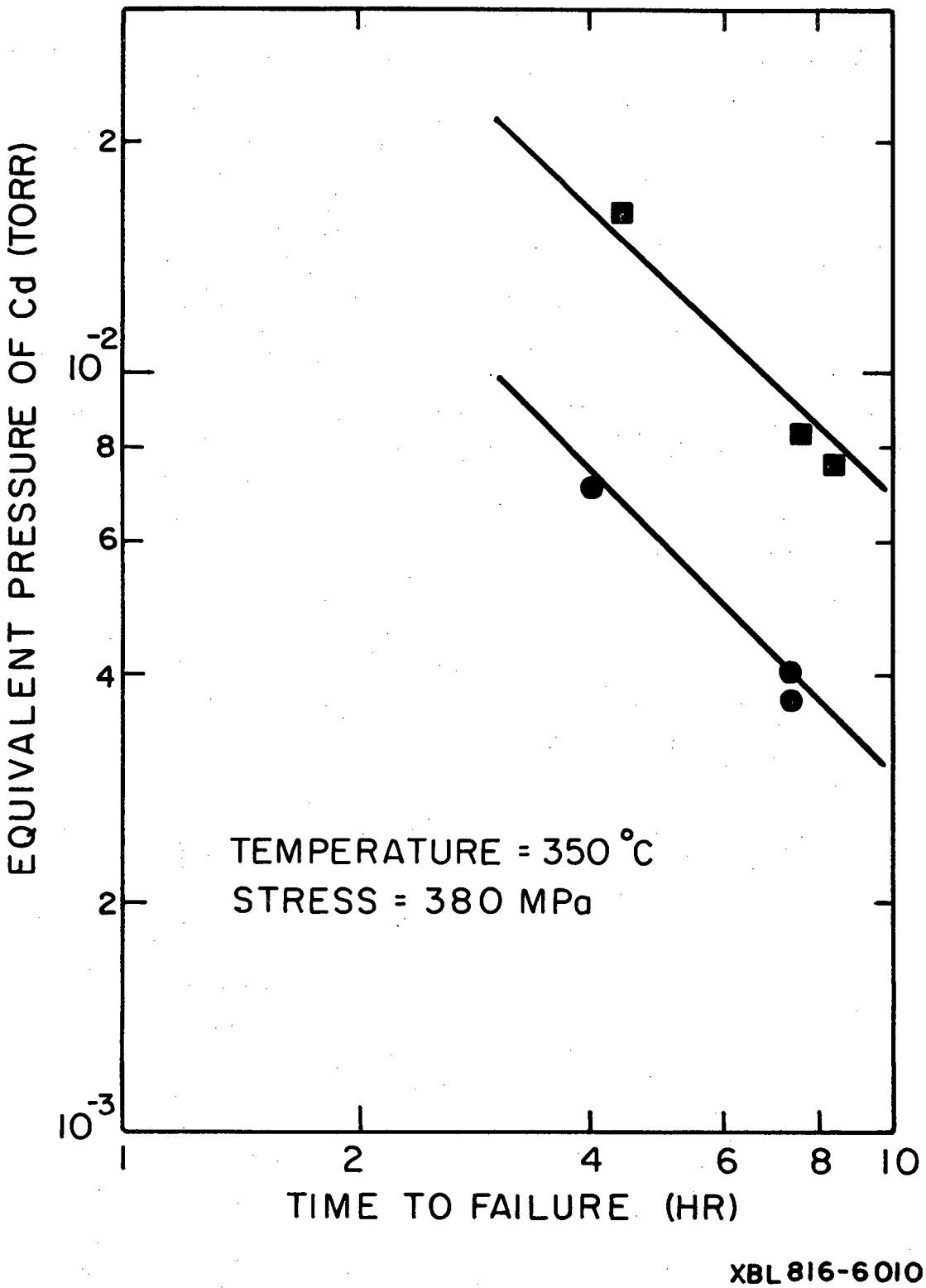

Figure 7-3. Time-to-failure vs. cadmium equivalent pressure relationship under fixed stress and temperature.

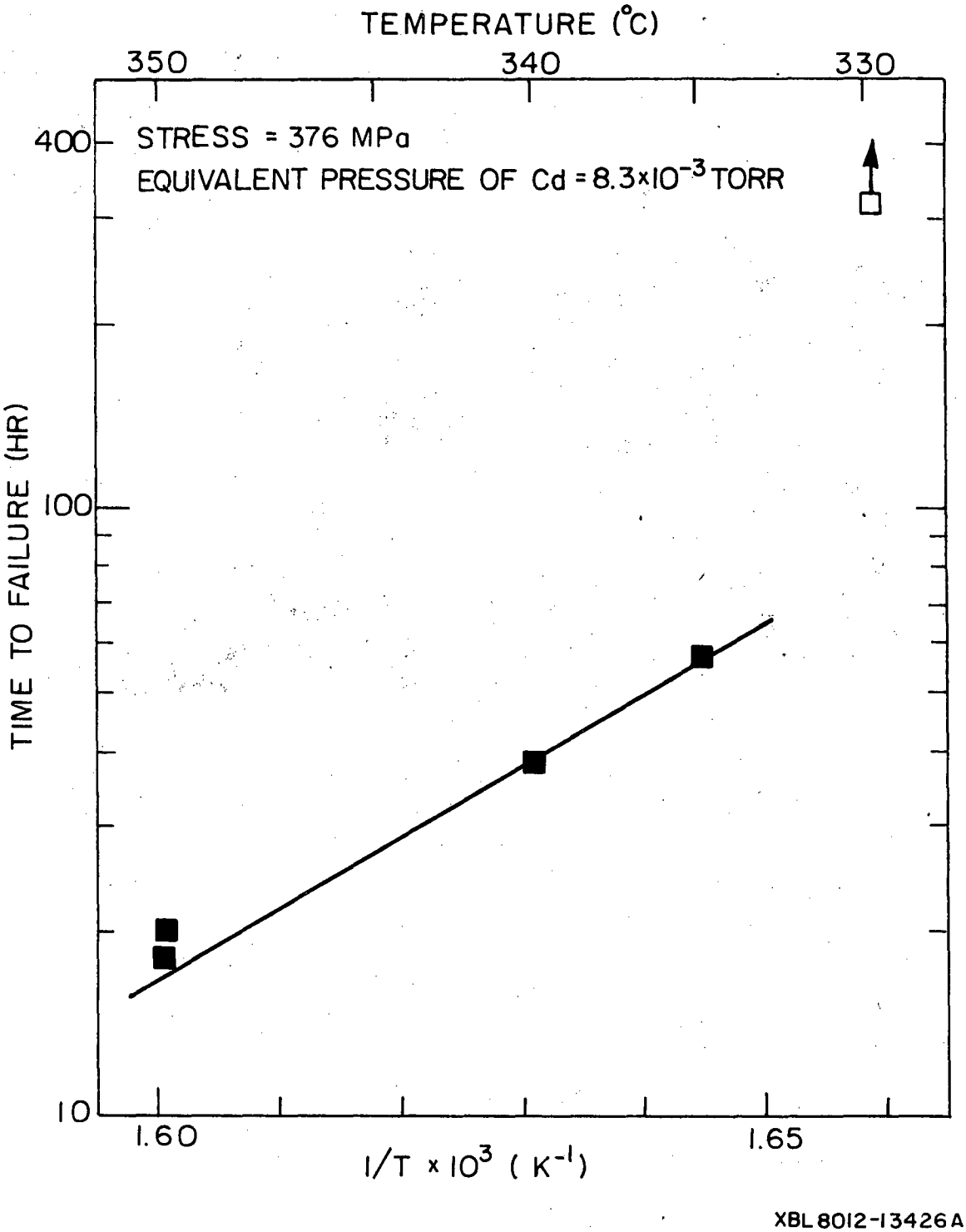

Fiugre 7-4. Time-to-failure vs. temperature relationship under fixed stress and cadmium equivalent pressure.

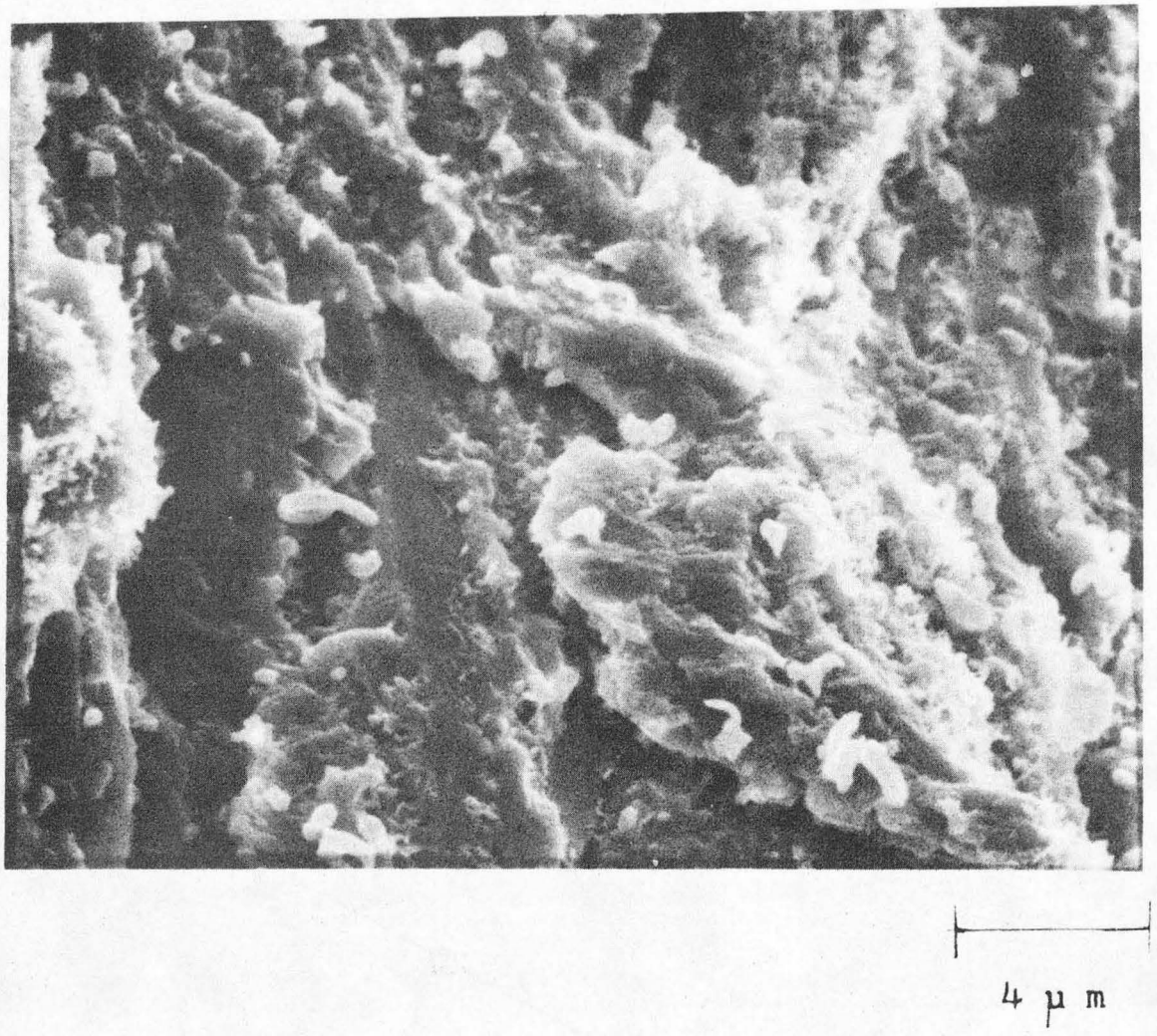

XBB 816-5494

Figure 7-5. SEM fractography of burst-failed specimen in Fig. 7-1.

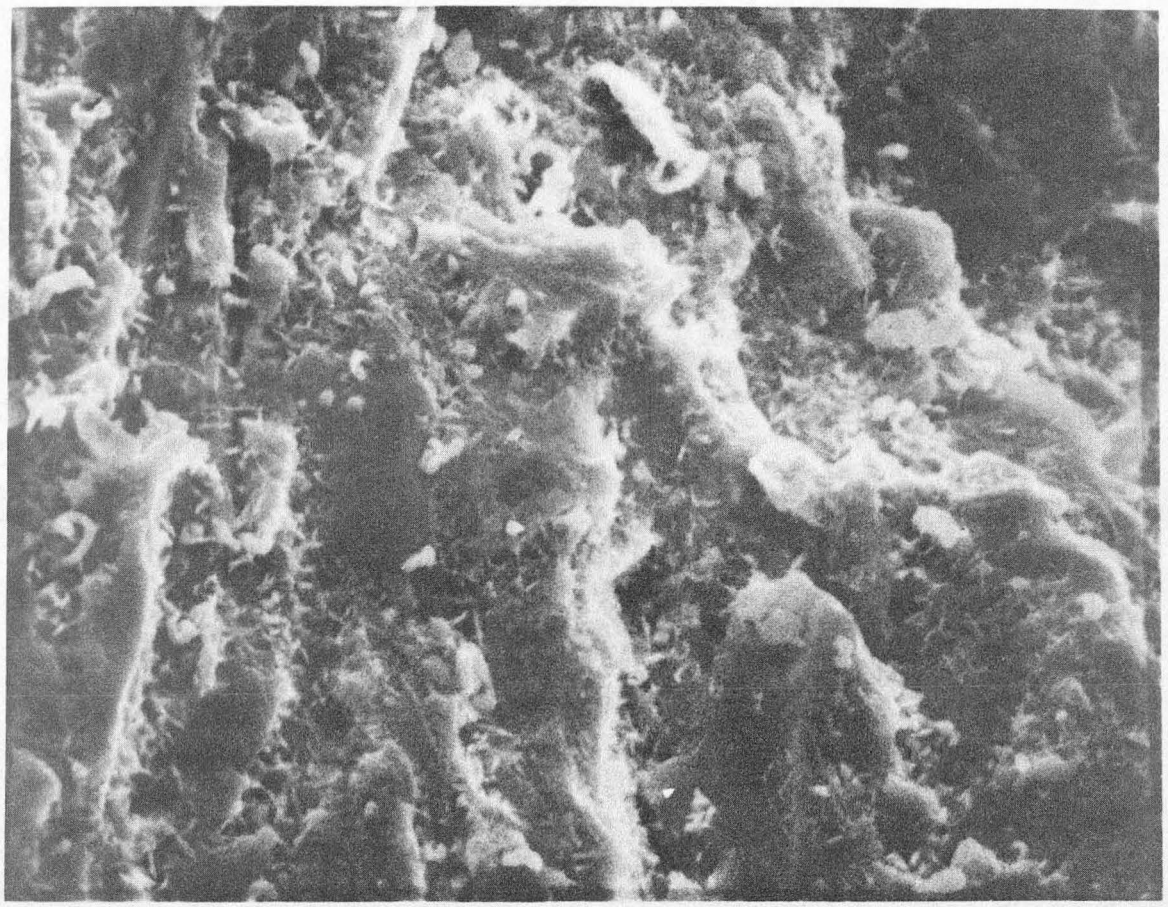

4 μm

XBB 816-5524

Figure 7-6. SEM fractography of burst-failed specimen in Fig. 7-1.

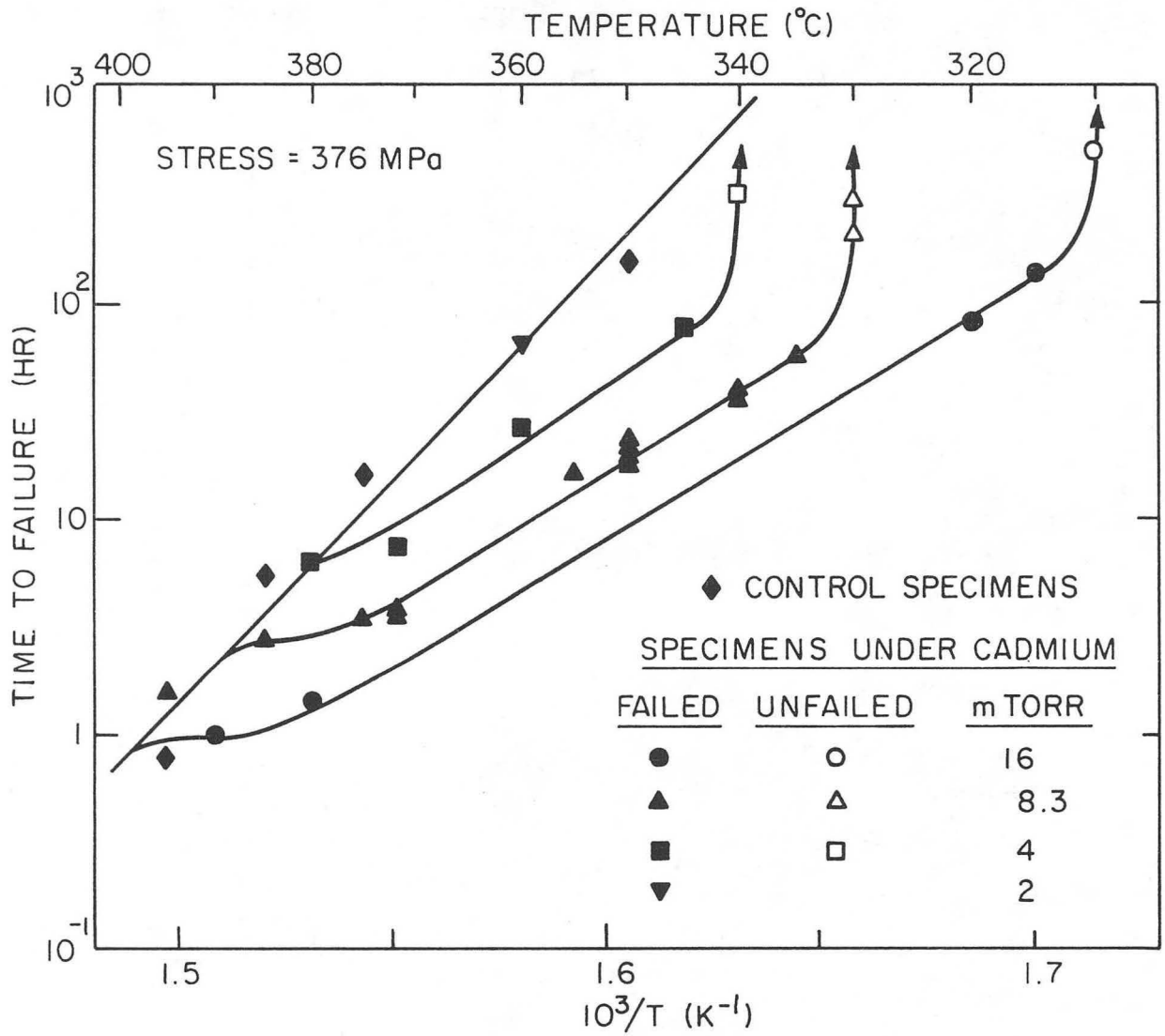

Figure 7-7. Temperature window study for cadmium vapor embrittlement.

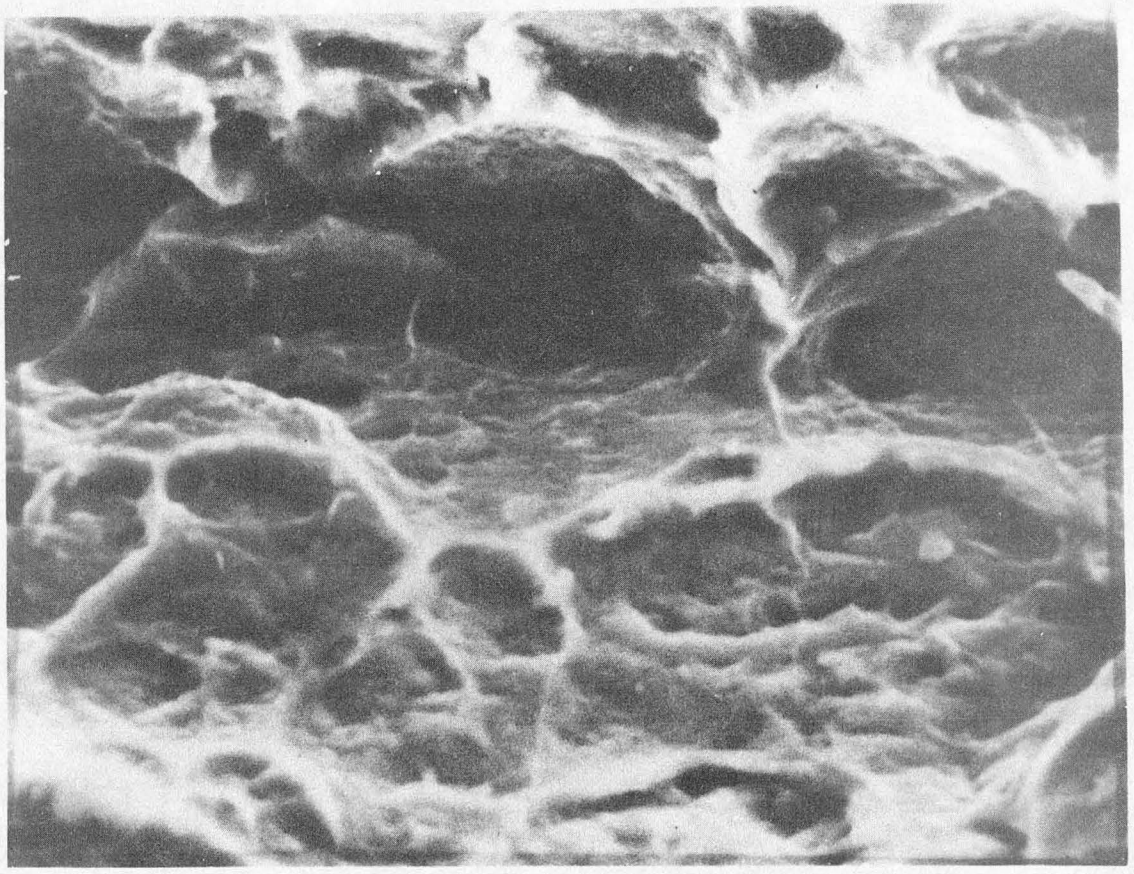

4 μm

XBB 816-5504

Figure 7-8. Fractography of specimen failed under 395°C, 376 MPa, 8.3×10^{-3} torr Cd after 1.6 hrs.

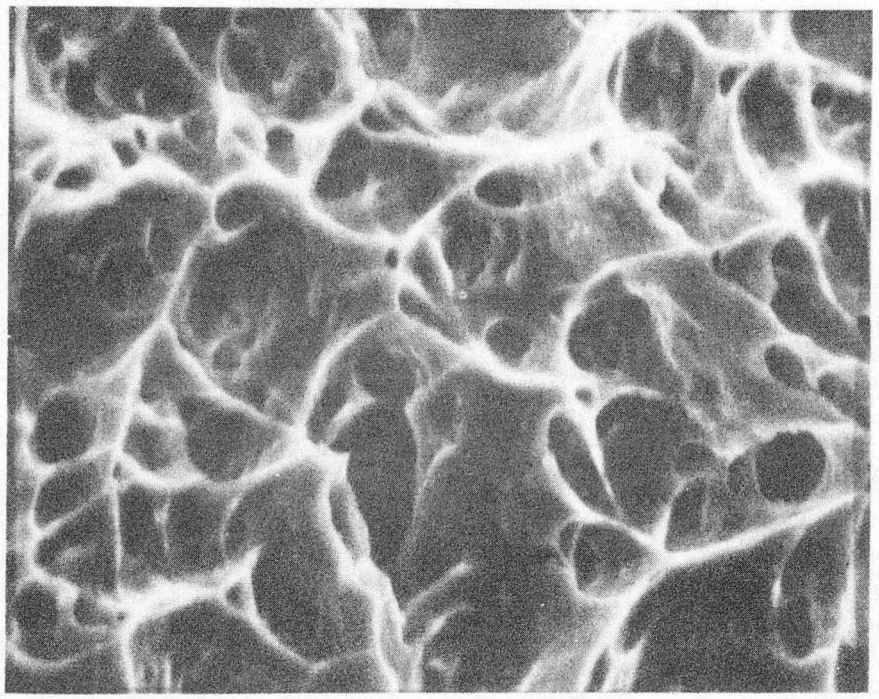

4 μm

XBB 817-7015

Figure 7-9. Fractography of specimen tested under 2 mtorr and 360°C showing ductile dimple fractography.

8. EFFECT OF CESIUM IODIDE ON THE FAILURE TIME OF ZIRCALOY

8.1 Introduction

Iodine is a well known stress corrosion cracking (SCC) agent of zircaloy. Inside a reactor fuel pin, iodine will be present mainly as cesium iodide according to thermodynamics.[15] In pile, iodine may be liberated by radiolysis of CsI,[36] which is the reason for investigating cesium iodide stress corrosion cracking with and without irradiation.

8.2 Experimental

8.2.1 Nonirradiated Case The experiment utilizes the tube-burst (biaxial) test mode. The apparatus is the same as that used in metal iodide tests without radiation. Cesium iodide crystals are placed in a Knudsen cell and heated to a temperature sufficient to create a molecular beam of a desired equivalent pressure impinging on the zircaloy specimen surface (Section 2.4).

8.2.2 Irradiated Case For the irradiation study, a Van de Graaff accelerator is connected to the apparatus used in the nonirradiated case. The H^+ beam from the accelerator and the cesium iodide molecular beam strike the same spot on the zircaloy specimen. Internal pressurization of the closed tubular specimen with argon produces the biaxial stress state. However, when the specimen fails, the argon flows out of zircaloy tube into the vacuum system and the Van de Graaff accelerator tube. To prevent this abrupt pressure rise from damaging the accelerator, a slammer valve[21] is placed between the reaction chamber and the accelerator. As soon as the pressure reading of ion

gauge on the reaction chamber increases, the slammer valve is automatically fired and closes to isolate the two regions in 0.2 msec. This time period is short enough to prevent the shock wave of released argon from reaching the Van de Graaff accelerator tube.

8.3 Materials

Zircaloy-4 tubing from Sandvik Special Metals Co. lot No. JV 11 is tested. Detailed information on these materials is given in Table 5-1.

8.4 Results

8.4.1 Cesium Iodide Affected Specimens Without Irradiation

The time-to-failure versus stress results are shown in Fig. 8-1. The data points and fitted curve of the control specimens (without corrosive agent) are included in the figure for comparison. There is no effect of cesium iodide on zircaloy failure lifetime. Specimen failure under CsI is of the burst-type (Fig. 8-2) and the fractography is completely ductile (Fig. 8-3). There are some white deposits on the fracture surface which give higher cesium and iodine EDAX signals than that of the overall surface. EDAX signal from the outside surface of cesium iodide-affected region (Fig. 8-4) show only cesium and iodine (44 percent I and 56 percent Cs [atomic percent]).

8.4.2 Specimen with Irradiation Only

Because of University regulations, the Van de Graaff accelerator can be operated only from 8:00 a.m. to 5:00 p.m. Therefore, the experiment utilizes step function loadings for failure lifetimes longer than eight hours. Temperature and irradiation are applied during the daytime for eight hours and turned off during the night. The time to

failure is the sum of the time periods that the specimen was under irradiation and temperature before fracture. One specimen was tested under 386 MPa, 350°C and 0.35 MeV, 5 μA H_2^+ beam current. The failure time was 22.7 hrs in comparison with 24.3 hrs for control specimens in continuous test mode without irradiation. The fracture is burst-type, and the fracture surface shown in Fig. 8-5 is ductile dimpe, the same as that of control specimens without radiation and corrosive agent. The effect of irradiation and the step function loading on the mechanical response of zircaloy is negligible. We will use this result as a reference state for the CsI irradiation study.

8.4.3 Irradiated and Cesium Iodide Affected Specimens For experiments with cesium iodide and irradiation, the availability of cesium iodide is also a step function as the temperature and irradiation discussed in the previous section. Five experiments were completed under 386 MPa hoop stress, 350°C, and irradiation condition defined by 350 keV, 5 μA H_2^+. The CsI equivalent pressures used were 10^{-3}, 4×10^{-4}, 10^{-4}, 5×10^{-5}, and 10^{-5} torr. Table 8-1 gives the test results. None of the specimens failed after 22 hrs, which is when the tests were terminated. Figure 8-6 is a photo of the specimen under 4×10^{-4} torr, which shows a white CsI deposit on the tube surface. The black region is the area struck by the positive ion beam, which exhibits a thinner CsI film because of ion sputtering.

8.5 Discussion

8.5.1 Unirradiated Cesium Iodide Affected Specimens The specimens failed under cesium iodide only in a burst-mode (Fig. 8-2) and the

fractography was ductile (Fig. 8-3). There was no decrease in time-to-failure due to the presence of CsI (Fig. 8-1). We can conclude that cesium iodide does not cause stress corrosion cracking of zircaloy without radiation. The same (negative) result has been observed by Cubicciotti and Jones.[13]

8.5.2 Irradiated and Cesium Iodide Affected Specimens Five specimens were tested 3.5 MeV, 5 μA H_2^+ bombardment over a two-order-of magnitude range of CsI equivalent pressures. None of them failed during the 22 hrs test perod (Table 8-1). In other studies no failure was observed in the inpile cesium iodide irradiation stress corrosion cracking tests of Davis et al.,[37] and Wood et al.[38] The idea that molecular or atomic iodine released from CsI by radiation can activate stress corrosion cracking of zircaloy does not appear to be substantiated.

8.5.3 Film Formation in Irradiated and Cesium Iodide Affected Tests Three mechanisms determine the CsI thickness on zircaloy:

(A) Sticking of the Incident Beam

The incident CsI beam can serve as a CsI source. The equivalent pressure is calculated from the primary molecular beam intensity (see Section 2-4):

$$I_{ads} = P_{eq} \Big/ \sqrt{2\pi m k T_K} \qquad (8\text{-}1)$$

Where P_{eq} is the equivalent pressure, m is the mass number, k is the gas constant, and T_K is the Knudsen cell temperature. The sticking probability of CsI molecule is assumed to be unity. The

results of I_{ads} for different incident CsI beam equivalent pressures are given in Table 8-2.

(B) Desorption

The desorption rate of CsI from zircaloy is proportional to the vapor pressure of CsI at the specimen temperature:

$$I_{des} = P_{vap} \Big/ \sqrt{2\pi mkT} \qquad (8\text{-}2)$$

Where T is the zircaloy specimen temperature, and P_{vap} is the CsI vapor at 350°C (5×10^{-6} torr). We find $I_{des} = 3.7 \times 10^{14}$ molecules/cm^{2}sec at 350°C (Table 8-2). Therefore, a CsI film can form on zircaloy surface for some high CsI availability tests ($I_{ads} > I_{des}$). This phenomenon does not happen for iodine, aluminum iodide, iron iodide, and cadmium because $I_{des} > I_{ads}$ under all conditions.

(C) Ion Sputtering

The bombardment by H_2^+ can cause ion sputtering of the CsI film from the zircaloy surface. H_2^+ is the majority species in the Van de Graaff machine rather H^+ and H_3^+. As a 350 keV H_3^+ strikes the specimen surface, it splits into two protons each with half of the original H_2^+ energy.[39] The sputtering rate of solid is calculated by Smith's model,[32] which gives 2.1×10^{16} molecules/cm^{2}sec leaving the surface for 175 keV, 10 μA proton bombardment.

The calculated film thickness after 22 hrs of testing, including those mechanisms discussed above, are shown in the next-to-last column of Table 8-2.

By graphical and numerical integration of Northliffe and Schilling Tables,[40] we find the range of 175 keV H^+ in CsI is about 3 μm. In order to make sure that the proton can penetrate to the metal/CsI interface, measurement of the CsI film thickness is important. Four methods were used here to check the CsI film:

(A) Visual Method during the Experiments

During ion bombardment of ceramic targets, there is a blue light in the bombarded region arising from the discharge of positive hydrogen ions. This phenomenon does not exist for conducting metallic targets. For the 10^{-3} and 4×10^{-4} torr experiments, we observed the blue light during testing, which means that a ceramic layer was formed on zircaloy surface. For other three low CsI pressure tests (10^{-4}, 5×10^{-5}, and 10^{-5} torr), no blue light was observed during the experiments; the specimen surface was conductive.

(B) Visual Appearance after the Experiment

We found white CsI deposits on the specimens after high CsI pressure tests (10^{-3} and 4×10^{-4} torr) (Fig. 8-6). There was no CsI deposit on the specimens after low CsI pressure tests (10^{-4}, 5×10^{-5}, and 10^{-5} torr); as shown in Fig. 8-7, the black triangular mark caused by ion bombardment was the only mark on the zircaloy.

(C) Optical Microscopy

Specimens were mounted with Kold Mount resin, cut and polished at the position of the deposit, and the film thickness measured by optical microscope. We found a 30 μm film on the 10^{-3} torr specimen (Fig. 8-8). Compared with 34 μm from the adsorption, desorption, and sputtering calculation (Table 8-2), the agreement is good. The search for CsI on the 10^{-4} torr specimen failed; either the polishing and cleaning agents etched out the CsI film, or vibration during the process loosened it.

(D) EDAX Analysis

Specimens taken out of the apparatus were delivered to the SEM for EDAX analysis. For the 4×10^{-4} torr experiment, the surface CsI films inside and outside of the ion bombardment region are shown in Fig. 8-9 (46 atom percent I and 54 atom percent Cs) and Fig. 8-10 (44 atom percent and 56 atom percent Cs), respectively. Figure 8-11 shows the transition zone between them.
EDAX detects only Cs, I, but no Zr, which means that CsI film was thicker than 3 μm, the x-ray penetration distance. The signal from underlying zirconium metal cannot penetrate the film to reach the detector. The calculated value of the CsI film thickness for this case is 3.4 μm (Table 8-2).

For the 5×10^{-5} and 10^{-5} torr specimens, no CsI film was detected (Fig. 8-12). This is expected from our calculation (Table 8-2). Only some white deposits, containing Cs, I, and Zr appear on the iodide-affected and bombarded surfaces (Fig. 8-12). The density of these deposits for the 5×10^{-5} torr experiment is higher than that for the 10^{-5} torr test.

8.5.4 Effect of Film Thickness The range of 175 keV H^+ in CsI is 3 μm. If the CsI film is thicker than the radiation can not reach the metal CsI interface. In this case, no iodine will be released near the zirconium metal. From chemical point of view, we wish to use the highest possible CsI impingement rate. But high CsI supply rates produce film > 3 μm thick which protect the film/metal interface from irradiation. At the other extreme, a low CsI impingement rate will insure a thin film (or submonolayer surface concentrations). But even with radiolytic decomposition of adsorbed CsI, the concentration may be too low to produce SCC.

8.5.5 Energy Deposition Rate from the Proton Beam Compared with the Inpile Environment For low iodine equivalent pressure tests (5×10^{-5} and 10^{-5} torr), no CsI film was detected by EDAX, because the net adsorption rate was negative (Table 8-2). The radiation deposits all of its energy in the zircaloy in these two tests. A 175 keV, 10 μA proton current is formed at the zircaloy surface by bombardement with 350 keV, 5 μA H_2^+ particles.[38] From the Northliffe and Schilling Table,[40] the range this energy proton in zirconium is 1.1 mg/cm^2 (1.8 μm). The energy deposition rate is then:

$$= (0.175 \times 10^6 \text{ ev} \times 1.6 \times 10^{-12} \text{ erg/eV}) \qquad (8\text{-}1)$$

$$\times[(10^{-5} \text{ coulomb/sec})/(1.6 \times 10^{-19} \text{coulomb/electron charge})]$$

$$/(1.1 \times 10^{-3} \text{ gcm}^{-2})$$

$$= 1.6 \times 10^{10} \text{ erg/g-sec}$$

$$= 1.6 \times 10^{8} \text{ rad/sec}$$

For a fuel rod inpile, fission fragment recoil from the outer fuel surface is the most important energy deposition mechanism.[39] The fission fragment recoil current is given by[41]

$$I_{tot}^{rec} = (1/2)\dot{F}\mu_{ff} \tag{8-2}$$

where μ_{ff} is the range of fission fragments in UO_2 and for a fuel pellet of radius R operating at linear power P.

$$\dot{F} = P/(3.2 \times 10^{-11}\ \pi R^2)$$

we take the stopping power of iodine in silver (26 keV $\mu g^{-1} cm^2$)[42] as an approximation[39] for fission fragments in zircaloy.[39] For a 50 MeV fission fragment,[39] we find the range is about 3 μm and dose rate is about 1.6×10^6 rad/sec (R = 0.5 cm and = 300 W/cm).

Thus, the proton beam delivers ~100 times as much energy to the cladding as fission fragment recoil during irradiation. Nonetheless, we find no irradiated CsI stress corrosion cracking of zircaloy at any CsI equivalent pressure.

Table 8-1 Radiation enhanced CsI test results

Test Mode	Continuous		Discontinuous				
CsI Equivalent Pressure (torr)	0	0	10^{-3}	4×10^{-4}	10^{-4}	5×10^{-5}	10^{-5}
Radiation Intensity	0	3.5 MeV 5 μA H_2^+	3.5 MeV 5 μA H_2^+	3.5 MeV 5 μA H_2^+	3.5 MeV 5 μA H_2^+	3.5 MeV 5 μA H_2^+	3.5 MeV 5 μA H_2^+
Failure Time (hr)	24.3	22.7	*	*	*	*	*
CsI Film Thickness (μm)	--	--	30	> 3		None	None
CsI film Detected Method			c	d		a,b,d	a,b,d
I_{ads} / $I_{des} + I_{sput}$	--	--	> 1	> 1	< 1	< 1	< 1

Stress = 386 MPa
Temperature = 350°C

* No failure after 22 hrs of testing
a Visual (during experiment) (i.e., blue light)
b Visual (post-test)
c Optical microscopy
d EDAX analysis

Table 3-2 Adsorption, Desorption, and Sputtering Calculation (Specimen Temperature = 350°C, Test Time = 22 Hours)

P_{eq}(torr)	I_{ads} (molecules/cm^{2}sec)	I_{des} (molecules/cm^{2}sec)	I_{sput} (molecules/cm^{2}sec)	I_{net}= $I_{ads} - (I_{des}+I_{sput})$	FILM THICKNESS (μm) By Calculation*	By Experiment
10^{-3}	6.1×10^{16}	3.7×10^{14}	2.1×10^{16}	> 0	34	30
4×10^{-4}	2.5×10^{16}	3.7×10^{14}	2.1×10^{16}	> 0	3.4	≥ 3
10^{-4}	6.4×10^{15}	3.7×10^{14}	2.1×10^{16}	< 0	None	—
5×10^{-5}	3.3×10^{15}	3.7×10^{14}	2.1×10^{16}	< 0	None	None
10^{-5}	6.7×10^{14}	3.7×10^{14}	2.1×10^{16}	< 0	None	None

* The film thickness(δ) was calculated from the net adsorption rate I_{net} and the test time.

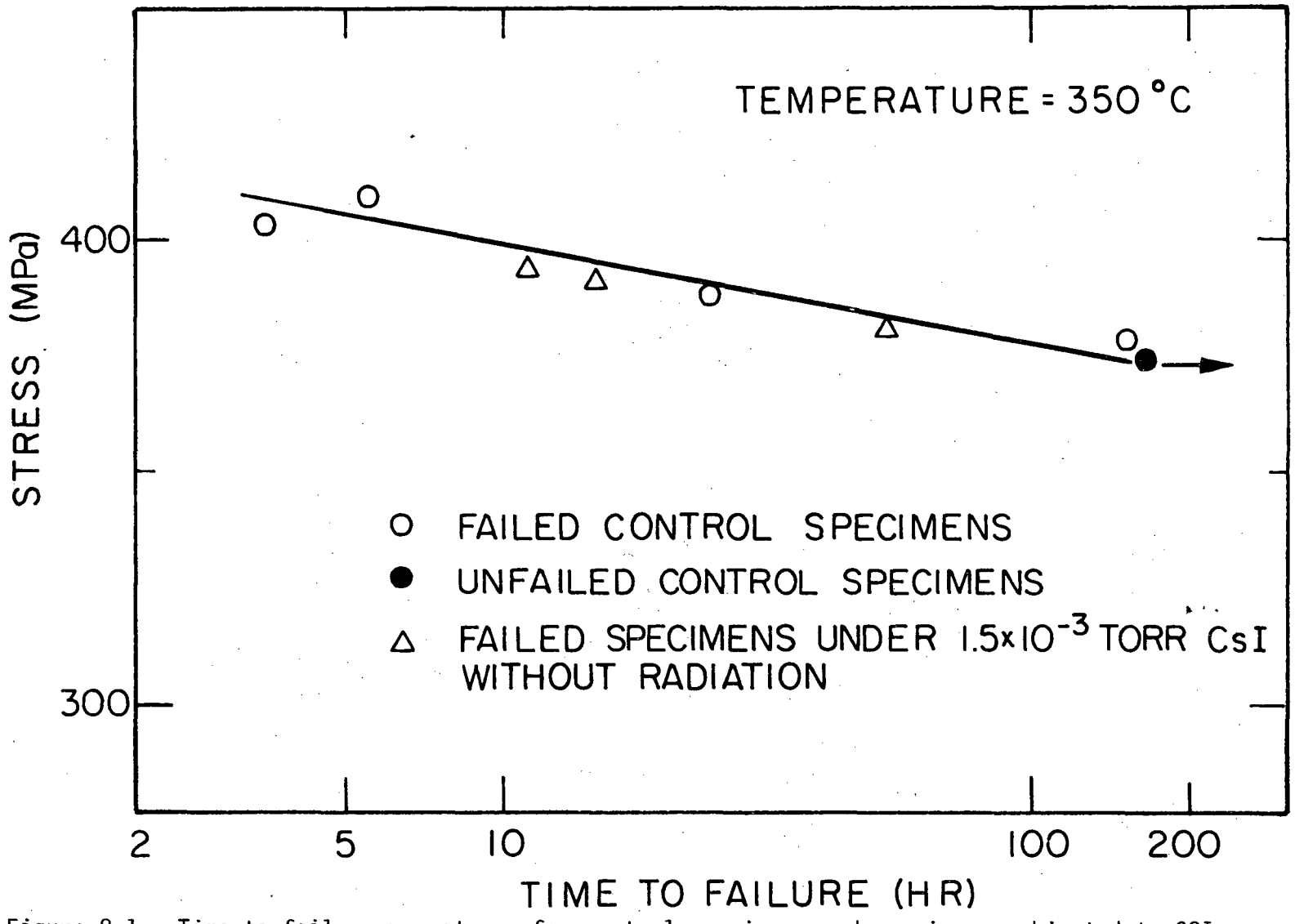

Figure 8-1. Time-to-failure vs. stress for control specimens and specimens subjected to CSI.

XBL812-5221A

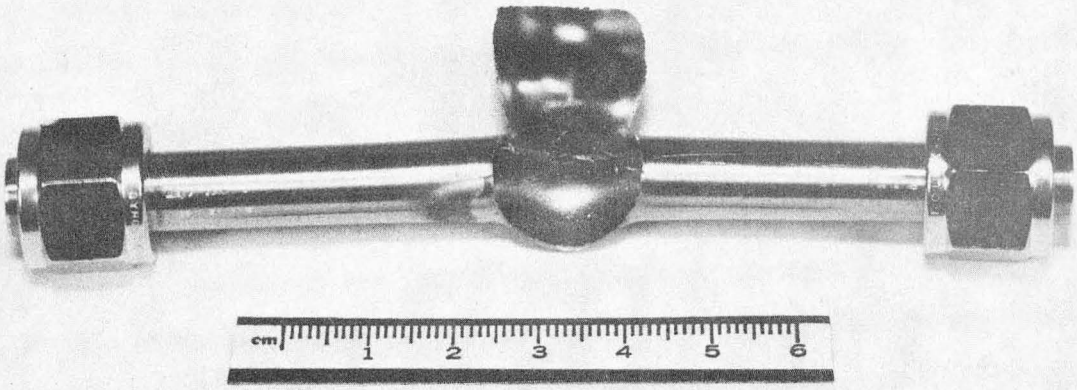

XBB 800-12747

Figure 8-2. Burst-type failure of specimen under 395 MPa, 1.5×10^{-3} torr CsI, and $350^{\circ}C$ after 11 hours.

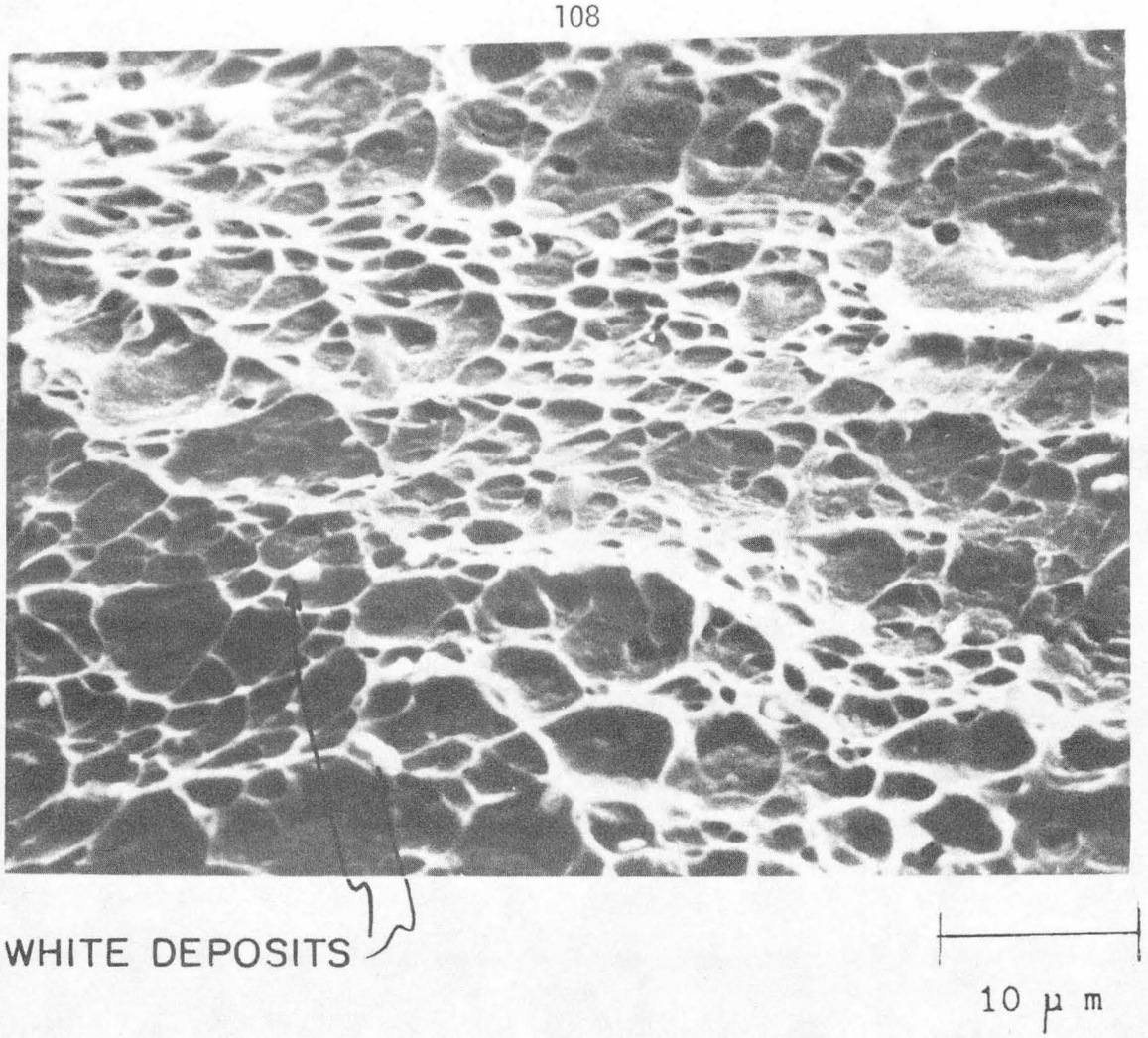

XBB 816-5497A

Figure 7-3. Fractography of specimen in Fig. 8-2.

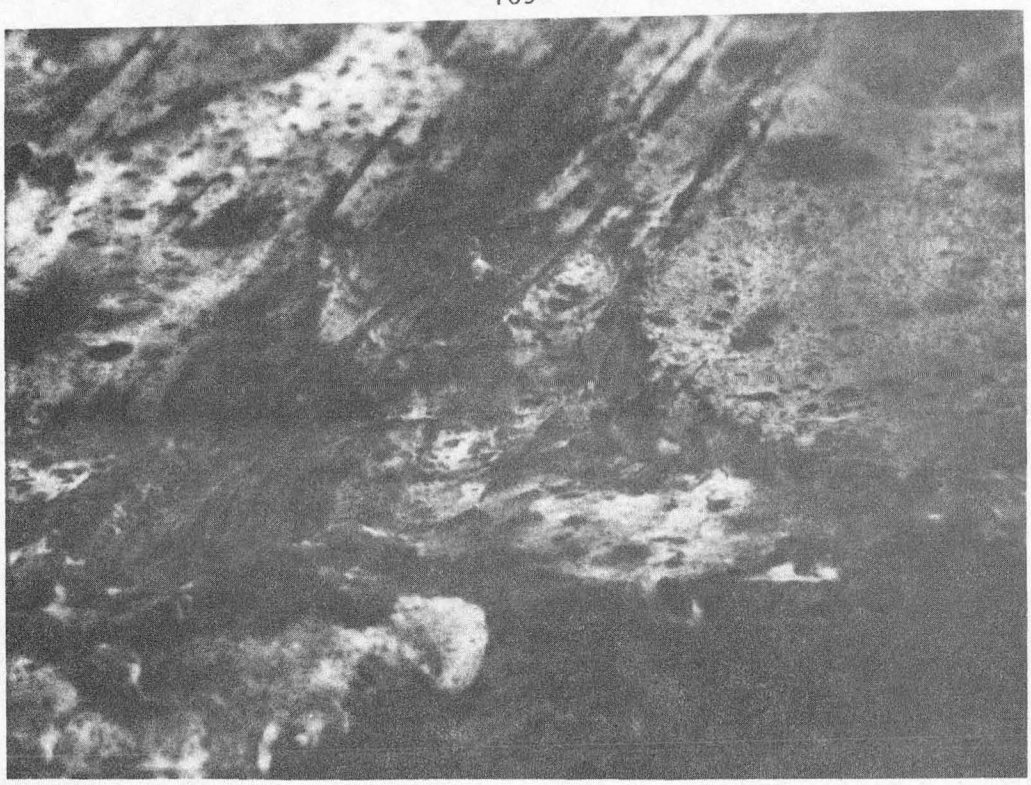

20 μ m

XBB 816-5519

Figure 8-4. CsI-affected region on O.D. surface of specimen in Fig. 8-2.

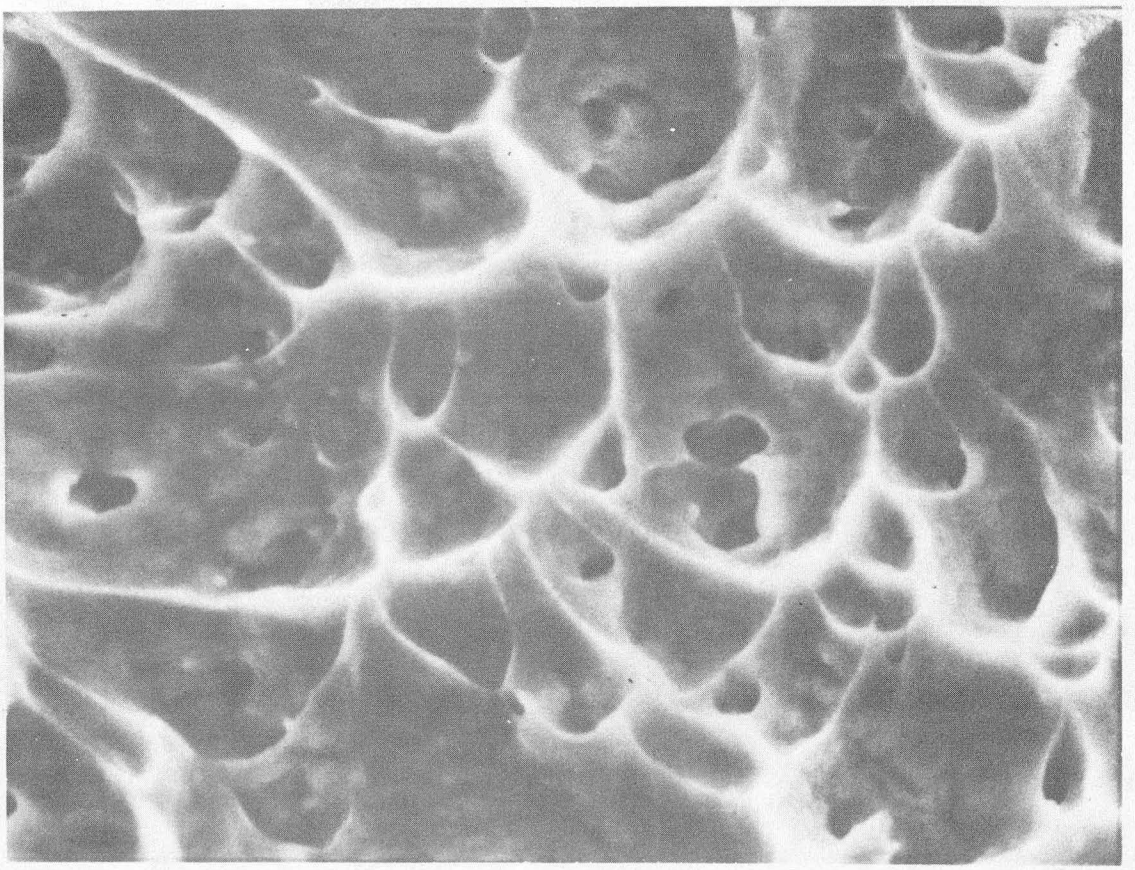

4 μm

XBB 816-5498

Figure 8-5. Fractography of the specimen tested under radiation without CsI.

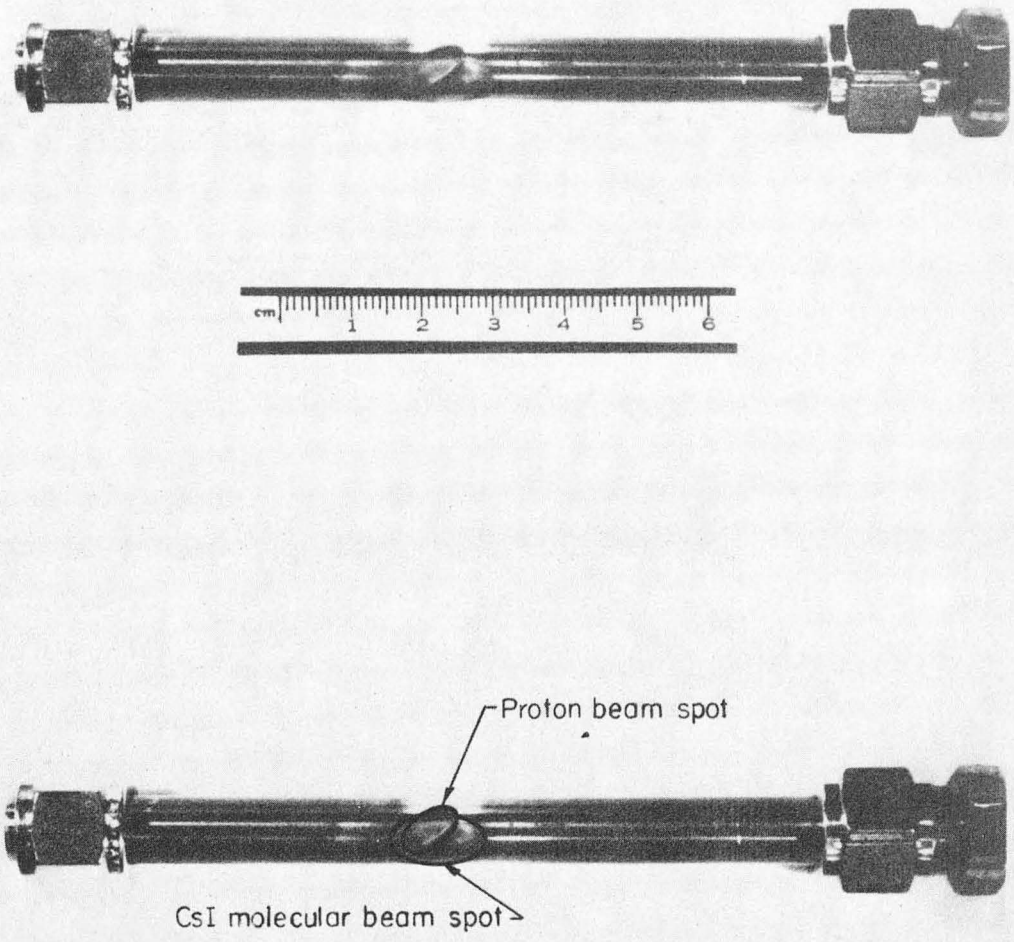

XBB 817-7014A

Figure 8-6. Specimen tested under 4 x 10^{-4} torr CsI, 386 MPa, and 0.35 MeV, 5 μA, H_2+ irradiation.

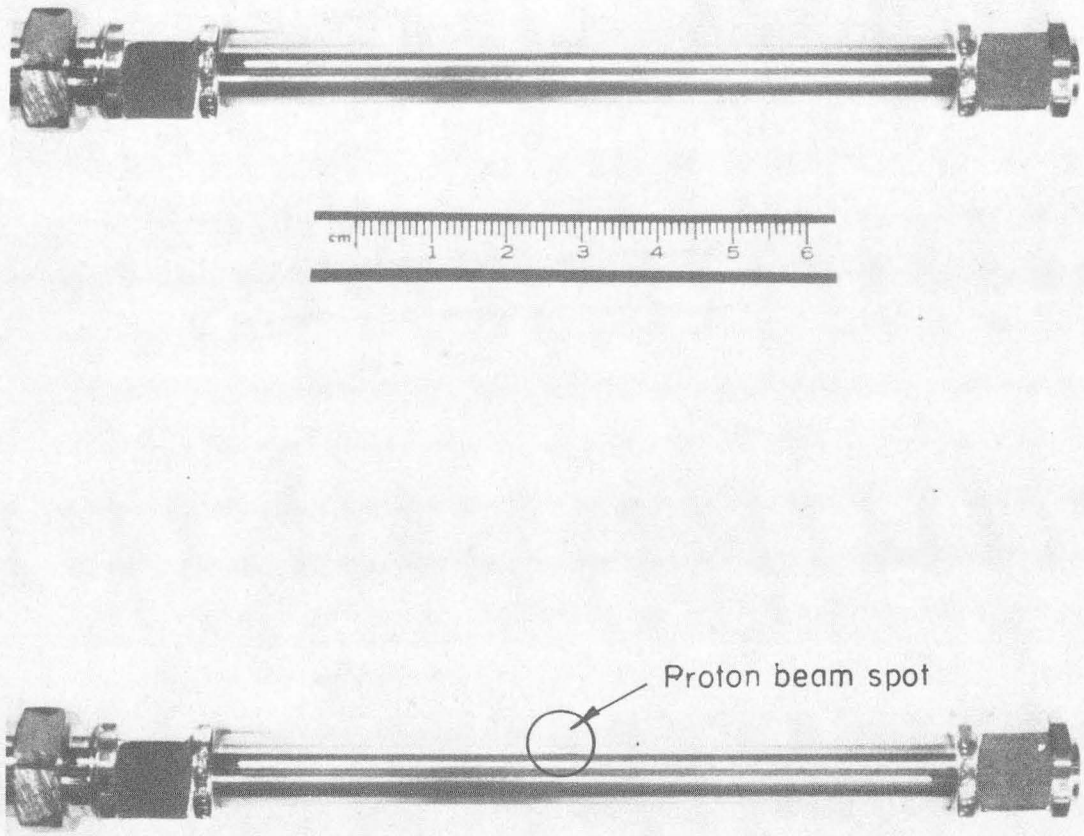

XBB 817-7013A

Figure 8-7. Specimen tested under 5 x10^{-5} torr CsI, 396 MPa, 350°C, and 0.35 MeV, 5 μA, H_2+ irradiation.

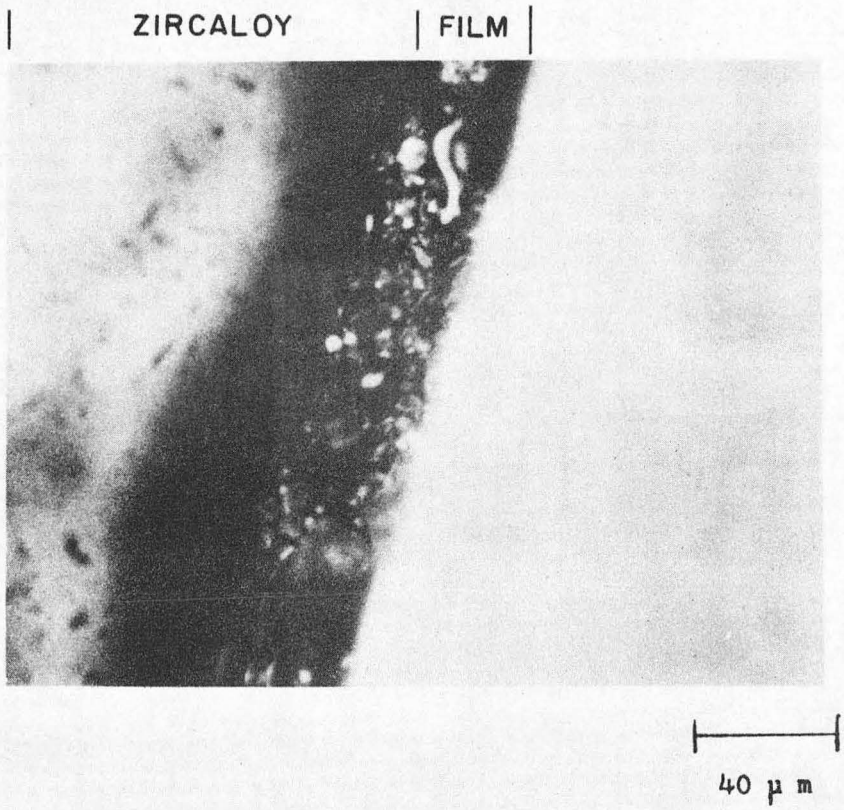

XBB 816-5510A

Figure 8-8. Optical microscopy of the film on specimen under 10^{-3} torr CsI, and radiation for 22 hrs.

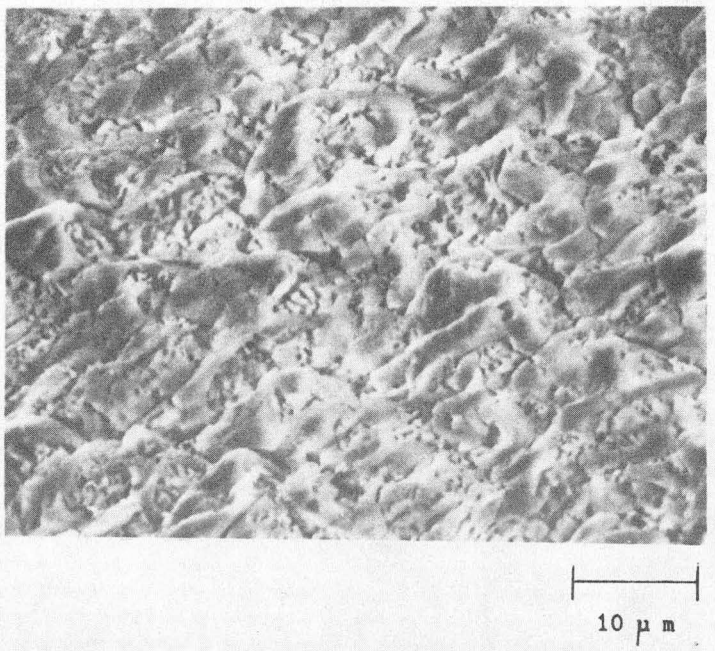

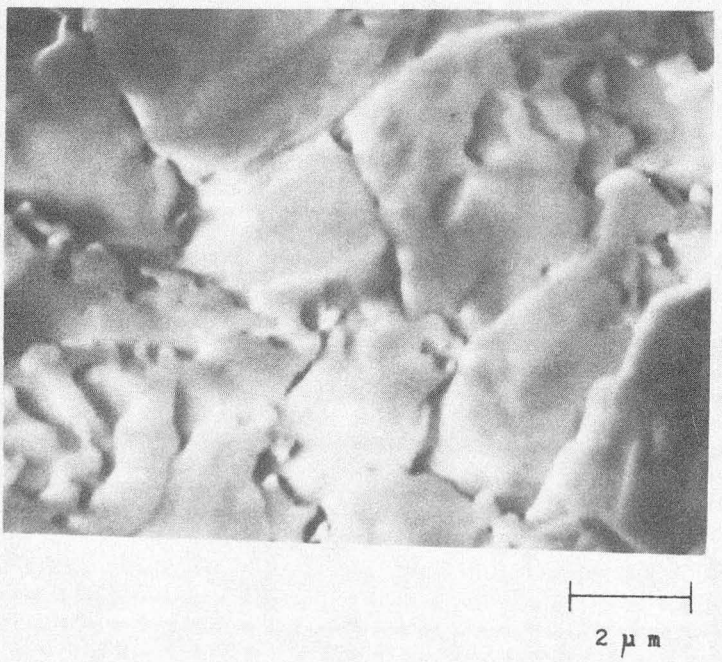

XBB 816-5537A

Figure 8-9. Cesium iodide and radiation-affected region on specimen subject to 4×10^{-4} torr CsI (46 atom % I and 54 atom % Cs). No cracks visible.

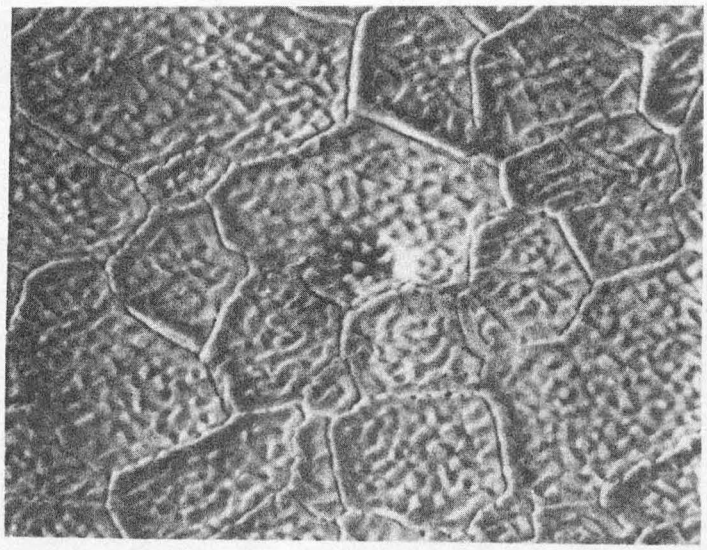

10 μm

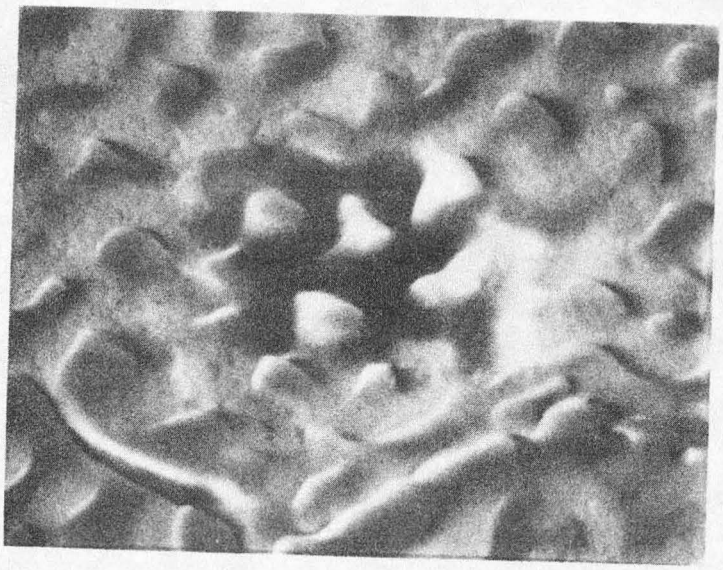

2 μm

XBB 816-5508A

Figure 8-10. Cesium iodide-affected zone outside the irradiation region on specimen in Fig. 8-6 (44 atom % I and 56 atom % Cs).

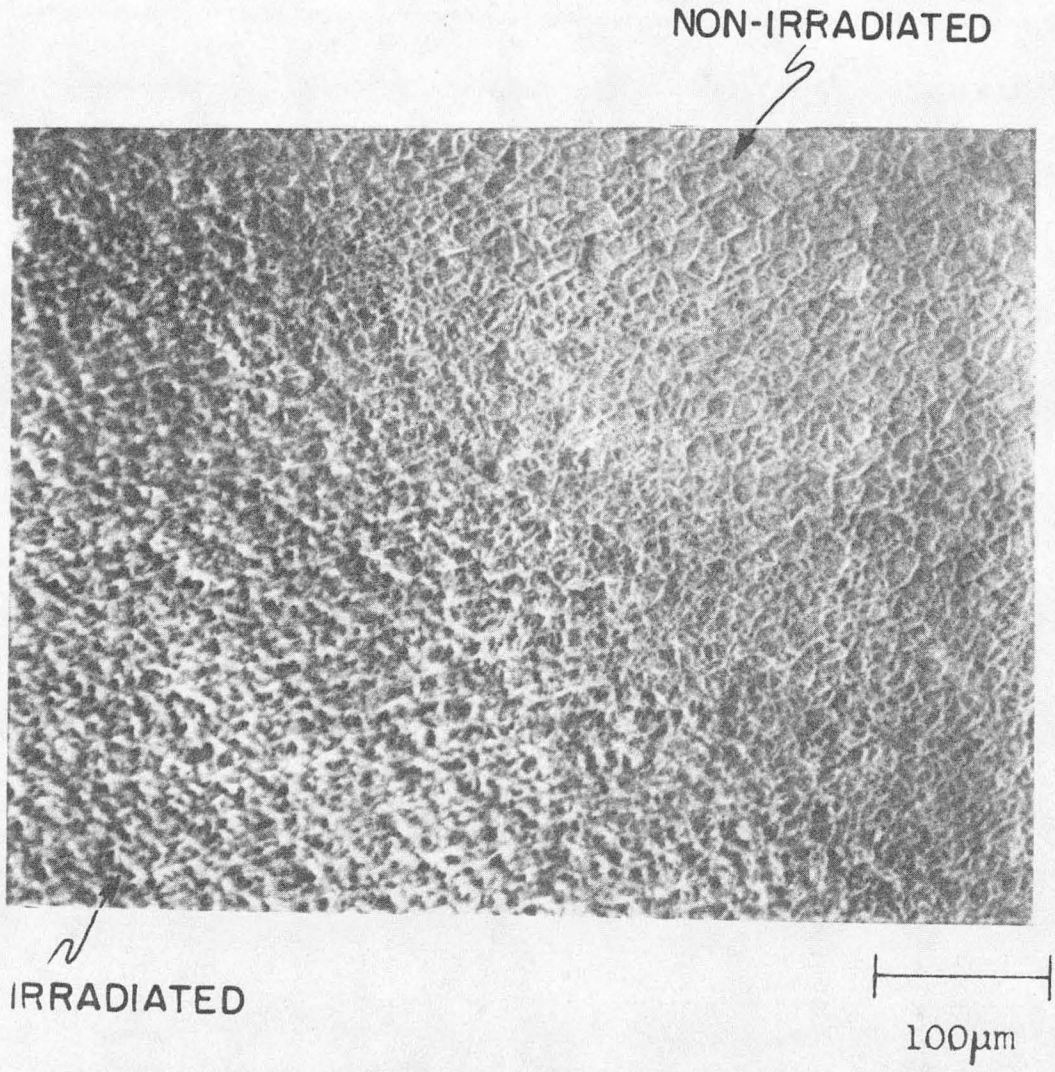

XBB 816-5536A

Figure 8-11. The transition zone between Fig. 8-9 and 8-10.

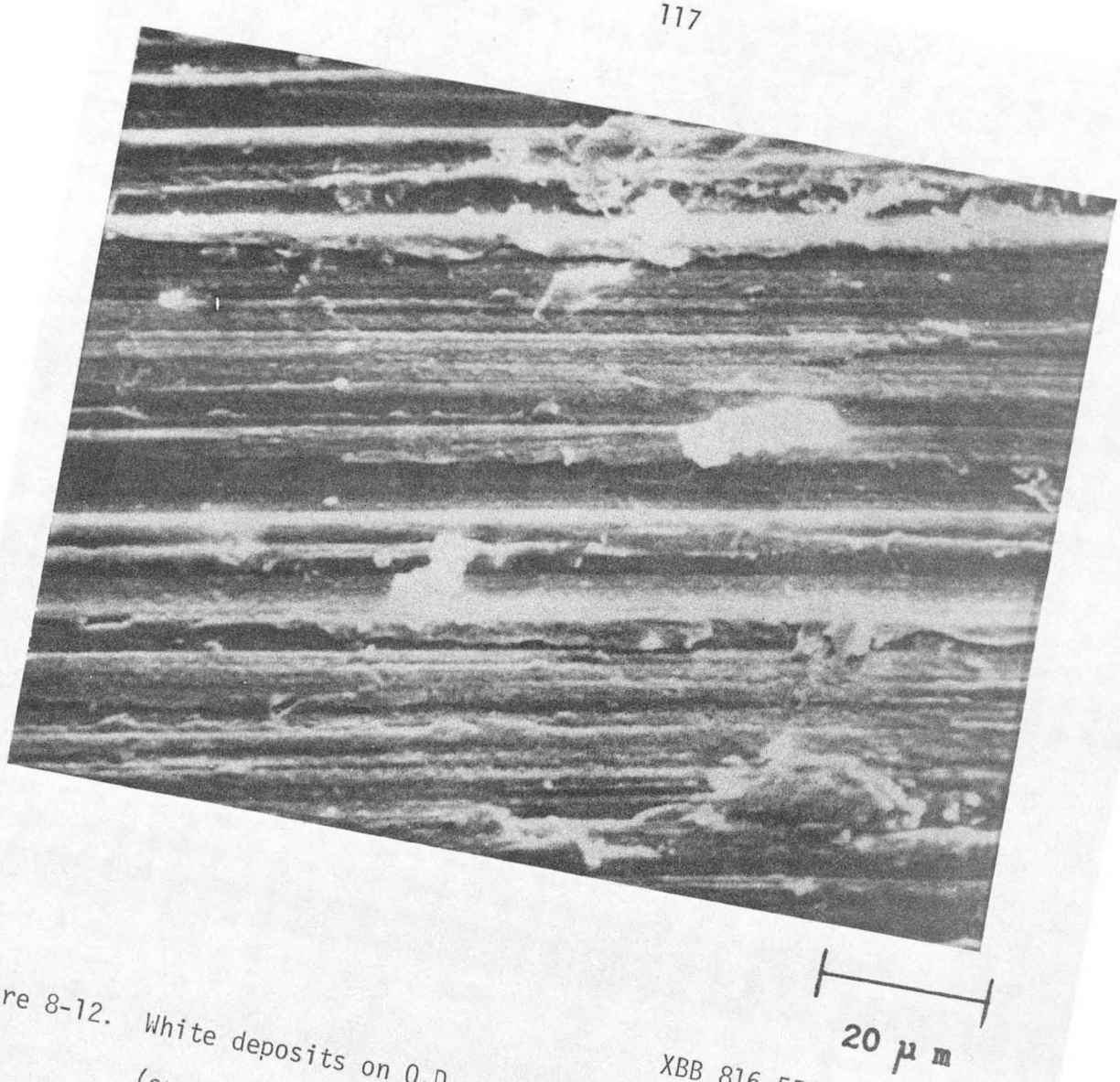

XBB 816-5526

Figure 8-12. White deposits on O.D. surface of the specimen in Fig. 8-10 (on the CsI-H_2^+ spot).

9. DISCUSSION

9.1 Crack Propagation Controls the Failure Time

According to the crack initiation study discussed in Chapter 6, we find that the crack is initiated within 20 percent of the specimen's lifetime, which suggests that crack propagation is the slow step in SCC of zircaloy. Since the assumption of small strains is valid for stress corrosion cracking of zircaloy, the crack propagation model for brittle solids[28,30,43] can be applied.

9.2 Proposed Environment Affected Crack Propagation Model

Following Weiderhorn[30,43] and Evans,[28] adsorption of reaction of chemically active species at the crack tip can lead to slow crack growth. We can assume that the reaction

$$2I_{(ads)} + Zr_{(s)} \longrightarrow ZrI_{2(s)} \qquad (9\text{-}1)$$

occurring at the crack tip is the rate-determining process. If the velocity of the crack is controlled by the rate of reaction at the crack tip, the crack velocity is proportional to the reaction rate. From absolute-rate theory,[29] the rate of reaction (9-1) is proportional to:

$$(kT/h)[I_{ads}]^2[Zr]\exp(-\Delta G^*/RT) \qquad (9\text{-}2)$$

Where k, T, h, and R are the Boltzmann constant, absolute temperature, Planck's constant, and gas constant, respectively. ΔG^* is the change

in free energy as the reaction passes from the initial to the activated state.

The free energy of activation can be divided into four terms:

$$\Delta G^* = \Delta E^* - T\Delta S^* + \sigma'\Delta V^* + V_m\nu/\rho \qquad (9\text{-}3)$$

Where ΔE^* is the activation energy, ΔS^* the activation entropy, and ΔV^* the activation volume. The last term represents the change in free energy of reactants resulting from surface curvature; V_m is the molar volume of the solid, ν the surface tension of gas-solid interface, and ρ the radius of curvature at the crack tip. σ', the principle tensile stress at the crack tip is related to the stress intensity factory K by:

$$\sigma' \propto K \qquad (9\text{-}4)$$

The crack velocity is proportional to rate of reaction

$$da/dt \propto (kT/h)[I_{ads}]^2[Zr]\exp(-\Delta E^*/RT)\exp(BK/T) \qquad (9\text{-}5)$$

Since the experimental range of T is small, the linear dependence of T is minor in comparison to exponential dependence. We get

$$da/dt = A'[I_{ads}]^2\exp(-\Delta E^*/RT)\exp(BK/T) \qquad (9\text{-}5)$$

Where A' is a constant independent of stress, temperature, and adsorbed iodine concentration. Now $[I_{ads}]$ will be determined for the different iodine-bearing gases which bombard the zircaloy surface.

9.2.1 Iodine The surface iodine population is assumed to be in equilibrium with the supply from the molecular beam:

$$I_2(g) \Longleftrightarrow 2I_{(ads)} \tag{9-6}$$

$$[I_{ads}] = \sqrt{K_1}\ P_1^{\ 1/2} \tag{9-7}$$

where P_1 is the equivalent pressure of iodine in the molecular beam striking the zircaloy. Inserting Eq (9-7) into Eq (9-5) yields

$$da/dt = A_1P_1 \exp(-E_1^*/RT) \exp(B_1K/T) \tag{9-8}$$

Here the exponential temperature dependence in K_1 is contained in E_1^*.

9.2.2 Aluminum Iodide From thermochemistry we know that in the vapor phase over crystalline aluminum iodide, $AlI_3(g)$ is the major species; $AlI_{(g)}$, $I_{(g)}$ and $I_{2(g)}$ are of several orders smaller in pressure. Therefore, the triodide drives the following chemical reaction on the zircaloy surface:

$$AlI_{3(g)} \Longleftrightarrow AlI_{(ads)} + 2I_{(ads)} \tag{9-9}$$

Reaction (9-9) is assumed to be in equilibrium. Consumption of $I_{(ads)}$ by reaction (9-1) is neglected. The law of mass action applicable to this reaction is:

$$K_2 = [AlI_{(ads)}][I_{(ads)}]^2/P_2 \tag{9-10}$$

where P_2 is the equivalent pressure of AlI_3 in the molecular beam. Since $[AlI_{(ads)}] = (1/2)[I_{(ads)}]$ because of the stoichiometry of Eq. 9-9, 9-10 becomes:

$$[I_{(ads)}] = (K_2/2)^{1/3} \tag{9-11}$$

and Eq (9-5) yields

$$da/dt = A_2P_2^{2/3}\exp(-E_2*/RT)\exp(B_2K/T) \tag{9-12}$$

9.2.3 <u>Iron Iodide</u> The reaction considered in this case is:

$$FeI_{2(g)} \Longleftrightarrow FeI_{(ads)} + I_{(ads)} \tag{9-13}$$

Assuming reaction (9-13) to be at equilibrium with the incident FeI_2 molecular beam:

$$K_3 = [FeI_{ads})][I_{(ads)}]/P_3 \qquad (9\text{-}14)$$

where P_3 is the equivalent pressure of FeI_2 molecular beam. Since $[FeI_{(ads)}] = [I_{ads})]$,

$$[I_{(ads)}] = K_3^{\ 1/2} P_3^{1//2} \qquad (9\text{-}15)$$

We get from Eq (9-5)

$$da/dt = A_3 P_3 \exp(-E_3^*/RT)\exp(B_3 K/T) \qquad (9\text{-}16))$$

These reaction models reproduce the stress, temperature, and equivalent reaction pressure dependences which were observed experimentally. In particular, the observed reaction orders (unity for I_2 and FeI_2 and 0.7 for AlI_3) are predicted by the proposed chemical model.

9.3 <u>In-Pile Situation</u>

9.3.1 <u>Chemistry of Iodine</u> In a recent publication,[23] Cubicciotti et al. discussed iodine chemical activity in reactor fuel pin. They showed that the iodine partial pressure is determined by the equilibrium between cesium iodide and cesium uranate:

$$CsI(s)+(1/2)UO_2(s)+(1/2)O_2(\text{from fuel})$$
$$<=>(1/2)Cs_2UO_4(s)+I(g) \qquad (9\text{-}17)$$

The calculated pressure of monoatomic iodine is 10^{-19} atm (at -410 KJ/mole of O_2). The equilibrium pressure of I(g) for a monolayer of

chemisorbed iodine on zircaloy is also ~10^{-19} atm.[23] They suggested that reaction 9-17 generates a pressure of iodine (10^{-19} atm) which is large enough to create a chemisorbed iodine layer on zircaloy.[23] The reactor fuel center has a higher oxygen potential. A power rise can release fission products (e.g., CsI) from hot fuel center to the gap and simultaneously increase the oxygen potential in the pellet-cladding gap. Both effects according to reaction 9-17, increase the iodine activity.[23]

However, possible kinetic limitation must be considered in addition to the thermochemistry. The impingement rate of gas molecules on surface is determined by:

$$\text{Impinging Rate} = P \Big/ \sqrt{2\pi mkT} \qquad (9\text{-}18)$$

where P is iodine pressure, m its molecular weight, k the gas constant, and T the temperature. For 10^{-19} atm of I(g),

$$\text{impingement rate} = 10^{-19}\text{atm} \times 1.0133 \times 10^{6}\ \text{gcm}^{-1}\text{sec}^{-2}/\text{atm} \Big/ \sqrt{2n \times 126.9\text{g/mole} \times 8.314 \times 10^{7}\text{gcm}^{2}\text{sec}^{-2}\text{mole}^{-1}\text{K}^{-1} \times 623\ \text{K}}$$

$$= 1.58 \times 10^{-20}\text{moles/cm}^{2}\text{sec}$$

$$= 9.5 \times 10^{3}\text{atoms/cm}^{2}\text{sec}$$

A rough estimate of the atom size in the iodine crystal can be calculated from the density of iodine, 4.93 g/cm^3, or 2.3×10^{22}atoms/cm^3. The volume each atom occupies is 4.3×10^{-23}cm^3/atom. Therefore, $(4.3 \times 10^{-23})^{2/3} = 1.2 \times 10^{-15}$cm^2 is roughly surface area occupied

by each iodine atom. There are 8.2×10^{14} atoms/cm^2 for a monolayer iodine surface layer. If we assume that every iodine molecule which strikes the zircaloy will stick, we find it will take 2700 years to form a monolayer of adsorption under 10^{-19}atm of monoatomic iodine. Thus, neither the hypothesis of irradiation decomposition of CsI nor the equilibrium pressure of I in a fuel pin appears to implicate fission product iodine in the PCI (pellet-cladding interaction) process.

9.3.2 Chemistry of Cadmium Cadmium remains in the elemental state inside a reactor fuel pin,[19,33] and is sufficiently volatile to be present in the fuel-cladding gap.[15] The vapor pressure is calculated to be 0.25 torr at cladding temperature, 350°C.[44]

Let us consider a 1 cm long section of a 1 cm diameter fuel rod. A 90 percent smear density is assumed, so that the section contains 0.64 cm^3 of solid UO_2 and 0.07 cm^3 of gas space. The number of fissions per unit volme can be calculated from the burnup, and the total cadmium produced in the section is given by:

$$N_{CD} = Y_{Cd} \times (0.64\ \text{cm}^3) \times (D) \times \text{Burnup(in MWd tonne}^{-1}) \times 2.7\text{x}10^{14}\ \text{fissions tonne MWd}^{-1}\ \text{g}^{-1}/6.023\text{x}10^{24} \qquad (9.19)$$

Where (D) is the density of UO_2 (10.98 g/cm^3), and Y_{Cd} is the fission yield of cadmium (0.1 percent).[15] Cadmium can be present in either the gas or the condensed phase. The mass balance is:

$$0.07\ \text{cm}^3\ P_{Cd}\ /\ RT + n_{Cd} = N_{Cd} \qquad (9\text{-}26)$$

where n_{Cd} is the gram moles of cadmium present as a condensed phase.

Combining Eqs 9-19 and 9-20 shows that enough cadmium in the vapor phase is produced after 0.15 MWd/tonne burnup to attain the 0.25 torr vapor pressure. For a 30,000 MWd/tonne fuel lifetime, most cadmium will exist in condensed phase and maintain the partial pressure of cadmium at 0.25 torr. This pressure is much higher than 4×10^{-3} torr pressure required for cadmium vapor embrittlement of zircaloy (Section 7.5.4). Cadmium is a prime candidate for the PCI instigator in light water reactors. The fracture surface of specimens failed in out-of-pile tests with cadmium vapor is similar to these observed for in-pile PCI failures. However, cadmium embrittlement always produces large strain, burst-type failures in the laboratory, whereas PCI failures in reactor fuel cladding is of the small strain, pinhole-type.

10. CONCLUSIONS

10.1 Unirradiated Stress Corrosion Cracking Test Results

Compared to control specimens at the temperature and stress, failure times are greatly reduced by the presence of iodine, iron iodide, and aluminum iodide. For both iodine and iron iodide, there exists a stress (379 MPa), above which "burst-type" failure occurs. Lower stresses produce "pinhole-type" failures. However, the fractography of both types of failures show cleavage characteristics which are very different from the ductile dimple fracture surface found in the absence of corrosive agents. These three types of stress rupture failures are shown in Fig. 10-1.

All specimens tested under cadmium exhibited burst-type failure and the fracture surface showed brittle-type cleavage features. For cadmium, the rupture times were shorter than those of the controls specimens but exhibited more scatter than those in iodine or metal iodides. Fracture occurred randomly inside the cadmium-affected region on the zircaloy specimen, unlike iodine and iodides, where failure always took place at the center of molecular beam spot. There may be some unknown surface inhomogeneity controlling the cadmium embrittlement process which is not present in SCC by iodine or metal iodides. Specimens cut from different tubes gave widely varying rupture times in cadmium, but tests using the same zircaloy tubes gave consistent results.

In cesium iodide tests, plots of time to failure versus stress did not show any decrease in comparison with control specimens. SEM

fractography revealed completely ductile behavior, the same as that without a corrosive agent.

Greatly reduced failure times and brittle fractography are the two main features of stress corrosion cracking. On both counts, iodine, iron iodide, and aluminum iodide are stress corrosion cracking agents for zircaloy. However, casium iodide is not. This behavior is consistent with the thermochemistry of the reaction[16]

$$0.55I_2(g) + Zr(s) \text{ --- } ZrI_{1.1}(s)$$

$$\Delta G^\circ 600K = -37.9 \text{Kcal/mole} \qquad (10\text{-}1)$$

$$0.37AlI_3(g) + Zr^*(s) \text{ --- } 0.37Al(s) + ZrI_{1.1}(s)$$

$$\Delta G^\circ 600K = -11.0 \text{ Kcal/mole} \qquad (10\text{-}2)$$

$$0.55\ FeI_2(g) + Zr(s) \text{ --- } 0.55Fe(s) + ZrI_{1.1}(s)$$

$$\Delta G^\circ 600K = -32.7 \text{ Kcal/mole} \qquad (10\text{-}3)$$

$$1.1\ CsI(g) + Zr(s) \text{ --- } 1.1Cs(1) + ZrI_{1.1}(s)$$

$$\Delta G^\circ 600K = +\ 29.4 \text{ Kcal/mole} \qquad (10\text{-}4)$$

The standard free energies are negative, suggests that the first three reactions are possible, but the last one is prohibited. This may be the reason why iodine, iron iodide, and aluminum iodide, but not cesium iodide, can cause SCC of zircaloy.

10.2 Data Correlation of Failure Times

The rupture time data are correlated in terms of the crack growth model:[28,30]

$$da/dt = A\ p^n \exp(-E/RT)\exp(BK/T) \qquad (10\text{-}5)$$

Where a is the crack length, p is the partial pressure of the SCC agent, K is the stress intensity factor, and T is the temperature. A and B are constants. When integrated from the initial length a_o to the final length a_c at which the net section stress reaches the ultimate tensile stress, Eq. 10-5 gives the rupture time. The chemical or corrosion aspects of SCC is related to the reaction order n and activation energy E. These parameters are shown in Table 10-1.

The reaction orders for I_2 and FeI_2 are both unity, whereas that of AlI_3 is 2/3. These values reflect a rate-limiting surface chemical step with kinetics associated with the number of iodine atoms per molecule of SCC agent. The order for cadmium embrittlement is unity. Alloying processes take place at the zircaloy specimen surface.

This crack growth model also predicts SCC experiments with variable loading and surface roughness.[45]

Despite the successes of the model, the basis of its applicability to iodine SCC is still uncertain. First, the model contains no provision for a threshold stress below which iodine does not affect the rupture lifetime. Equation 10-5 is valid only for stresses larger than the threshold value, which can only be determined empirically. A threshold stress may be required to initiate cracks, but, once done, their propagation is governed by the growth theory utilized here (Chapter 6).

Second, the model does not explicitly account for variations in specimen texture, although this variable may influence parameters A and B in Eq. 10-5.

Third, the stress dependent term in the model is exp ($\sigma' \Delta V^*/RT$). If we use the maximum values $\sigma' = \sigma_{UTS}$ and $\Delta V^* = V_m$ (the molar volume)

$$\exp(\sigma_{UTS} V_m/RT) = 1.3$$

The value is not large enough to account for rapid reaction at crack tip compared to the flat outside surface of the tube when the stress is applied.

10.3 Radiation Enhanced Cesium Iodide Stress Corrosion Cracking Tests

Because of the limitation of the proton range in CsI (3 μm), we attempted to avoid thick CsI film formation on the zircaloy specimens by reducing the CsI supply from the Knudsen cell (Section 8.5.3). However, the low CsI pressure irradiated tests (5×10^{-5} and 10^{-5} torr) did not show stress corrosion cracking phenomenon. Neither did the higher CsI pressure experiments which very likely had CsI film > 3 μm thickness, which would prevent the proton beam from reaching the film/metal interface where iodine liberation would be most effective.

10.4 In Pile Situation

From the discussion in Section 9.3, we know that the pressure of I(g) generated by the equilibrium of CsI(s) and Cs_2UO_4(s) is not

sufficient for zircaloy SCC. Radiation dissociation of CsI is necessary if PCI is to cause CsI stress corrosion cracking of zircaloy. Besides this report, two other papers[37,38] failed to demonstrate an irradiated CsI stress corrosion cracking phenomenon. However, cadmium is in the elemental state inside the reactor fuel pin,[19,33] and it can embrittle zircaloy at low pressure (4×10^{-3} torr) (Section 7.5.4). Much higher inpile cadmium partial pressures are calculated (Section 9.3.2). The amount of cadmium produced by fission is more than enough to create the required pressure (Section 9.3.2). Cadmium provides an alternative PCI mechanism.

Table 10-1 Chemical Parameters for Zircaloy SCC

SCC AGENT	MINIMUM PARTIAL PRESSURE TORR	STRESS EXPONENT	REACTION ORDER	ACTIVATION ENERGY KCAL/MOLE	STABILITY OF IODIDE
I_2	1×10^{-3}	~4	1.0 ± 0.1	7	-38
FeI_2	3×10^{-3}	~20	0.9 ± 0.1	131	-33
AlI_3	1×10^{-3}	—	0.7 ± 0.1	—	-11
CsI	←	No Effect	→		+29
CD	4×10^{-3}	~20	1.0 ± 0.2	54	—

(A) M in $da/dt \propto K_I^M$

(B) ΔG° (Kcal/mole) for the reaction:

$$1/N\ MI_N(g) + Zr(s) \longleftrightarrow ZrI(s) + 1/N\ M(s) \text{ at } 600^\circ K$$

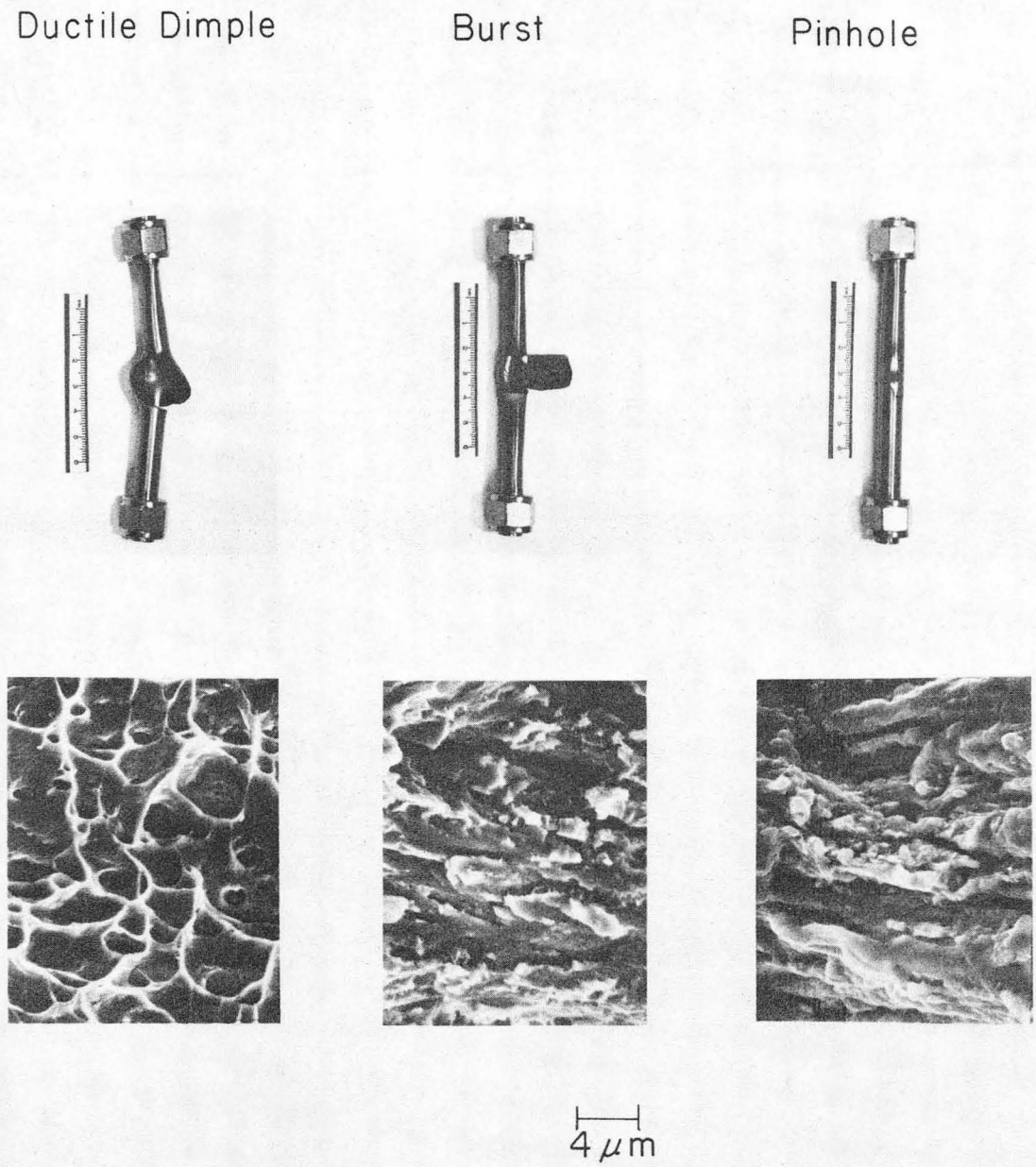

XBB 800-14059A

Figure 10-1. Comparison of fractography.

APPENDIX A IODINE FLOW RATE CALIBRATION

A.1 Introduction

In order to provide enough iodine, the diameter of the iodine doser was made as large as possible (subject to the limitation of the diffusion pump's speed). In the iodine experiment, the doser diameter is slightly larger than the mean free path at the vapor pressure over solid iodine at room temperature. This means that the flow through the filing tube is in the free molecular flow range. However, calibration is necessary to achieve accurate iodine flow rates and equivalent iodine pressure at the zircaloy surface.

A.2 Apparatus

The apparatus for the present experiment shown in Fig. A-1 consists of two major parts. The doser assembly consists of a doser tube, reservoir, several valves, and an argon filling line. Several dosers were tested. The dimensions of the doser tubes were the same as the iodine dosers used in the stress corrosion cracking tests (Chapter 3). The second part of Fig. A-1 is the "target" assembly which consists of a tube with 1 mm hole in the center. A wide range pressure gauge and an ion gauge are connected to the tube for pressure measurement inside the target tube. The target tube is the same size as the zircaloy specimen.

A.3 Calibration Procedure

Argon is used in the calibration experiment. The wide range pressure gauge from Granville Phillips Co. was supplied with an argon calibration curve. The corrosive nature and unknown gauge calibration of iodine dictated for use of argon as a substitute.

The calibration procedure is as follows:

(1) Remove the target assembly from the system. With the outlet valve of the reservoir closed, fill the reservoir with argon. Close the filling valve, open the outlet valve of the reservoir. Argon gas flows through the doser into the vacuum system. The pressure drop of the reservoir is recorded as a function of time to determine the flow rate.

(2) Repeat part (1) with the target assembly in the system. The distance between the doser outlet and the 1 mm hole on the target is varied over the range of values used in the iodine stress corrosion cracking tests (Chapter 3).

(3) With the outlet and filling valves of reservoir open, adjust the regulating valves on argon filling line. The pressure in the reservoir is adjusted to create a desirable flow rate of argon through the doser. Wait long enough to let the gas inside the target tube come to equilibrium (i.e., when the incoming and outgoing rates through 1 mm hole are equal). The outgoing rate at the hole is proportional to the gas pressure inside the target assembly. The incoming rate depends on flow rate through the doser and distance between the doser outlet and the 1 mm hole on the target tube. This incoming rate defines the equivalent pressure created by the doser and the doser-target geometry. Gauges on the target assembly measure the gas pressure which is the equivalent pressure produced by the argon flow through the doser.

A.4 Results and Discussion

(1) Figure A-2 gives the pressure drop versus time in the experiments of Part (1). The curve in the figure is the calculated value from Schock's model.[20] The pressure drop in the reservoir is calculated from the argon flow rate, which is obtained by solving the following equation for the dimensionless mass flow rate M.

$$L/D = (0.0196)\ [\dot{M}^{-1} - \dot{M} + 2\dot{M}\log\dot{M})P_1 + 22(1-\dot{M})^2/\dot{M}] \qquad \text{(A-1)}$$

where

D = diameter of doser tube [cm]

L = length of doser tube [cm]

m = mass flow rate [g/sec]

$$\dot{M} = [4\dot{m}\ \sqrt{RT}]/\pi D^2 p_1 \qquad \text{(A-2)}$$

p_1 = pressure at tube inlet (iodine or argon reservoir) [dyne-cm^{-2}] = [g-cm^{-1}sec^{-2}]

R' = universal gas constant divided by the molecular weight of flowing gas [g-cm^{2}sec^{-2}mole^{-1}K^{-1}]/[g-mole^{-1}] = [cm^{2}sec^{-2}K^{-1}]

$$P_1 = P_1/\ [\ \sqrt{0.5\pi RT}(\nu/D)]$$

is the dimensionless pressure at doser inlet

ν = viscosity of flowing gas [poises] = [g-cm^{-1}sec^{-1}]

The discrepancy between theory and experiment is small. We can use the Schock model to calculate the mass flow rate $\dot{m}$ for iodine and convert this to the molar flow rate 1* (moles/sec) by dividing by 254.

(2) As a result of step (2) of the calibration procedure, we find that the presence of the target assembly does not affect the argon flow rate for all doser sizes and doser-target distances used (Fig. A-3). This means that small gap between the doser outlet and the target produces a very small resistance to gas flow in comparison to that of the doser tube itself.

(3) If the distance between the doser outlet and target (d) is large in comparison with doser diameter (D), the gas flux on the target surface may be assumed to arise from a point source:

$$I^* = X 1^*/\pi d^2 \qquad \text{(A-3)}$$

where

1* = iodine flow rate through the doser (moles/sec)

I* = impingement rate of iodine molecules on the target (moles/cm^{2}cm)

X = peaking factor[46] which characterizes non-cosine emission from long channels

The equivalent pressure P_{eq} is given by

$$I^* = P_{eq} \Big/ \sqrt{2\pi mkT} \qquad \text{(A-4)}$$

where

m = molecular weight of the flowing gas

k = gas constant

T = temperature of the gas

Figures A-4 and A-5 give examples of χ values versus flow rate and doser outlet to target distance for two certain size doser after part (3) experiment. The peaking factor is expressed as a combination of Eqs. A-4 and A-5.

$$\chi = P_{eq} n d^2 \;/\; 1^* \quad \sqrt{2\pi mkT}$$

From Fig. A-4 and A-5, it is seen that the peaking factor χ depends only on doser size and distance between doser and target, and not on the flow rate. It is reasonable for the impingement rate to be proportional to flow rate.

In general, the peaking factor depends on angular distribution of molecules leaving the doser, doser target-distance, and doser diameter. In our experiment, the length of the doser is much larger than the diameter. The angular distributions of the flow from different dosers must be almost the same.[46] We take a normalized distance, the doser-target distance divided by doser diameter, as a control variable. The target sees the same

geometric effect from dosers with equal normalized distances. So we expect the peaking factor to be dependent only on the normalized doser-target distance, as shown in Fig. A-6. All data points fall in a narrow band.

A.5 Conclusion

The calibration method with argon used here gives reasonable flow rates and peaking factors. We can apply Eqs. (A-1)-(A-3) to determine the molar flow 1* from the iodine doser inlet pressure p_1 and Fig. A-6 to the calculation of iodine equivalent pressure on zircaloy surfaces.

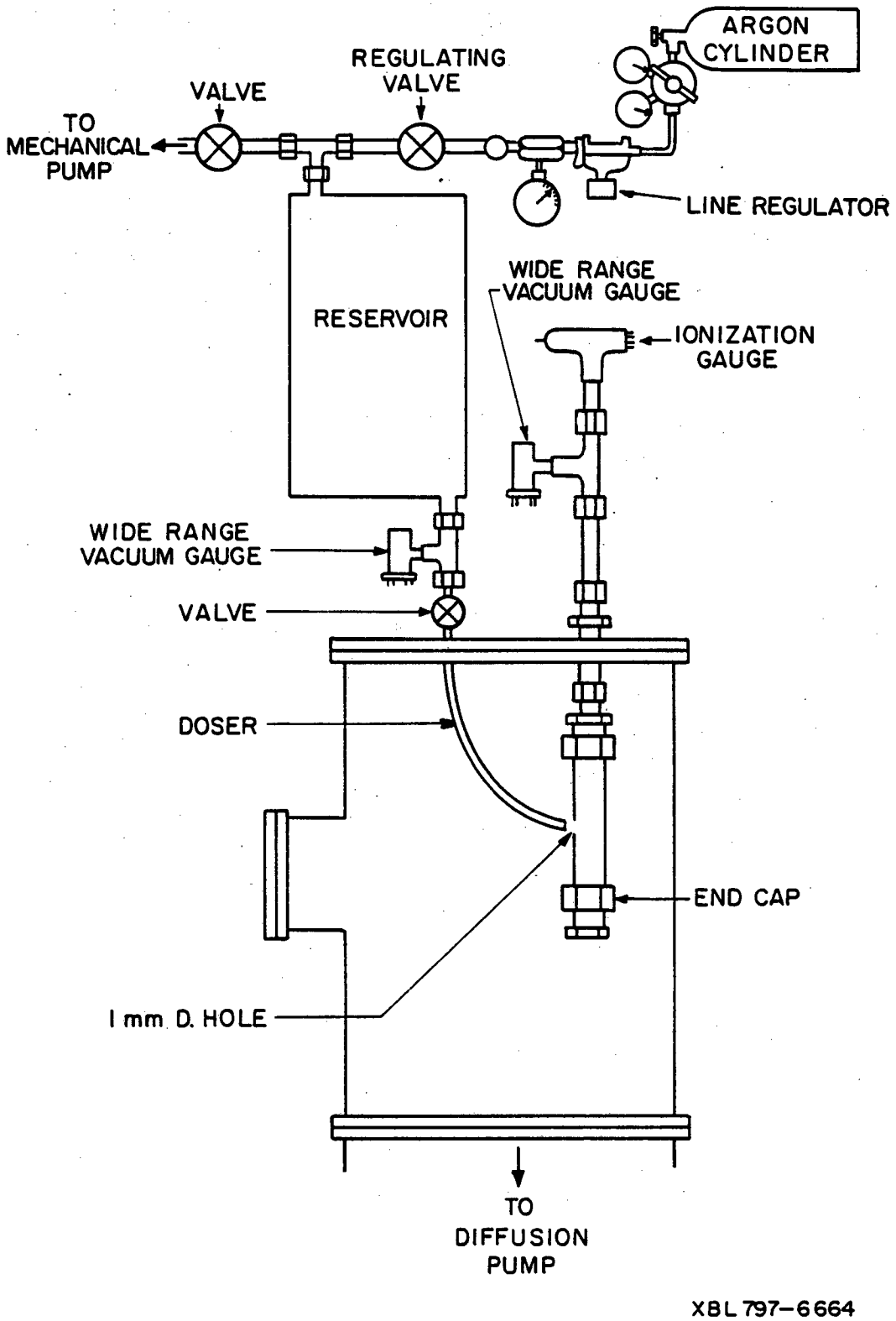

Figure A-1. Doser flow rate calibration apparatus.

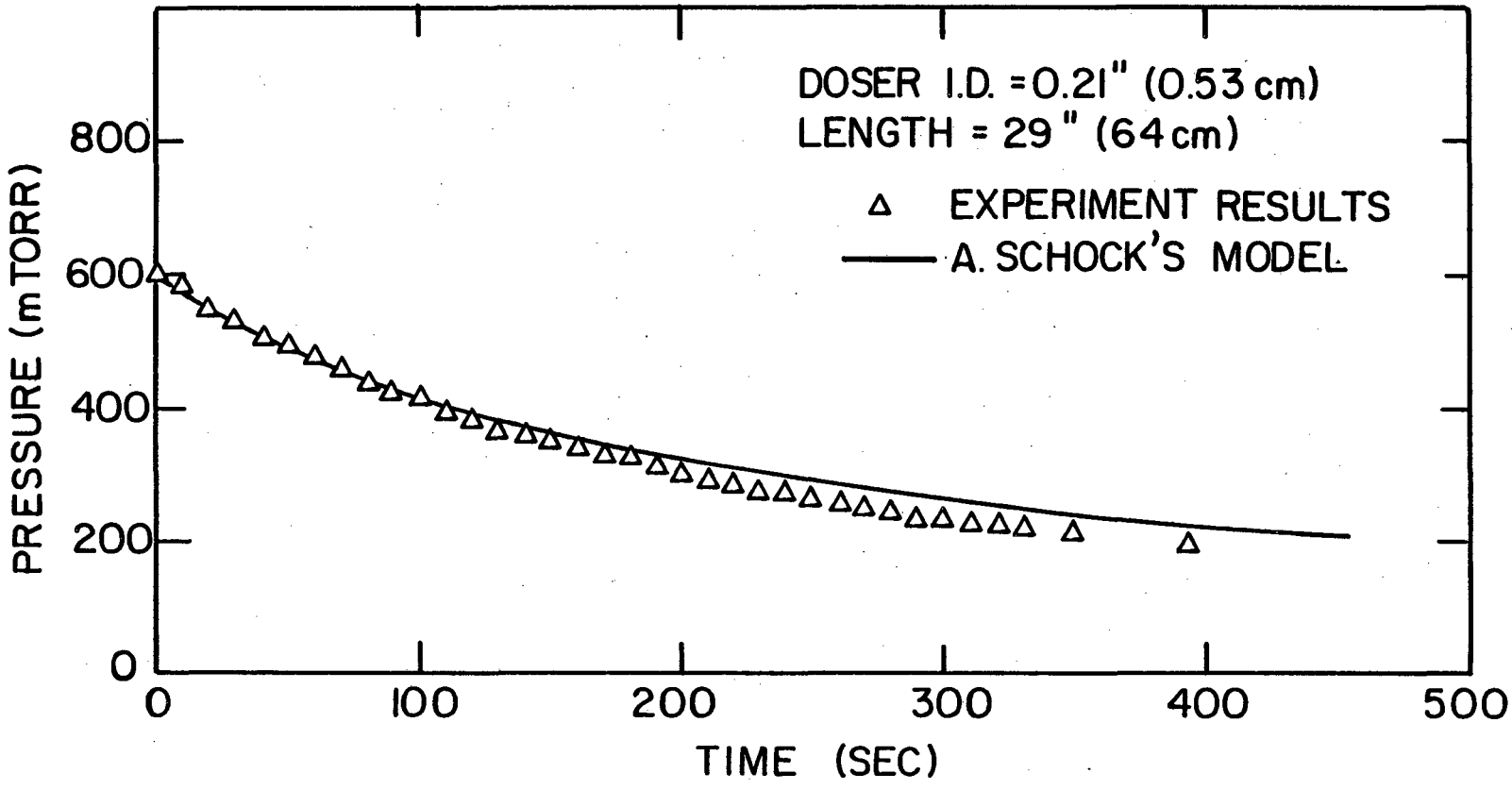

XBL 798-6811

Figure A-2. Pressure drop vs. time in the reservoir compared with Schock's model (Argon).

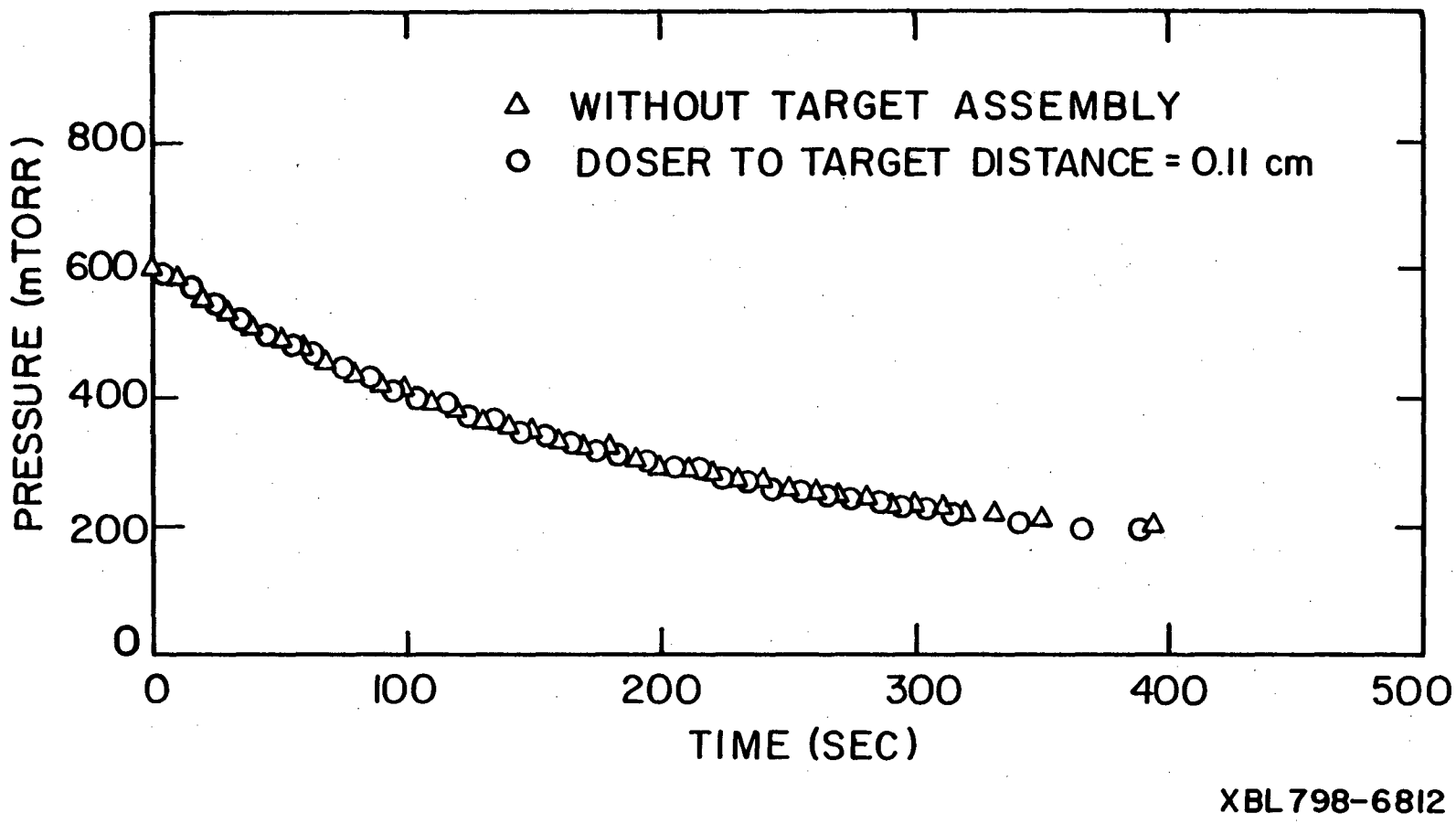

Figure A-3. Pressure drop vs. time to the reservoir with and without target assembly (Argon).

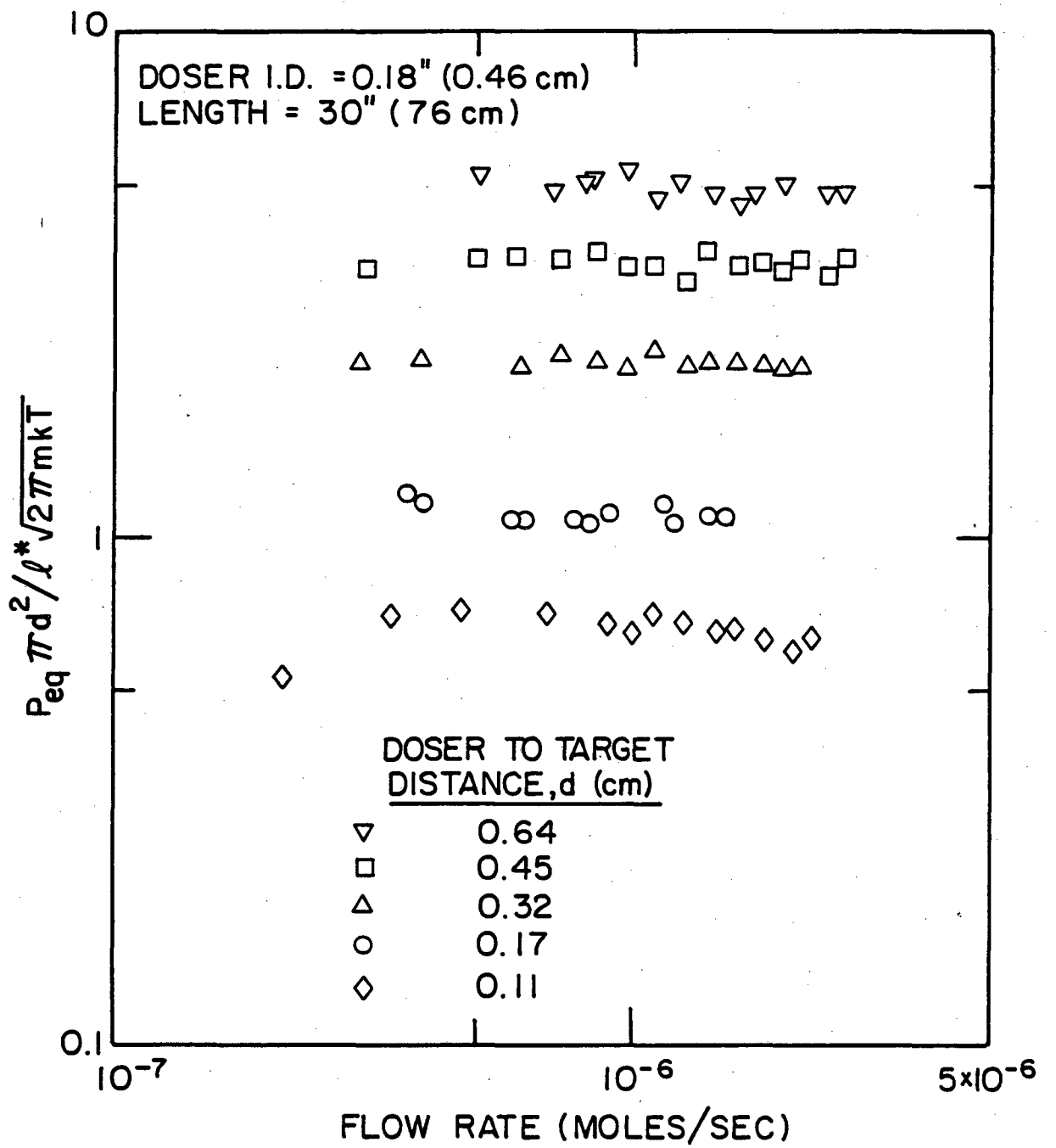

Figure A-4. Peaking factor vs. flow rate and doser-to-target distance (Argon).

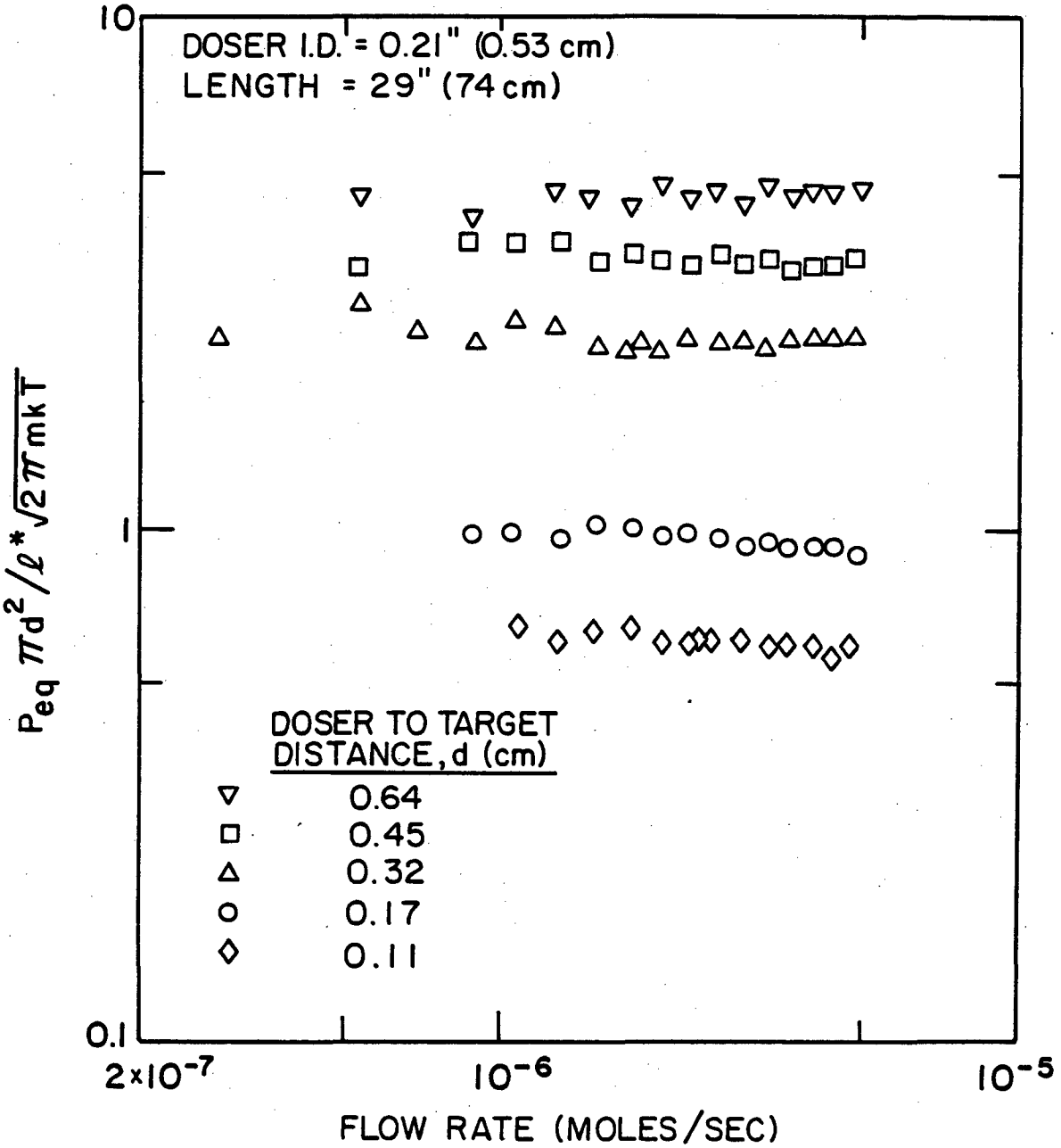

XBL 798-6806

Figure A-5. Peaking factor vs. flow rate and doser-to-target distance (Argon).

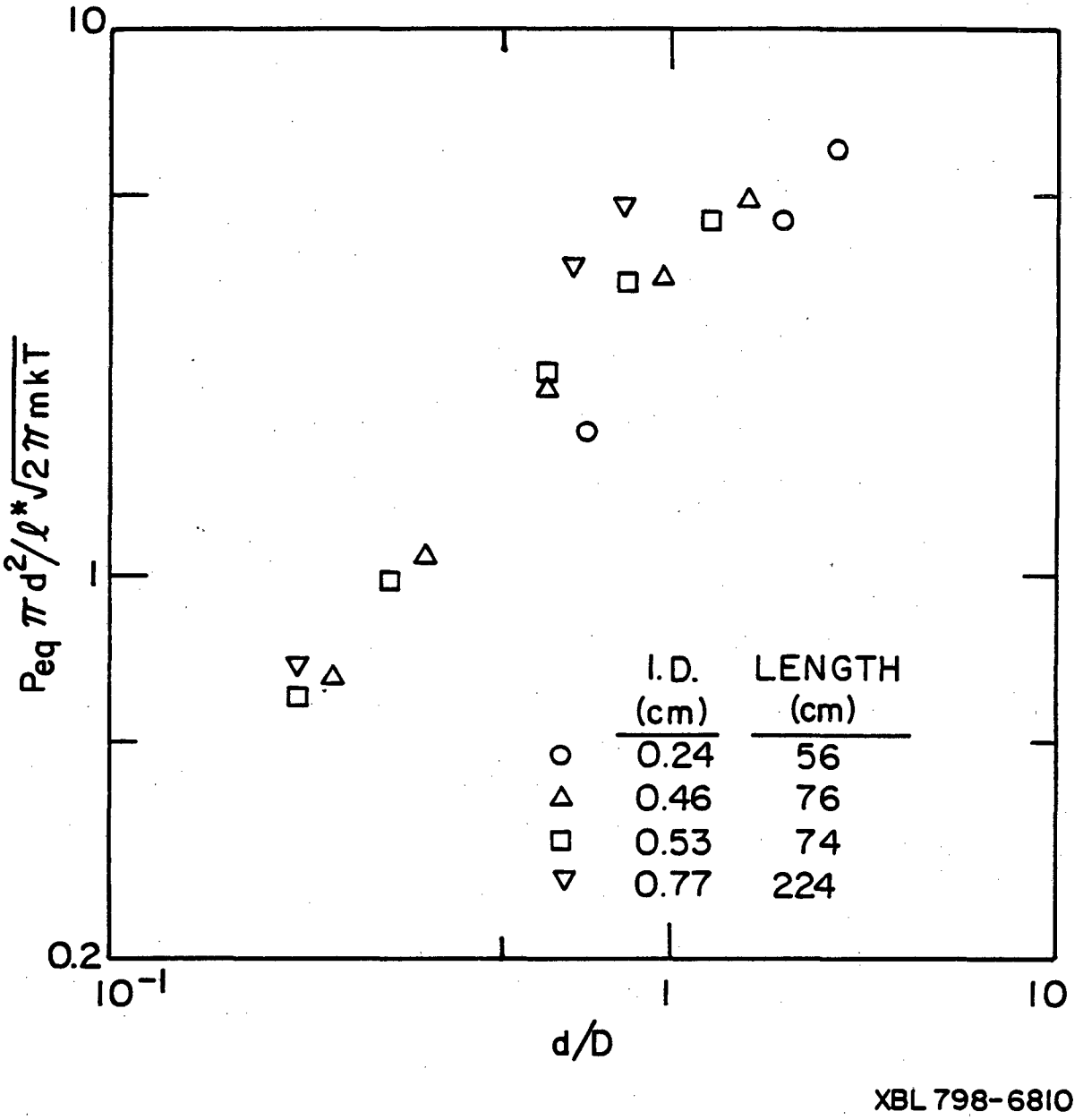

Figure A-6. Peaking factor vs. normalized doser-target distance (Argon).

APPENDIX B CALCULATION OF VAPOR PRESSURE OVER ALUMINUM IODIDE IN A STAINLESS STEEL KNUDSEN CELL

The following chemical reactions are considered in the Knudsen cell (made of stainless steel) above solid aluminum iodide:

$$AlI_3(s) = AlI_3(g)$$
$$AlI_3(g) = AlI(g) + I_2(g)$$
$$I_2(g) = 2I(g)$$
$$I_2(g) + Fe(s) = FeI_2(g)$$

The opening of the Knudsen cell is very small, so we can assume that the amount of gas outflow is negligible. There is no disturbance of the equilibrium in the vapor phase. Two possible conditions are considered:

(1) $P_{FeI_2(g)}$ is less than the vapor pressure of $FeI_2(s)$

There is no solid FeI_2 present. We take the mass balance equation into consideration:

Number of iodine atoms in vapor phase

= 3 X (number of aluminum atoms in vapor phase)

for congruent vaporization.

$$3P_{AlI_3} + P_{AlI} + P_{I_2} + P_I + 2\,P_{FeI_2} = 3\,(P_{AlI_3} + P_{AlI})$$

All equilibrium pressures can be calculated.

(2) $P_{FeI_2(g)}$ is equal to the vapor pressure of crystal $FeI_2(s)$

Since solid FeI_2 is present in the system,

$$FeI_2(s) = FeI_2(g)$$

We can caluclate the value of other vapor pressures by setting P_{FeI_2} equal to the vapor pressure of $FeI_2(s)$.

After detailed calculation, we find no FeI_2 solid present, and $AlI_3(g)$ is the major species in vapor. The relative pressures of vapor components are indicated in Fig. B-1.

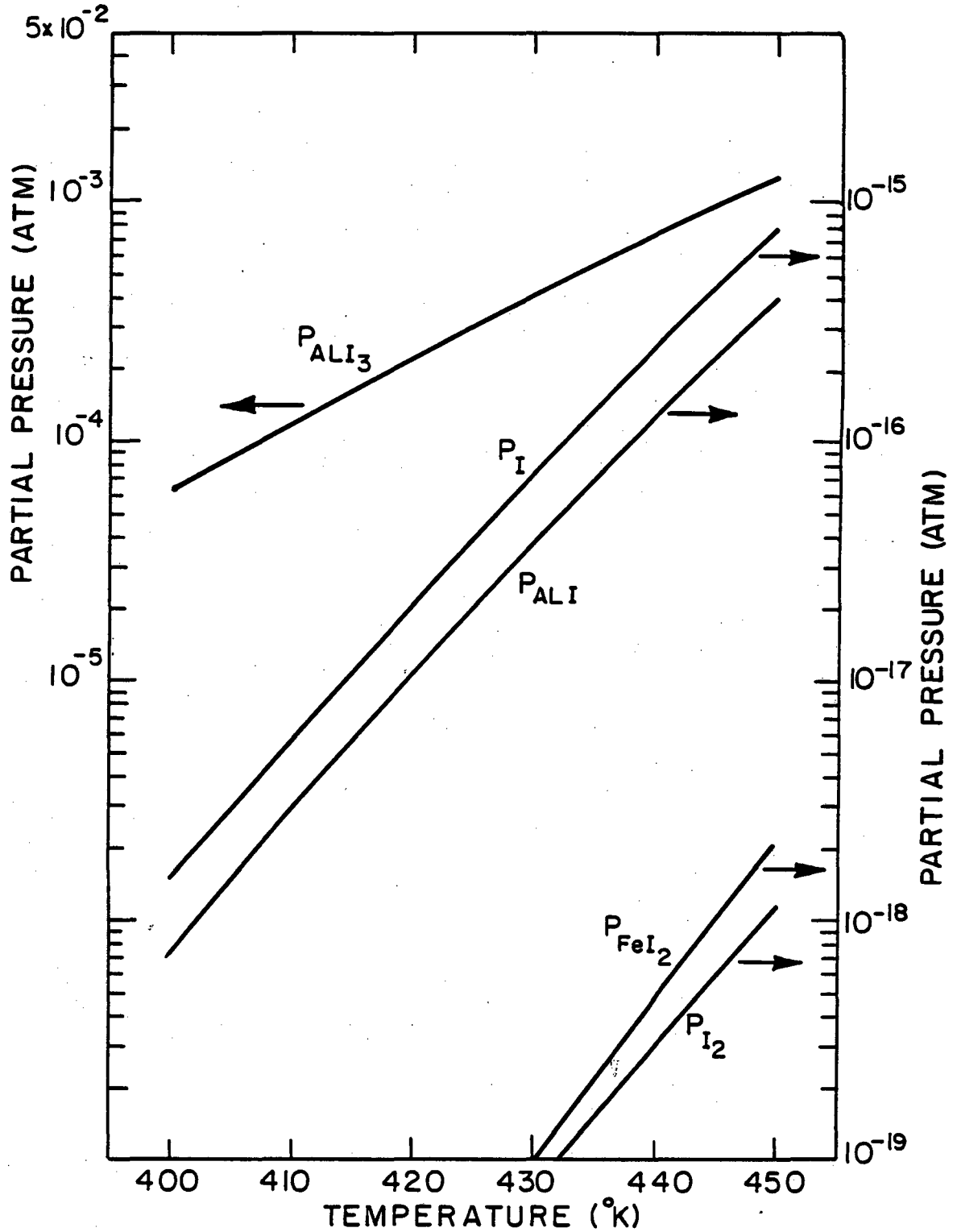

XBL 797-6674

Figure B-1. Relative pressures of vapor species over aluminum iodide crystals in a stainless steel Knudsen cell.

REFERENCES

1. J. C. Wood, B. A. Surette, I. M. London, and J. Baird, J. Nucl. Mater., 57 (1975) 155.
2. A. Garlick and P. D. Wolfenden, J. Nucl. Mater., 41 (1971) 274.
3. P. H. Kreyns, G. L. Spahr, and J. E. McCanley, WAPD-TM-1203 (1976).
4. J. G. Weinberg, WAPD-TM-1048 (1974).
5. R. P. Tucker, P. H. Kreyns, and J. J. Kearns, WAPD-TM-1248 (1976).
6. J. C. Wood, J. Nucl. Mater., 45 (1972/1973) 105.
7. C. C. Busby, R. P. Tucker, and J. E. McCauley, J. Nucl. Mater., 55 (1975) 64.
8. K. Videm and L. Lunde, Annals of Nuclear Energy, 3 (1976) 305.
9. I. Aitchison and B. Cox, Corrosion, 28 (1972) 83.
10. B. Cox, Corrosion, 28 (1972) 207.
11. J. C. Wood, Nucl. Technol., 23 (1974) 63.
12. A. Garlick, J. Nucl. Mater., 49 (1973/1974) 207.
13. D. Cubicciotti and R. L. Jones, EPRI NP-717 (1978).
14. N. W. Polan and R. P. Tucker, WAPD-1313 (1977).
15. D. Cubicciotti et al., "The Nature of Fission Product Deposits inside Light Water Reactor Fuel Rods" SRI Report, Project No. 4197 (1976).
16. D. Cubicciotti, R. L. Jones, and B. C. Syrett, "Stress Corrosion Cracking of Zircaloy," EPRI NP-1329 (1980).
17. A. K. Miller et al., EPRI NP-1798 (1981).
18. M. Peehs, H. Stehle, and E. Steinberg, ASTM STP-681, pp. 244 (1979).

19. W. T. Grubb and M. H. Morgan III, "Cadmium Embrittlement of Zircaloy," ANS Topical Meeting on Light Water Reactor Fuel Performance, St. Charles, Illinois, May 1977.

20. A. Schock, FSEC-NSG-217-74/37B (1974).

21. R. A. Gough, R. Lam, C. Martinez, and D. Morris, Nuclear Instrument and Methods 138 (1976) 415.

22. Katsumi Une, J. Nucl. Sci. Eng., 14 (1977) 443.

23. D. Cubicciotti, R. L. Jones, and B. C. Syrett, "Chemical Aspects of Iodine-Induced Stress Corrosion Cracking of Zircaloy," ASTM Fifth Conference on "Zirconium in Industry," 1980.

24. W. A. Backofon, W. F. Hosford, Jr., and J. J. Burke, Trans ASM (1962) 264.

25. E. I. Lin, Trans Amer. Nucl. Soc., 27 (1977) 597.

26. F. L. Yaggee, R. F. Mattas, and L. A. Neimark, EPRI NP-1155 (1979).

27. D. L. Baty, "Iodine Stress Corrosion Cracking of Zircaloy-4 Tubes," IAEA Specialists' Meeting on Internal Fuel Rod Chemistry, Erlangen, Germany, Jan. 1979.

28. A. G. Evans and T. G. Longdon, Progress in Materials Science, 21 (1976) 307.

29. S. Glasstone, K. J. Laidler, and H. Eyring, "The Theory of Rate Process," McGraw-Hill Book Company (1941).

30. S. M. Weiderhorn, J. of Amer. Ceramic Soc. 55, (1972) 83.

31. K. Gaugler, Personal communication.

32. D. L. Smith, J. Nucl. Mater., 75 (1978) 20.

33. D. Cubicciotti and J. E. Sanocki, J. Nucl. Mater., 78 (1978) 96.

34. J. C. Wood, D. G. Hardy, and A. S. Bain, "Mechanistic Studies of Power Ramping Defects," ANS Topical Meeting on Light Water Reactor Fuel Performance, Portland, Oregon, 1979.

35. C. F. Old, "Liquid Metal Embrittlement of Nuclear Materials," J. Nucl. Mater., 92 (1980) 2.

36. D. Cubicciotti and J. H. Davis, Nucl. Sci. Eng., 60 (1976) 314.

37. J. H. Davis, J. S. Armijo, and R. A. Proebstle, "In Pile Fuel Stress Corrosion Tests," American Ceramic Society Meeting, San Francisco, November 1976.

38. J. C. Wood and D. C. Hardy," Characteristics and Interpretation of Power Ramping Defects," ANS Topical Meeting on Light Water Fuel Performance, 1977.

39. S. G. Prussin, Personal Communication.

40. L. C. Northliffe and R. F. Schilling, Nuclear Data Tables, A7 (1970) 233.

41. D. R. Olander, "Fundamental Aspects of Nuclear Reactor Fuel Elements," Chapter 15, USERDA, TID 26711-P1 (1976).

42. P. Marmier and E. Sheldon, "Physics of Nuclei and Particles," Vol. 1, pp. 203, Academic Press (1969).

43. S. M. Weiderhorn and L. H. Bolz, J. of Amer. Ceramic Soc. 53, (1970) 543.

44. Handbook of Physics and Chemistry, 48th Eds., pp. D-113.

45. S. H. Shann and D. R. Olander, "Correlation of Failure Times for Iodine Stress Corrosion Cracking of Zircaloy," Nucl. Technol. 53 (1981) 407.

46. D. R. Olander and R. H. Jones, Entropie, 30 (1969) 42.

This report was done with support from the Department of Energy. Any conclusions or opinions expressed in this report represent solely those of the author(s) and not necessarily those of The Regents of the University of California, the Lawrence Berkeley Laboratory or the Department of Energy.

Reference to a company or product name does not imply approval or recommendation of the product by the University of California or the U.S. Department of Energy to the exclusion of others that may be suitable.

TECHNICAL INFORMATION DEPARTMENT
LAWRENCE BERKELEY LABORATORY
UNIVERSITY OF CALIFORNIA
BERKELEY, CALIFORNIA 94720